



Romain Bureau, MSc.

Modelling the microstructure evolution of an aluminium alloy 6082 during cold rolling and continuous solution annealing

DOCTORAL THESIS

to achieve the university degree of
Doktor der technischen Wissenschaften
submitted to

Graz University of Technology

Supervisor

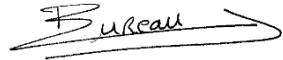
Assoc.Prof. Dr.techn. Cecilia Poletti

Institute of Materials Science, Joining and Forming

AFFIDAVIT

I declare that I have authored this thesis independently, that I have not used other than the declared sources / resources, and that I have explicitly marked all material which has been quoted either literally or by content from the sources used. The text document uploaded to TUGRAZonline is identical to the present doctoral thesis.

November 15th, 2017

Bureau

Acknowledgements

I cannot in good faith claim this thesis to be entirely mine. Rather, it is the result of a collaborative work involving contributors from several institutions, whom I shall thank here.

First and foremost, I offer my deepest gratitude to my supervisor, Assoc. Prof. Cecilia Poletti, for the support she showed me throughout this thesis. Her guidance of course, but also her patience, her kindness and her encouragements were deeply appreciated. They contributed greatly to make this work whole.

I also would like to express my thanks to Prof. Christof Sommitsch for welcoming me in the institute and initially co-supervising me. The support he shows to his students is remarkable.

The company AMAG Austria Metall AG has my gratitude for entrusting me with this project and providing us the necessary testing material. On a personal level, I would like to thank Dipl.-Phys Peter Simon and Dipl.-Phys. P. Schulz for their co-supervision from the company's side. Their help and their patience were invaluable.

Many thanks to Prof. Ernst Kozeschnik and Dr. Piotr Warczok from the Institute of Materials Science and Technology, TU Wien, for the profitable input they brought to this project.

I am grateful to Dr.-tech. Evgeniya Kabliman and Dr.-tech. Pavel Sherstnev from the Austrian Institute of Technology for the extensive discussions we had in the first half of this project, as their model served as basis for this work.

The Material Center Leoben coordinated this project. They are warmly praised for their support. Many thanks to Katrin Ebner for her help in the administrative issues.

Thanks to Dr. Stefan Mitsche from the Austrian Center for Electron Microscopy and Nanoanalysis FELMI-ZFE for the microscopic investigations he carried out for this project.

From the AGH University of Science, department of Applied Computer Science, my gratitude goes to Dr. Piotr Macioł for the work done in implementing the models developed here in his AM3 structure. I also offer my gratitude to Prof. Maciej Pietrzyk who gracefully accepted to review this work and to participate in my defense as an assessor.

Many thanks go to Manuela, Isabella, Claudia and Sandra for their help in all kinds of administrative businesses.

From the laboratory team, however little experimental work I had to do, I always received unwavering help when I needed it, and for that I am grateful.

Additionally, I would like to acknowledge the works of Peter Loidolt and Mirjam Spuller, whom I had the pleasure to supervise during my thesis.

Martina and Dilek shall also receive a special thank for helping me on various occasions, may they be work related or not.

Special thanks to Surya for the free coffees, and the sometimes animated but nonetheless fruitful discussions that ensued.

Now it is hard to remember every situation where a word, an advice or a critical remark from any of my co-workers was helpful. Therefore I shall thank the modelling group, but also the rest of the IWS team all together. The friendly and respectful atmosphere they maintained made it a pleasure to go to work every day.

Last but not least, I take this occasion to thank my parents for always supporting me in my studies.

Financial support by the Austrian Federal Government (in particular from Bundesministerium für Verkehr, Innovation und Technologie and Bundesministerium für Wissenschaft, Forschung und Wirtschaft) represented by Österreichische Forschungsförderungsgesellschaft mbH and the Styrian and the Tyrolean Provincial Government, represented by Steirische Wirtschaftsförderungsgesellschaft mbH and Standortagentur Tirol, within the framework of the COMET Funding Program is gratefully acknowledged.

Abstract

The production processes of metallic parts usually consist in a succession of thermal and mechanical steps that transform the material at its very core, at a microscopic level. The induced changes directly impact the material properties at a macroscopic level. Hence, understanding the micro-mechanisms involved in the shaping of metallic parts has become a major concern for the manufacturers.

Upon straining, some metallic materials, such as aluminium alloys, tend to self-harden, owing to interaction of microscopic defects with the other constituents of the microstructure. The evolution of the density of dislocations, of the grain size, the size and volume distribution of second-phase particles, among others, are all determinant when trying to assess the strength of metallic alloys.

In a previous work, Dr. P. Sherstnev had developed a model for high-temperature deformation and dynamic recrystallization of an industrial grade aluminium alloy 6082, featuring the dislocation density as single internal variable. Owing to its design, the model was unable to account for the work hardening at temperatures below 400 °C. In this thesis, the flow stress of the same alloy 6082 was measured by means of plane strain compression tests, for strain rates ranging from 10^{-2} s^{-1} to 10 s^{-1} and temperatures ranging from 25 °C to 400 °C. A subsequent constitutive model featuring two internal variables was developed in order to represent the observed work hardening. When the deformation temperature is decreased, the plane strain experiments showed that the yield stress deviates from the classically reviewed linearity. This was explained by stating that the flow stress must saturate to a maximum value when lowering the deformation temperature, corresponding to the maximum stress required to free moving dislocations from the attractive jog junctions they form on their way through the crystal.

Additionally, annealing experiments were conducted at 300 °C and 400 °C, after room temperature deformation. The observation of the induced kinetics of nucleation and growth of recrystallized grains served as basis to develop a recrystallization model. The latter takes as input the same microscopic variables as the ones used in the constitutive model. As such, it was designed with the objective to

complement it, and the equations describing the microstructure evolution in the constitutive model could be re-used. A custom nucleation criterion was expanded in order to make the model predict the time of beginning of recrystallization. The nucleation and the growth models are made aware of the competitive static recovery that tends to inhibit the recrystallization kinetics, thus the output of the model revolves entirely around this competition.

Finally, both the constitutive model and the recrystallization model were successfully implemented as subroutine in a finite element code, which was in turn used to model an industrial multi-pass rolling process followed by a continuous recrystallization step.

Zusammenfassung

Der Herstellungsprozess von metallischen Bauteilen besteht gewöhnlich aus einer Abfolge von thermischen und mechanischen Schritten, welche die Mikrostruktur des Materials umwandeln. Die induzierten Veränderungen wirken sich direkt auf die makroskopische Materialeigenschaften aus. Daher ist das Verständnis der Mikromechanismen, die bei der Formgebung von Metallteilen beteiligt sind, für die Hersteller ein Hauptanliegen geworden.

Während der Verformung neigen einige metallische Materialien, wie Aluminiumlegierungen, aufgrund der Wechselwirkung von mikroskopischen Defekten mit anderen Bestandteilen der Mikrostruktur dazu, sich selbst zu verfestigen. Die Festigkeit von Metalllegierungen wird von der Versetzungsdichte, der Korngröße, der Größenverteilung und der Volumenverteilung von Partikeln der Sekundärphasen bestimmt.

In einer früheren Arbeit hat Dr. P. Sherstnev ein Modell für die Hochtemperaturverformung und die dynamische Rekristallisation einer industriellen Aluminiumlegierung 6082 entwickelt, das die gesamte Versetzungsdichte als einzelne interne Variable darstellt. Aufgrund seines Designs konnte das Modell die Kaltverfestigung bei Temperaturen unter 400 °C nicht berücksichtigen. In der vorliegenden Arbeit wurde die Fließspannung dieser Legierung mit Hilfe von biaxialen Verformungsversuchen für Dehnraten von 10^{-2} s^{-1} bis 10 s^{-1} und Temperaturen von 25 °C bis 400 °C festgestellt. Ein nachfolgendes Materialmodell mit zwei internen Variablen wurde entwickelt, um die beobachtete Verfestigung darzustellen. Bei abnehmender Verformungstemperatur zeigten die experimentellen Ergebnisse, dass die Fließspannung von der klassischen Betrachtung der Linearität abweicht. Dies würde bedeuten, dass die Fließspannung einen Sättigungswert erreicht, sobald die Verformungstemperatur gesenkt wird. Dieser Sättigungswert entspricht der maximalen Spannung, die erforderlich ist, um die beweglichen Versetzungen aus der Attraktivität der Jog Junctions zu lösen.

Nach der Verformung bei Raumtemperatur wurden Wärmebehandlungen bei 300 °C und 400 °C durchgeführt. Die Untersuchung des dabei auftretenden Rekristalli-

sationprozesses diene als Grundlage für die Entwicklung eines Rekristallisationsmodells. Dieses Modell wurde als Erweiterung des oben erwähnten Materialmodells konzipiert, wobei die internen Variablen sowie die Gleichungen für die Mikrostrukturentwicklung weiterverwendet werden können. Ein spezifisches Keimbildungskriterium wurde erweitert, damit das Modell den Zeitpunkt des Rekristallisationsbeginns vorhersagen kann. Das Rekristallisationsmodell berücksichtigt die Keimbildung und das Kornwachstum in Abhängigkeit von der Erholung der Mikrostruktur.

Schließlich wurden beide Modelle erfolgreich in einem Finite Elemente Code für ein industrielles Durchlaufwalzverfahren mit anschließender Wärmebehandlung implementiert.

Contents

Abstract	i
Zusammenfassung	iii
Introduction	1
1 State of the art	5
1.1 Generalities on dislocations	5
1.1.1 Dislocations, slip and plastic deformation	5
1.1.2 Taylor factor	8
1.1.3 Orowan equation	9
1.2 Flow stress and the stages of hardening	10
1.3 Flow stress modelling	12
1.3.1 The Taylor equation	12
1.3.2 The model of Kocks	14
1.3.3 Second phase strengthening	16
1.3.4 Solid solution strengthening	16
1.3.5 Softening due to static recovery	18
1.3.6 Processing conditions	19
1.3.7 Grain and subgrain sizes	21
1.3.8 Additional dislocation densities	23
1.3.9 Evolution rates	25
1.4 Recrystallization modelling	28
1.4.1 The energy of deformation	29
1.4.2 Pressure on a boundary	30
1.4.3 Nucleation	31
1.4.4 Grain growth	32
1.4.5 Recrystallized fraction	32
1.5 Problem formulation	33
2 Materials Characterization	36

2.1	Methodology	37
2.1.1	Plain strain tests	37
2.1.2	Sample preparation for microscopy	39
2.1.3	Microscopic equipment	40
2.1.4	Observation of second-phase particles	40
2.1.5	Annealing tests	42
2.1.6	Grain and subgrain characterization	43
2.2	As received condition characteristics	44
3	Flow stress model	50
3.1	Model set up	50
3.1.1	Microstructure representation	50
3.1.2	Constitutive equation	51
3.1.3	Evolution rates	53
3.1.4	Model parameters	54
3.2	Model results	58
3.2.1	Flow curves and rate parameters	58
3.2.2	Athermal stress, effective stress	63
3.2.3	Dislocation densities	63
3.2.4	Subgrain size	68
4	Recrystallization	70
4.1	Experimental characterization	70
4.1.1	Experiments	70
4.1.2	Experimental results	72
4.2	Recrystallization model	76
4.2.1	Model set-up	76
4.2.2	Model implementation	85
4.3	Results	87
4.3.1	Non-isothermal	87
4.3.2	Isothermal	93
5	Finite element simulations	96
5.1	Implementation of the flow stress model	97
5.1.1	Generalities about flow rules	97
5.1.2	Plane strain compression	98
5.1.3	Multi-pass rolling	102
5.2	Implementation of the recrystallization model	106
5.2.1	Simplified recrystallization model	106
5.2.2	Annealing of samples deformed in plane strain compression	107
5.2.3	Solution annealing after rolling	107

6 Additional Discussion	110
6.1 Deformation behaviour	110
6.2 Recrystallization behaviour	111
6.3 Modelling: further considerations	112
Conclusion	116

Introduction

Nowadays, aluminium and its alloys rank second in consumption volumes among all the metals, surpassed only by steel [1–3]. From packaging to transportation industries, in structural parts and façades or for decorative purposes, in the chemical industry, in constructions, aluminium has become a key component in all kinds of applications. Its low density, corrosion resistance, low temperature formability and recyclability help to reduce the energetic costs. Especially, its excellent strength-to-weight ratio has been the primary factor for the development of the aeronautic and automotive industries.

The 6xxx series aluminium alloys have magnesium and silicon as main alloying elements. They are high strength alloys that are subjected to precipitation strengthening. Although they do not reach the same strength level as alloys from the 2xxx (copper alloyed) and 7xxx (zinc and magnesium alloyed) series, their good weldability and machinability make them very good general purpose alloys. Among them, the 6061 and 6082 alloys are two of the most commonly used, especially in the automotive industry. They are usually found as sheets or extruded products.

The production process of 6xxx series aluminium sheets consists in a succession of thermo-mechanical steps (figure 1) designed to improve the strength of the final product while reaching the desired geometry. The initial billet with its specific chemical composition is produced by continuous or batch casting. Each subsequent step brings irreversible changes in the microstructure that affect directly the mechanical properties of the material.

- I An initial annealing step can be applied in order to homogenize the chemical composition of the billet. The diffusion of solute elements is driven by chemical gradients in the workpiece.
- II After being brought to the working temperature, the billet is hot rolled several times between 550 °C and 450 °C down to a thickness of a couple of centimetres. At this point, the rolling passes are bidirectional to limit the accumulated

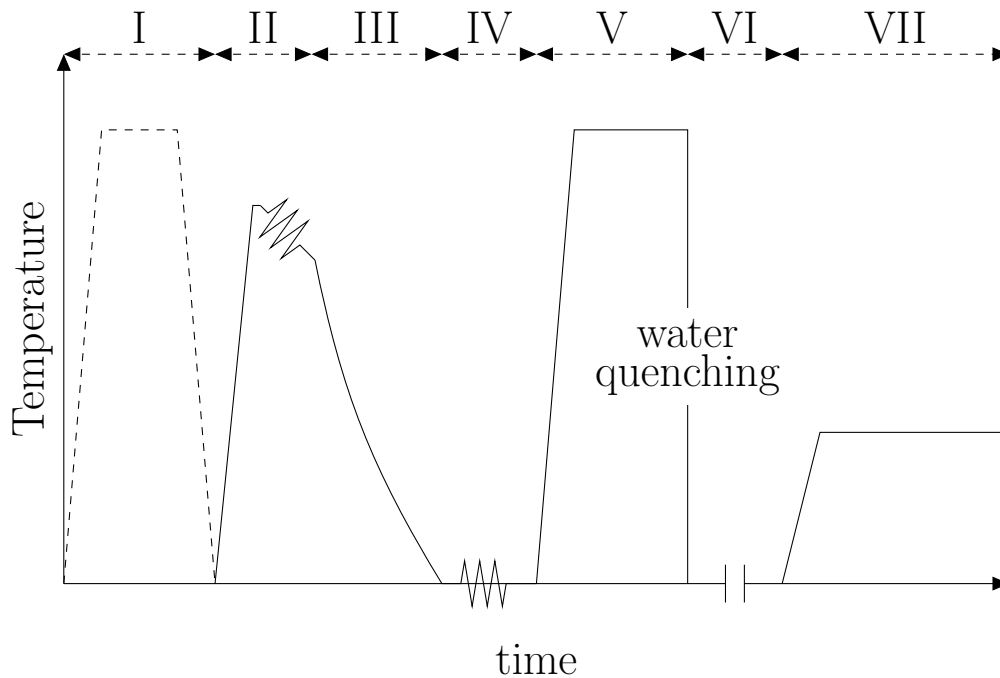


Figure 1: Typical industrial rolling schedule. I: homogenization. II: hot rolling. III: air cooling. IV: cold rolling. V: solution annealing. VI: cold storage. VII: ageing.

strain in the slab. The combination of mechanical work and high temperature induces dynamic recovery and static recrystallization between passes, which preserves the ductility of the material.

- III The plate is then coiled and slowly cooled down in air, leaving enough time for diffusional processes to happen. The occurrences of recovery, recrystallization and grain growth result in a coarse grained microstructure. The particles of second phases, if any, also have time to grow and stabilize, depleting the matrix of solid solution atoms.
- IV The unidirectional multiple passes of cold rolling at room temperature, down to a thickness of a couple of millimeters, strengthen the material by strain-hardening. If necessary, they can be alternated with recrystallization treatments. During cold rolling, the energy of the material is maximized, strengthening it but also reducing its ductility.
- V A solution annealing step at $\sim 580^\circ\text{C}$ is used to dissolve the second phase particles. During this step, the highly strained material recrystallizes. Because of the energy stored during cold deformation, many grains nucleate simultane-

ously and then impinge upon each other during growth. The final grain size is a function of the strain accumulated during cold deformation, the annealing temperature and the annealing time. A recrystallized but finely grained microstructure brings a good balance of mechanical strength and ductility to the material. At the end of the solution annealing, the plate is water quenched in order to keep the alloying elements in solid solution.

- VI After solution annealing and water quenching, the sheet is coiled and stored at room temperature for a couple of days. In alloys 6061 and 6082, diffusional processes happen readily at room temperature. The storage provokes the precipitation of metastable clusters that reduce the ageing potential in the next step.
- VII The final ageing step at temperatures between 150 °C and 250 °C for a couple of hours is designed to promote diffusion. The temperature is sufficient for the nuclei that precipitated in the previous step to slightly coarsen and to form new nuclei, but low enough to keep the second phase particles finely disperse. This ageing step is crucial in hardening the material. The chemical composition of the alloy, the temperature and the time of ageing govern the phase transformations in the material, which in turns governs the precipitation strengthening.

A combination of recrystallized, finely grained and precipitation hardened microstructure brings the best mechanical strength to the sheet while preserving a reasonable ductility for further shaping processes. It is also possible to shape the plate after step V or after step VI, before ageing. This is usually the case for deep drawing in the automotive industry [2].

It is now a well established practice to model the industrial processes with finite element methods. Such models require flow data as an input, i.e. the flow stress of the material with its strain, strain rate and temperature dependency. The strain-stress curves can either be obtained experimentally with simple deformation tests — plane strain compression tests to simulate rolling — over the desired range of temperatures and strain rates, or they can be calculated on the run, either by phenomenological approaches or with physically based models.

Modelling in general can be a powerful tool. It allows to roughly calculate the properties of the final product, which is a great help for designing and improving a production process. Yet, as models can only be as good as our understanding of the physical phenomena they are meant to represent, no model is so far self-sufficient, and an experimental investigation is always needed to validate their output.

Phenomenological approaches consist in setting up a constitutive equation linking

the flow stress to the strain, the strain rate and the temperature, and optimizing it so that it best represents the main features of the flow curves. The equation usually features a power law dependency for the strain and the strain rate, and an activation energy for the thermal dependency. Such models present the advantages of being easy to set up and requiring almost no computational power, but they do not provide any insight on the physics of the problem at hand.

Physical approaches are more deeply connected to the microstructure evolution. It is well-known that during straining and annealing, the microscopic state of the material is modified. This modification depends essentially on the material itself, its initial state and its thermomechanical history. Dislocation multiplication, recovery, recrystallization, phase transformations. . . All those microstructural changes affect directly the resistance of the material, hence its flow stress.

Typically, finite element codes are used to predict the strain, strain rate and temperature distributions in a workpiece during thermomechanical processing, and a routine is called at each time step and each node to calculate and return the microscopic state to the main code.

The present work first deals with modelling the flow stress of an industrial grade Aluminium Alloy 6082 during deformation at room to high temperature, for strain rates ranging from 0.01 s^{-1} to 10 s^{-1} , and based on a microscopic approach. Second, a model for static recrystallization during annealing after cold deformation was developed. It takes the microscopic variables of the constitutive model as input, therefore it is the continuity of the first part. Finally, both models are implemented in the finite element code DEFORM2DTM where they are used to characterize multiple rolling and subsequent recrystallization.

This document is divided into 6 chapters. Chapter 1 reviews the state of the art regarding constitutive microstructure based modelling and recrystallization modelling. From this chapter, the open questions are identified, and the objectives of the present work are elaborated. Chapter 2 concerns the characterization of the alloy used for this study. The methodology for microscopy and some experimental results are presented here. Chapter 3 introduces the constitutive model and its results. The results of the mechanical tests are presented in this chapter, in parallel with those of the model. Chapter 4 deals with recrystallization. A model for calculating the recrystallized grain size and volume fraction is developed. The numerical results are presented together with the experimental measurements for direct comparison. In chapter 5, both models are implemented in the FEM engine DEFORM2DTM. Finally, chapter 6 discusses the yet unaddressed points raised in the previous chapters.

Chapter 1

State of the art

Microstructure based models used to describe material flow and recrystallization behaviour require a certain insight on relevant microscopic features and mechanisms.

The first part of this chapter summarizes the knowledge necessary to further discuss and model the concepts of flow stress and recrystallization.

The second part is a review of the most relevant literature on flow curve modelling.

The third part deals with the microscopic approaches to boundary migration and recrystallization modelling.

1.1 Generalities on dislocations

From this point onward, it is assumed that the reader is familiar with the concepts of dislocations in crystalline materials and deformation by slip. Comprehensive introductions can be found in [4,5]. Section 1.1.1 summarizes the concepts relevant to this thesis.

1.1.1 Dislocations, slip and plastic deformation

Plastic deformation in metallic materials can be achieved in two ways: slip or twinning. Both modes of deformation occur along given crystallographic planes and directions. The stacking fault energy of the material is the determining property in favoring one or the other mode of deformation. Wrought commercial aluminium

alloys with a magnesium content below 3–4 w% possess a high stacking fault energy, which favours deformation by slip.

Slip mode is achieved by the movement of line defects in the microstructure, called dislocations, under the application of a shear stress. Dislocations deform the crystal structure elastically. As such, they carry an elastic strain field and an elastic energy. There are two kinds of dislocations: edge and screw. The Burgers vector of a dislocation determines its unit displacement. The Burgers vector of an edge dislocation is perpendicular to the dislocation line, and that of a screw dislocation is parallel to the dislocation line. The plane formed by a dislocation line and its Burgers vector is called a slip plane; it is the plane in which the dislocation can glide. Consequently, edge dislocations are confined to one plane, whereas screw dislocations are free to glide in any plane containing the dislocations line. In the general case, the dislocations have mixed edge and screw characters.

When a crystal is stressed, the component of the applied stress resolved on a particular slip plane is necessarily a shear stress. Only the resolved shear stress acts on the dislocations and contributes to their motion. The applied stress is related to the resolved shear stress by the Schmid factor (section 1.1.2). When the resolved shear stress reaches a critical value, the dislocations start moving and plastic deformation occurs. In a single crystal, the resolved shear stress is usually larger on a particular slip system, called the *primary* slip system. It is the slip system on which dislocations glide preferentially. The other slip systems are called *secondary* slip systems.

Dislocations located on secondary slip planes intersect the primary slip plane; they are called *forest* dislocations with respect to the primary slip system. The intersection of mobile dislocations with forest dislocations leads to the formation of jogs, which are steps in the dislocation lines. Those jogs effectively increase the length of the dislocations, thus they increase the energy of the material. In addition, the jogs exert an attractive force on the mobile dislocations. In consequence, the stress required to create a jog and break the mobile dislocation free from them is greater than the shear stress needed for unhindered dislocation glide.

When a mobile mixed dislocation encounters an obstacle on its slip plane, for example an unsharable second-phase particle, its screw character can overcome the obstacle by gliding in a secondary slip plane. This phenomenon is called *cross-slip*. It plays a primordial role in the plastic deformation and the strain-hardening behaviour of commercial aluminium alloys.

The mechanisms of jog formation and cross-slip can both be eased with thermal activation. In other words, the stress required to create jogs or move edge dislocation out of their slip plane can be reduced by increasing the working temperature.

Mobile dislocations can be immobilized in several ways. They can encounter an obstacle that they cannot bypass. This leads to dislocation pile-up and stress localization. Upon applying a higher shear stress, the obstacle might be overcome by cross slip. Mobile dislocations can also reach a configuration of lower energy by forming a dipole with another dislocation of opposite sign, initially gliding on a parallel slip plane but in the opposite direction. When a dipole forms, both dislocations stop gliding and get stored in the microstructure.

In high stacking fault materials, the stored dislocations have been shown to rearrange in dislocation entanglements, forming regions of high dislocation density and leaving the rest of the matrix almost depleted of stored dislocations. Those peculiar structures are called dislocation cells [6]. Upon further deformation, the dislocations within the cell walls organize into a regular structure of even lower energy. The cells turn into subgrains, whose walls are called low angle grain boundaries (LAGBs) because they delimit regions of a grain misoriented by a small angle — of the order of $1 - 15^\circ$. In contrast, grain boundaries in polycrystals have a misorientation greater than $10 - 15^\circ$ and are called high angle grain boundaries (HAGBs).

Mobile dislocations get absorbed by grain boundaries when they arrive into one, but not necessarily by subgrain boundaries. In fact, the main trapping mechanism is dipole formation. The mobile dislocations can travel across several subgrains before being stored in the microstructure. Nes [7] demonstrated statistically that the mean free path L of a moving dislocation varies inversely as the square root of the dislocation density ρ :

$$L \propto \rho^{-1/2} \tag{1.1}$$

The dislocation density in crystalline materials is usually defined as the length of dislocation line per unit volume, and it is expressed in m m^{-3} , or m^{-2} .

During deformation, not only do the dislocations travel and get stored, but they also multiply and annihilate. The Frank and Read mechanism, where a dislocation segment pinned at both ends by two obstacles is bent until it emits a dislocation loop, depicts a self regenerative source of mobile dislocations. Annihilation happens when two edge dislocation segments of opposite signs meet each other on the same slip plane. It can happen by glide when the two opposite dislocations travel readily on the same slip plane where they eventually meet, or by climb. Climb is a diffusive process that allows dislocations to travel between parallel slip planes by emission or absorption of vacancies. Because of its diffusive nature, climb is a strongly time and temperature dependent process. Although Nes [7] argued that room temperature climb cannot be completely disregarded, it is widely accepted

that dislocation annihilation at room temperature occurs almost exclusively by glide. This means that plastic deformation is necessary at room temperature for dislocation annihilation. At higher temperatures, the diffusional barriers for vacancy migration vanish and both annihilation by glide and by climb are permitted. One must however take into account the deformation rate. When dealing with creep, the strain rate is so low (typically 10^{-12} to 10^{-10} s $^{-1}$ for dislocation creep) that climb is often considered the main annihilation process. In industrial rolling, where strain rates can be greater than 100 s $^{-1}$, annihilation happens almost only by glide, even at high temperatures.

Dislocations are line defects whose that deform the crystal lattice elastically. As such, they carry an elastic strain field and an elastic energy. When dislocations exit the crystal or annihilate, either by glide or by climb, their strain energy is removed from the microstructure. When they re-arrange in a subgrain structure, their strain fields interfere with each other to reduce the stored energy. A reduction in stored energy, whether it comes from dislocation annihilation or re-arrangement in subgrain boundaries, is called *recovery*. Cross-slip and climb greatly promote recovery in that they increase the chances for dislocations to meet other dislocations and annihilate, or to re-arrange to form subgrains.

1.1.2 Taylor factor

As mentioned before, dislocations glide under the effect of an applied shear stress, in planes of given orientations. A slip system is defined as a set of symmetrically identical slip planes associated with a slip direction. In FCC crystals such as aluminium, there is a total of 12 slip systems, of whom a minimum of 5 must be active to accommodate any arbitrary deformation [5].

Single crystals can be sheared on a single slip system. The applied stress however is not necessarily parallel to the slip system. The component τ_k of the applied stress resolved on a given shear system is related to the applied macroscopic stress σ by the Schmid factor m [5]:

$$\sigma = \tau_k / m \tag{1.2}$$

In polycrystals, the macroscopic applied stress σ cannot be related to the resolved shear stress on a given slip system. Instead, it has to be related to the average resolved shear stress τ in all the active slip systems [8,9]. The Taylor factor M replaces the Schmid factor:

$$\sigma = M\tau \quad (1.3)$$

Let us call γ_k the total slip on a given slip system k and ϵ the macroscopic strain. For infinitesimal deformation steps, the Taylor factor is defined as:

$$M = \frac{\sum_k d\gamma_k}{d\epsilon} \quad (1.4)$$

In FCC polycrystals with randomly oriented grains, the Taylor factor is equal to 3.06. Equation (1.3) is often rewritten as [7, 10]:

$$\sigma = \sigma_0 + M\tau \quad (1.5)$$

Where σ_0 is a practical constant serving as a buffer for all contributions to the yield stress of the material that are not addressed specifically when defining τ . σ_0 is not always explicitly defined, in which case it can be taken equal to 0.

1.1.3 Orowan equation

Let us consider a single crystal populated with uniformly distributed mobile dislocations of density ρ_m and sheared with an applied resolved shear stress τ . The total shear strain γ resulting from the movement of the dislocations across the crystal is given by the Bailey-Orowan equation [11]:

$$\gamma = \rho_m b \bar{l} \quad (1.6)$$

The dislocations move a distance \bar{l} in average. Note that \bar{l} is not necessarily equal to the mean free path L of dislocations. It is the average distance traveled by mobile dislocations to achieve the plastic strain γ . At very small strains, $\bar{l} < L$. At larger strains, \bar{l} is not bound. b is the norm of the Burgers vector, usually taken equal to the lattice parameter. The time derivative of equation (1.6) reads:

$$\dot{\gamma} = \dot{\rho}_m b \bar{l} + \rho_m b \dot{\bar{l}} \quad (1.7)$$

Where $\dot{\gamma}$ is the shear strain rate and $\dot{\bar{l}}$ the average dislocation velocity. The rate of variation of the mobile dislocation density is usually believed to be slow in front of the variation of the average slip distance, therefore equation (1.6) is often simplified as:

$$\dot{\gamma} = \rho_m b \bar{v} \tag{1.8}$$

Note that equation (1.8) *assumes implicitly* that the density of mobile dislocation remains constant during deformation ($\partial \rho_m / \partial t = 0$).

1.2 Flow stress and the stages of hardening

The level of stress necessary to start deforming plastically metallic materials is called the *yield stress*. As deformation proceeds, the level of stress necessary to keep the material flowing is called the *flow stress*. When deformation occurs by glide, the yield stress is the stress that needs to be applied to set the mobile dislocations in motion, and the flow stress is the stress required to keep them moving.

During deformation, the multiplication and the storage of dislocations lead to an increase in the flow stress called *strain hardening* (or *work hardening*). The gliding dislocations interact with the surrounding stored dislocations which hinder their motion. The densification of the network of stored dislocations leads to strain hardening. At a given deformation temperature T and a given resolved shear rate $\dot{\gamma}$, the strain hardening is defined as:

$$\Theta := \left. \frac{\partial \tau}{\partial \gamma} \right|_{\dot{\gamma}, T} \tag{1.9}$$

In opposition, recovery, whether it comes from dislocation annihilation or cell and subsequent subgrain formation, tends to soften the microstructure by releasing its stored energy of deformation and to balance the strain hardening.

The flow stress is often plotted with respect to the macroscopic strain, at a given temperature and a given strain rate. Such a plot is known as a *flow curve*. Another useful representation is that of the strain hardening as defined in equation (1.9) with respect to the shear stress of the material, which is referred to as a Kocks-Mecking plot [7]. Because the shear stress / strain of a polycrystalline material is related to its macroscopic stress / strain by only the Taylor factor, and because M is often taken as a constant, it makes no qualitative difference whether we use the shear or the macroscopic stress / strain in the flow curves, or in the Kocks-Mecking plots.

Typically, the strain hardening of cell forming face centred cubic alloys such as aluminium alloys can be divided in four main stages (figure 1.1). Descriptions of the stages of work hardening can be found in [12, 13].

- Stage I, also called “easy glide”, corresponds to the glide of mobile dislocations on a single slip system in single crystals. It occurs only in well recovered single crystals, when the microstructure is still very much free of stored dislocations. Therefore the mobile dislocations can glide almost unhindered, leading to quite large strains, up to 0.6. The hardening in stage I is low, on the order of $2 \times 10^{-4}\mu$, where μ is the shear modulus. It is mostly due to the formation of dislocation dipoles. Stage I cannot be observed during the deformation of polycrystals, thus will not be given further attention here. It is however of great importance when modelling creep hardening [14].
- Stage II onsets right after stage I in single crystals, and at the beginning of plastic deformation in polycrystals. The accumulation and pile up of dislocations on the primary slip system build up a resolved shear stress on secondary slip systems. When that shear stress becomes greater than a critical value, dislocations can then cross slip and glide on the secondary slip systems. Secondary slip presumably relaxes the stress concentration on the primary slip system, but leads to the formation of jogs as a result of the interactions of dislocations gliding on different slip systems. The hardening rate in stage II is constant and rather large, on the order of $\mu/200$ [7, 12], and depends weakly on the temperature or the strain rate [15]. This results in a linear increase in flow stress as the deformation proceeds.
- Stage III onsets as the flow stress deviates from linearity with respect to the strain. It is associated with dynamic recovery and the formation of dislocation cells (and eventually subgrains). The strain hardening decreases monotonically with increasing stress. In contrast to stage II, stage III behaviour is strain rate sensitive and highly temperature sensitive. At high deformation temperatures, the hardening eventually cancels and stage III ends with a flow stress saturation. The subsequent deformation at constant flow stress is called *steady-state*.
- Stage IV was intensively reviewed in [12, 16]. It typically characterizes the behaviour at room temperature after stage III, where the flow curves present a constant and low hardening of about $2 \times 10^{-4}\mu$, much like in Stage I. Several causes have been proposed for the sustained hardening, such as grain or subgrain size refinement, plastic instabilities, stress induced transformations, etc. The mechanisms responsible for the stage IV behaviour are however still unclear. At high temperatures, a steady-state is reached at the end of stage

III and stage IV is not achieved. At moderate temperatures, an intermediate state between stage IV and steady-state is achieved.

Zehetbauer and Seumer reported systematic flow stress saturation at room temperature at very large strain, typically greater than 4 – 5 [17]. That is sometimes understood as the onset of a fifth stage followed by a steady-state at room temperature. When the deformation temperature increases, diffusional mechanisms such as dislocation climb are promoted, and part of the energy necessary for mobile dislocations to overcome the local obstacles they meet on their way through the crystal is provided by heat. The overall hardening decreases in intensity, leading to the onset of a steady-state regime at high temperatures.

Typical examples of a) flow curves and b) Kocks-Mecking plots for increasing temperatures are given in figure 1.1, after [7]. In this figure, τ_i is the yield stress of the material. τ_{III} to τ_S , respectively γ_{III} to γ_S , are the critical resolved shear stresses, respectively resolved shear strains, for the onsets of stages III to saturation. Those critical stresses have been thoroughly investigated [7] and decrease with the temperature.

1.3 Flow stress modelling

In 1934, Taylor introduced the movement of dislocations as a mechanism for plastic deformation and formulated the expression of the shear stress of the material [18]. His theory is supported by experimental evidence [19, 20] and has been used as basis for all subsequent models. One of the most successful flow stress models was developed by Kocks in 1976 [21]. It sets a model structure that has since been used as a standard. Typically, a flow stress model consists in:

1. A set of independent internal variables used to describe the microstructure.
2. A constitutive equation relating the flow or the shear stress of the material to the microscopic variables and the processing conditions.
3. A set of rate equations for the internal variables.

1.3.1 The Taylor equation

Edge dislocations of opposite signs gliding on parallel slip planes exert an attractive force on each other that is inversely proportional to the distance between the slip planes. In [18], Taylor argued that single crystals deform plastically when the

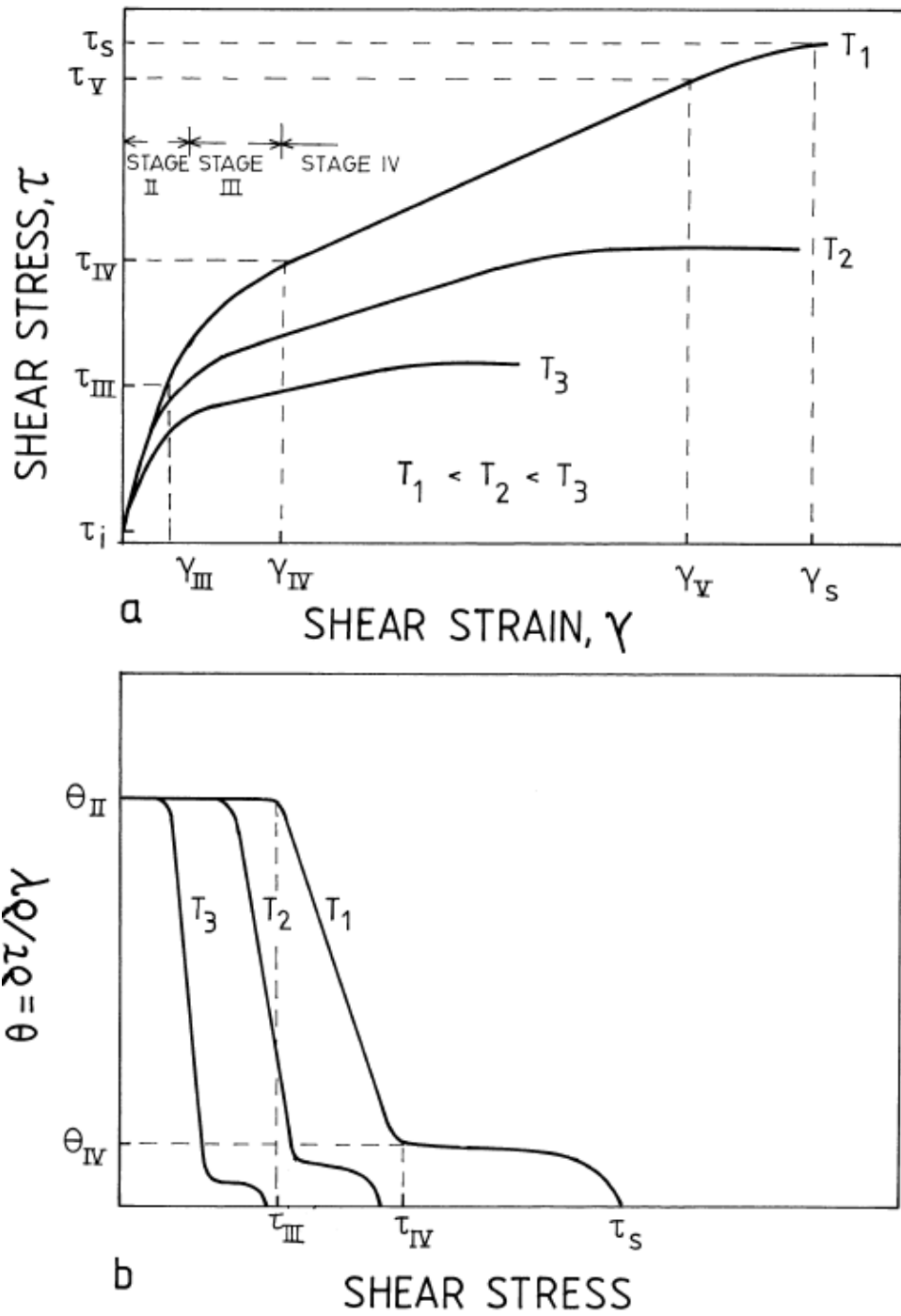


Figure 1.1: The stages of work-hardening, after [7]. Typical a) flow curves for increasing temperature and b) corresponding Kocks-Mecking plots.

resolved shear stress is sufficient to break two edge dislocations free from each other's attraction. The Taylor equation reads:

$$\tau = \tau_{ath} = \frac{\alpha_1 \mu b}{\lambda_\rho} \quad (1.10)$$

α_1 is a stress constant in the range 0.1–1 and λ_ρ is the distance between stored dislocations, usually written as:

$$\lambda_\rho = \rho^{-0.5} \quad (1.11)$$

The shear stress is labeled *athermal* to emphasize the fact that it is almost independent of the deformation temperature, except for the small variations in μ . b also varies with the temperature, but its variation is negligible compared to that of μ [13]. Because the flow stress actually depends on the processing conditions, a more useful form of equation (1.10) should include a temperature and strain rate dependent term.

1.3.2 The model of Kocks

In his model [21], Kocks features the stored dislocation density ρ as single internal variable in an attempt to model saturating flow stresses in stage III hardening. The shear stress is given by:

$$\tau = \tau_{ath} s(T, \dot{\epsilon}) \quad (1.12)$$

Recalling equation (1.3), the constitutive equation reads:

$$\sigma = M \tau_{ath} s(T, \dot{\epsilon}) \quad (1.13)$$

The function $s(T, \dot{\epsilon})$ accounts for the processing conditions, namely the temperature T and the strain rate $\dot{\epsilon}$. The expression *structure parameter* has been used by Estrin in e.g. [22] to refer to the microstructure contribution to the flow stress, i.e. to τ_{ath} in equation (1.13). The deviations from the intrinsic material strength due to the process conditions are all accounted for by s . The latter describes the ratio of flow stress for a fixed microstructure at different temperatures and strain rates. Kocks only writes that:

$$s = s \left(k_B T \ln \left(\frac{\dot{\epsilon}}{\dot{\epsilon}_0} \right) \right) \quad (1.14)$$

With k_B the Boltzmann constant and $\dot{\epsilon}_0$ a normalization strain rate. The argument of s is the combination expected from the thermal activation theory. Estrin in [22] relates s to the strain rate sensitivity m^* of the material via:

$$s = \left(\frac{\dot{\epsilon}}{\dot{\epsilon}_0} \right)^{m^*}, \quad m^* = \left. \frac{\partial \ln \sigma}{\partial \ln \dot{\epsilon}} \right|_{T, \epsilon} \ll 1 \quad (1.15)$$

Where m^* is generally a function of the temperature, as is $\dot{\epsilon}_0$. This approach clearly separates the effects on the flow stress of the microstructure from those of the processing conditions.

At given processing conditions, the hardening in stage III decreases linearly with the shear stress. One can write:

$$\frac{\partial \tau_{ath}}{\partial \gamma} = K - K' \tau_{ath} \quad (1.16)$$

K and K' being model constants. Recalling equation (1.10), it comes:

$$\frac{\partial \rho}{\partial \gamma} = \frac{2K}{\alpha_1 \mu b} \sqrt{\rho} - 2K' \rho \quad (1.17)$$

Or equivalently:

$$\frac{\partial \rho}{\partial t} = \dot{\gamma} \left(\frac{2K}{\alpha \mu b} \sqrt{\rho} - 2K' \rho \right) \quad (1.18)$$

Equation (1.18) can be reformulated in the more general form:

$$\frac{\partial \rho}{\partial t} = \left(\frac{\partial \rho}{\partial t} \right)^+ - \left(\frac{\partial \rho}{\partial t} \right)^- \quad (1.19)$$

The + identifies a storage term and the – an annihilation term. Note that Kocks did not introduce any specific mechanism for those two phenomena. Rather, he reached the same expression as in equation (1.17) by stating that the mobile dislocations would statistically become stored after traveling their mean free path, and that some of the stored dislocations would annihilate when contacting a recovery

site. In any case, the evolution rates are temperature and strain rate independent (except for the small thermal variations of b and μ). They represent the evolution of an ever similar microstructure with respect to the deformation conditions.

1.3.3 Second phase strengthening

A common addition to almost every model dealing with multiple-phase alloys [5, 9, 23–25] is the contribution of second-phase particles to the flow stress of the material. It comes under the form of an extra shear stress τ_d :

$$\tau = \tau_{ath} + \tau_d \quad (1.20)$$

The expression of τ_d varies from one model to another, but it is always based on the well known Orowan stress:

$$\tau_d = \frac{\chi\mu b}{\lambda_d} \quad (1.21)$$

Where χ is a constant of the order of unity and λ_d is the inter particle spacing in the slip plane. Nes *et al.* [24] and Kabliman and Sherstnev [25] use another expression based on the calculation of Ashby [26]:

$$\tau_d = \frac{\chi'\mu b}{1.24 \times 2\pi \lambda_d} \ln \left(\frac{\lambda_d}{b} \right) \quad (1.22)$$

With χ' a constant of the order of unity.

If the particles are arranged on a square lattice, then λ_d is:

$$\lambda_d = N_S^{-1/2} \quad (1.23)$$

N_S is the surface density of particles intersecting the slip plane.

1.3.4 Solid solution strengthening

Point defects, i.e vacancies, self-interstitial atoms and alloying elements in solid solution distort the surrounding matrix elastically and can interact with nearby

dislocations. Spherical point defects and edge dislocations have an interaction energy E_I given by [5, 27]:

$$E_I = \frac{4}{3}\mu br_a^3\eta \frac{1 + \nu \sin \theta}{1 - \nu} \frac{1}{r} \quad (1.24)$$

Where (r, θ) are the polar coordinates of the point defect relative to the dislocation line, θ being measured from the slip direction, ν is the Poisson coefficient of the matrix, and r_a and $r_a(1 + \eta)$ are the atomic radius of the matrix and the radius of the point defect. η is then seen as a misfit parameter between the two radii. It is found to be maximized for interstitial atoms, falling in the range 0.1 – 1.0 [5]. The sites of minimum interaction energy, i.e. maximum binding energy, are within the dislocation core at $\theta = 3\pi/2$ and $r \approx b$. Thus interstitial atoms tend to segregate in the dislocation cores, provided that they have time to diffuse. The equilibrium defect concentration c near the dislocation of a dilute solution of point defects reads [27]:

$$c = c_0 \exp\left(\frac{-|E_I|}{k_B T}\right) \quad (1.25)$$

c_0 being the concentration of solutes far away from the dislocation. Assuming that each interstitial in the dislocation core exerts a local pinning force (local-force model in [5]), an additional shear stress τ_{ss} needs to be applied to unlock the dislocations:

$$\tau_{ss} \approx 0.13\mu\sqrt{c} \quad (1.26)$$

And the resolved shear stress becomes:

$$\tau = \tau_{ath} + \tau_d + \tau_{ss} \quad (1.27)$$

Several remarks have to be done here. First, we have only considered one type of interstitial, i.e. one alloying element. Each type of interstitial atom has its own misfit parameter and its own interaction energy with the dislocations. In a commercial alloy, the different kinds of solute atoms do not have the same pinning effect on the dislocation, and τ_{ss} must take into account the concentrations of all solute elements. Second, τ_{ss} is directly linked to τ_d for the former decreases in magnitude when the atoms in solutions migrate toward the second phase particles. In general, $\tau_{ss} \ll \tau_d$ [5], thus τ_{ss} only needs to be included in equation (1.27)

when the matrix is depleted of second-phase particles, like after solution annealing. Finally, when dislocations break free from the solute atoms and glide away, equation (1.25) does not hold any more unless the temperature is high enough and the strain rate low enough to allow the solute atoms to diffuse faster than the dislocations move and repeatedly lock them.

1.3.5 Softening due to static recovery

One inconvenient of the model of Kocks is that it is limited to the description of dynamic phenomena. Indeed when $\dot{\gamma} = 0$, equation (1.18) cancels out. Thus, no static recovery by climb is allowed. This might not be a problem during deformation, where all dynamic effects prevail, but needs to be addressed after deformation at high temperature for example, when a non negligible fraction of dislocations annihilate. Recovery softens the material and reduces the yield stress as the latter depends explicitly on the dislocation density. A static recovery coefficient C_r can be added to the evolution rate:

$$\frac{\partial \rho}{\partial t} = \dot{\gamma} \left(\frac{2K}{\alpha_1 \mu b} \sqrt{\rho} - 2K' \rho \right) - C_r \quad (1.28)$$

Estrin [23] advises to use a coefficient with the general form:

$$C_r = C_r^0 \exp \left(-\frac{Q_0}{k_B T} \right) \sinh \left(\frac{\beta_0 \sqrt{\rho}}{k_B T} \right) \quad (1.29)$$

Where C_r^0 , Q_0 and β_0 are constant parameters to be optimized by comparison with experiments. Considering that any annihilation event occurring after deformation must be driven by climb mechanisms acting on the edge component of the dislocation stored during deformation, one can calculate another recovery coefficient based on the climb forces acting on the dislocation segments [5]. Caillard and Martin [28] studied intensively the thermally activated mechanisms in crystal plasticity and came up with a coefficient of the form:

$$C_r = C_r^1 \frac{\mu b^3}{\pi (1 - \nu)} \frac{D}{k_B T} \rho^2 \quad (1.30)$$

C_r^1 is a constant to be optimized and D is the diffusion coefficient with an Arrhenius form:

$$D = D_0 \exp\left(\frac{Q_{diff}}{k_B T}\right) \quad (1.31)$$

D_0 being the Arrhenius coefficient. This form was used by Kablman and Sherstnev in [25]. Note that the diffusion coefficient can be that of bulk diffusion or that of pipe diffusion, according to the dominant mechanism for the diffusion of vacancies.

1.3.6 Processing conditions

Another issue that has to be properly addressed is the influence of the strain rate and the temperature on the flow stress of the material — dealt with by the function $s(T, \dot{\epsilon})$ in equation (1.13).

With equation (1.15), Kocks, Mecking and Estrin include the strain rate sensitivity in the expression of the flow stress [21–23, 29]. Such an approach has proven successful to model high temperature deformation and creep. It is however unsatisfactory in that it does not ensue from any physical mechanism, but rather follows on from phenomenological features in the flow curves.

[7, 9, 30, 31], among others, make use of the concept of local obstacles to the dislocation movement. This concept is broken down in [5]. It is born from the idea that the flow stress results i) from long range interactions between mobile and stored dislocations through their elastic field (Taylor, equation (1.10)), and ii) from the necessity for mobile dislocations to bypass local, short range obstacles when they encounter them physically. The short range obstacles present energy barriers that can be overcome by thermal activation, thus their contribution to the flow stress is highly temperature dependent.

Suppose that a dislocation segment moving in the x direction is stopped at a position x_1 by some local obstacle. The obstacle exerts a resisting force F on the dislocation line. In order for the dislocation to move to a position x_2 after the obstacle, it must overcome the energy barrier Q_{act} presented by the obstacle :

$$Q_{act} = \int_{x_1}^{x_2} F dx \quad (1.32)$$

Part of this energy, the Gibbs energy of change ΔG between positions x_1 and x_2 , can be provided by thermal activation. The remainder has to be supplied by mechanical work, i.e. an extra shear stress τ_{eff} has to be applied, which produces a force $\tau_{eff}b$ per unit length on the dislocation line. Figure 1.2 presents the simple

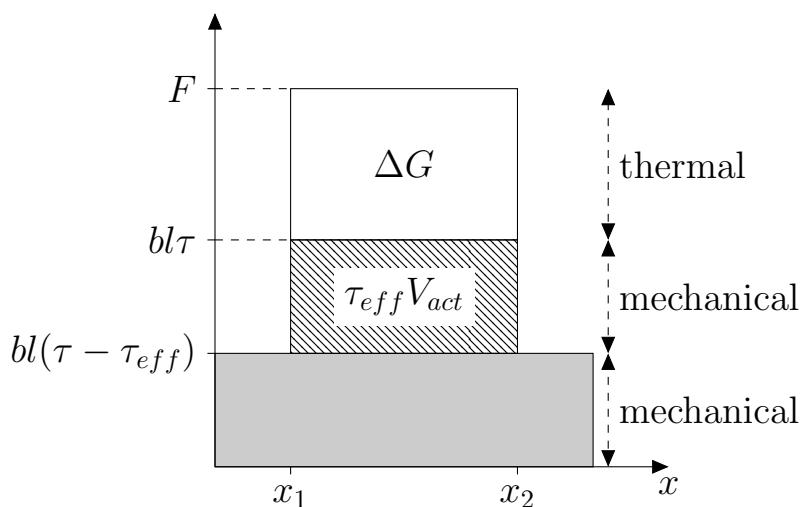


Figure 1.2: Profile of the resistance force F versus distance x for a square barrier opposing the dislocation motion. The shaded area is the energy provided by the long range stresses. To travel from x_1 to x_2 , the dislocations need some extra energy. The hashed area is the energy provided by the effective stress, and the white area is the thermal energy.

case of a square energy barrier, when the obstacles oppose a constant resisting force to the dislocation motion. Let λ be the spacing of the obstacles along the dislocation line, the effective forward force on the line per obstacle is $\tau_{eff}b\lambda$, and the work done by τ_{eff} when the dislocation moves from x_1 to x_2 is $\tau_{eff}b\lambda(x_2 - x_1)$. $b\lambda(x_2 - x_1)$ has the dimension of a volume and is called the activation volume V_{act} for convenience. Q_{act} reads:

$$Q_{act} = \Delta G + \tau_{eff}V_{act} \quad (1.33)$$

Or equivalently:

$$\Delta G = Q_{act} - \tau_{eff}V_{act} \quad (1.34)$$

If the dislocation line vibrates at the attack frequency ν_{att} (it “attacks” the obstacle at that frequency), its probability to successfully overcome the energy barrier of the obstacle at temperature T is given by the Boltzmann factor $\exp(-\Delta G/k_B T)$, provided that $\Delta G \gg k_B T$. Therefore the dislocation velocity \bar{v} reads:

$$\bar{v} = \bar{d}\nu_{att} \exp\left(-\frac{Q_{act} - \tau_{eff}V_{act}}{k_B T}\right) \quad (1.35)$$

ν_{att} is often assimilated to ν_D , the Debye vibrational frequency of the atoms near the dislocation line ($\nu_D \approx 1.5 \times 10^{13} \text{ s}^{-1}$ for aluminium), although Granato *et al.* [32] argue that the attack frequency can differ from the Debye frequency by several orders of magnitude. Roters *et al* [9] use the value $7.8 \times 10^9 \text{ s}^{-1}$. \bar{d} is the average distance moved for each obstacle overcome. The following phenomenological form is often preferred to equation (1.35) [7, 9, 23]:

$$\bar{v} = \bar{d}\nu_{att} \exp\left(-\frac{Q_{act}}{k_B T}\right) \sinh\left(\frac{\tau_{eff} V_{act}}{k_B T}\right) \quad (1.36)$$

Note that since the energy barrier stops at position x_2 , once a dislocation arrives at x_2 , it is then free to move until the next obstacle. Thus \bar{d} is usually larger than $x_2 - x_1$. If we assume that:

1. The forest of stored dislocations is the major obstacle to mobile dislocations.
2. The distance \bar{d} is a lot larger than $(x_2 - x_1)$.
3. It takes a lot more time to overcome the obstacle than to travel the distance \bar{d} .

Then \bar{d} is equal to the spacing of forest dislocations in the slip direction and is inversely proportional to $\sqrt{\rho}$. If the dislocations intersect the slip plane randomly, then $\bar{d} = \lambda$.

Combining equations (1.3), (1.8) and (1.35), the effective shear stress is given by:

$$\tau_{eff} = \frac{Q_{act}}{V_{act}} + \frac{k_B T}{V_{act}} \ln\left(\frac{M\dot{\epsilon}}{\rho_m b \bar{d} \nu_{att}}\right) \quad (1.37)$$

Since the logarithmic part is negative, the effective stress decreases when the temperature increases. This means that the more the energy provided by heat increases, the less need there is for mechanical energy to be provided to overcome Q_{act} . Therefore there is a critical temperature above which τ_{eff} cancels out. If the strain rate increases however, the logarithmic part increases closer to 0 and τ_{eff} rises.

The total shear stress becomes:

$$\tau = \tau_{ath} + \tau_d + \tau_{ss} + \tau_{eff} \quad (1.38)$$

All the information related to the deviations of the microstructure resistance to plastic straining due to temperature and strain rate is now included in τ_{eff} . There

is no need for the processing function $s(T, \dot{\epsilon})$ any more.

1.3.7 Grain and subgrain sizes

The major limitation of saturating one-variable models is precisely that they are designed to saturate. The modelling of stage III hardening inevitably leads to a flow stress saturation because the strain hardening eventually cancels out (equation (1.16)). In effect, all one-variable models based on the Kocks design are bound to follow the same trend, making them suitable for high temperature deformation, but unable to represent the persistent stage IV hardening at moderate to low temperatures. The way to get around this problem is to introduce additional internal variables having their own evolution rates. At least two variables must be independent, otherwise the problem remains. It is important for the variables to have saturating kinetics, because we do not want the material to harden indefinitely. However their kinetics should be different in order to account for the multi-stage hardening seen in figure 1.1.

It is common to use the subgrain equivalent diameter as second internal variable [7, 33–35]. Gil Sevillano *et al.* [16] assembled subgrain size measurements during deformation at room temperature from various authors (figure 1.3). They found that a wide range of pure metals exhibited a similar behaviour. Let us call δ the subgrain size and $\delta_{1.5}$ the subgrain size at a strain of 1.5. [7] gives the relationship:

$$\frac{1}{\delta} = (0.7 + 0.09\gamma) \delta_{1.5} \quad (1.39)$$

Of course this relationship holds only at room temperature. At moderate to high temperatures, it is necessary to set up an evolution rate similar to equation (1.18). Alternatively, the subgrain size during steady-state deformation can be related to the Zener-Hollomon parameter [34]. The subgrain size must then be included in the constitutive equation as an additional contribution to the shear stress τ_δ :

$$\tau_\delta = \frac{\alpha_2 \mu b}{\delta} \quad (1.40)$$

α_2 being a proportionality constant.

If the grain size δ_g is comparable to the subgrain size, the contribution of grain boundaries to the shear stress τ_g can be defined in a similar fashion:

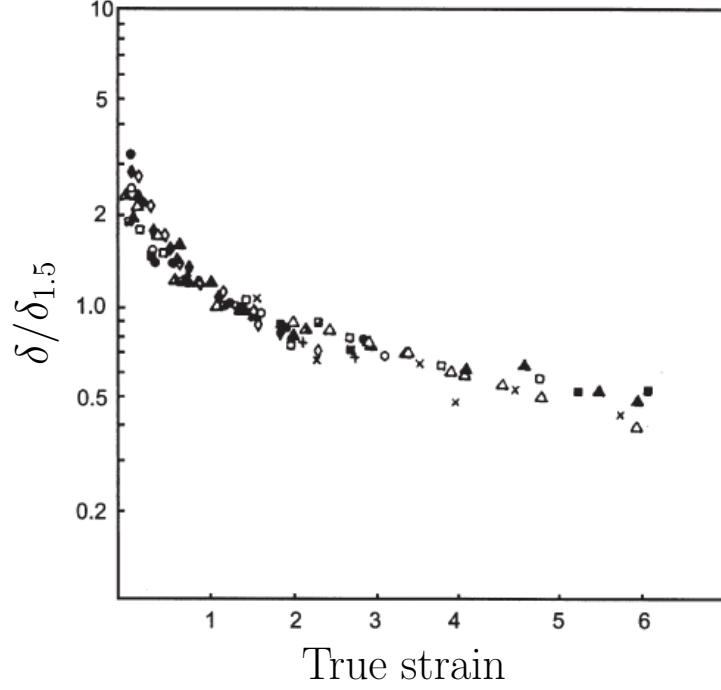


Figure 1.3: Cell/subgrain size evolution during deformation of Al, Cu, Ni, Fe, Cr and Nb, from [7], adapted from [16]. The subgrain size is normalized by the subgrain size at a strain of 1.5.

$$\tau_g = \frac{\alpha_3 \mu b}{\delta_g} \quad (1.41)$$

α_3 being a proportionality constant. The evolution rate for the grain size however is far from trivial and will not be reported here. In order to be assessed correctly, it requires a texture model [36–38], seeing as the grains in a polycrystal do not deform homogeneously.

The total shear stress becomes:

$$\tau = \tau_{ath} + \tau_d + \tau_{ss} + \tau_{eff} + \tau_\delta + \tau_g \quad (1.42)$$

In the general case where the grains are much bigger than the subgrains, τ_g can be neglected in front of τ_δ (assuming that α_2 and α_3 do not differ too much).

1.3.8 Additional dislocation densities

A second common way to introduce additional internal variables is to divide the dislocations in several types, each having its own density and its own kinetics. Since the work of Mughrabi [39], it is common to represent the microstructure by a juxtaposition of subgrains, whose interiors and walls are populated with dislocations of respective densities ρ_i and ρ_w [9,30,31]. Let us emphasize that those are the densities of dislocations *within* the subgrain interior (respectively walls). They have to be multiplied by the volume fraction of interiors (respectively walls) to give the actual volume densities.

Additionally, according to the Orowan equation (1.8), almost all the models feature the mobile dislocations of density ρ_m to account for the plastic deformation, even though ρ_m is not always considered as a variable.

With several types of dislocations, the definition of the athermal stress becomes less trivial. Let us call f_w the fraction of walls ($0 < f_w < 1$), the stored dislocation density now reads:

$$\rho = (1 - f_w) \rho_i + f_w \rho_w \quad (1.43)$$

Thus combining equations (1.10), (1.11) and (1.43) yields:

$$\tau_{ath} = \alpha_1 \mu b \sqrt{(1 - f_w) \rho_i + f_w \rho_w} \quad (1.44)$$

Even though there is experimental evidence that the Taylor model holds for cell forming alloys, it describes mobile dislocations traveling in the vicinity of isolated stored dislocations. Thus it is not adapted to the interaction with cell wall dislocations. Argon [40] uses the following equation instead:

$$\tau_{ath} = \alpha_1 \mu b ((1 - f_w) \sqrt{\rho_i} + f_w \sqrt{\rho_w}) \quad (1.45)$$

It is also sometimes considered that the Taylor model holds only for the cell interiors, and that the contribution of wall dislocations has to be treated completely differently [7,41]. In that case, τ_{ath} becomes:

$$\tau_{ath} = \alpha_1 \mu b \sqrt{(1 - f_w) \rho_i} \quad (1.46)$$

With that last expression for ρ_i , Nes and co-workers tend to link the wall dislocation density to the subgrain size with an equation of the type $\rho_w \propto \delta^{-1/2}$ and use

equations (1.39) and (1.40). Sandström and Lagneborg [42] use equation (1.46) with $f_w = 0$ — effectively the Taylor equation in which ρ is replaced by ρ_i , arguing that the wall dislocation density does not contribute to harden the material. This might hold at high deformation temperatures, but cannot be retained at low and moderate temperatures where stage IV hardening is promoted by the subgrain refinement.

Gottstein, Roters and co-workers argue that there are much more obstacles to mobile dislocations within the cell walls than within the cell interiors. Therefore they use a hybrid model [9] consisting of two shear stresses τ_i and τ_w , one for each region, defined as:

$$\tau_x = \alpha_1 \mu b \sqrt{\rho_x} + \tau_{eff_x} \quad (x = i, w) \quad (1.47)$$

τ_{eff_x} is obtained by replacing \bar{d} in equation (1.37) by d_x , the forest dislocation spacing in the region of interest (typically, $d_x \propto \rho_x^{-0.5}$). The shear stress is then given by:

$$\tau = (1 - f_w) \tau_i + f_w \tau_w + \dots \quad (1.48)$$

Where the ellipsis stands for other contributions that are not related to the dislocations.

Estrin and co-workers use a processing function as defined in equation (1.13) and Kocks' or Argon's approaches for the athermal stress [22, 43], depending on the number of variables their models feature.

In general, the shear stress is expressed as a combination of the expressions mentioned above. The expressions of the flow stress according to several authors are reported in table 1.1. In that table, the variables evolve during deformation, thus they are assigned an evolution rate.

Other kinds of internal variables are also worth being mentioned. Rollet and Kocks [13] use the concept of dislocation debris that are stored as dipoles and loops, and correspond to the dislocations stored in the cell interiors. The Geometrically Necessary Dislocations (GND) introduced by Ashby in [45] were used by Sellars and Zhu [33], Duan and Sheppard [10] and Ma *et al* [46]. Pantleon [47] relates stage IV hardening to the misorientation between subgrains.

Authors	Variables	Flow stress
Kocks [21]	ρ	$\sigma = M\tau_{ath}S(T, \dot{\epsilon})$
Duan* <i>et al</i> [10]	$\rho(\rho_i, \delta)$	$\sigma = \sigma_0 + M\tau_{ath}$
Duan <i>et al</i> [10]	ρ_i, δ	$\sigma = \sigma_0 + M(\tau_{ath} + \tau_\delta)$
Estrin <i>et al</i> [22]	ρ	$\sigma = M\tau_{ath} \left(\frac{\dot{\epsilon}}{\dot{\epsilon}_0}\right)^{1/m^*}$
Estrin <i>et al</i> [43]	ρ_i, ρ_w	$\sigma = M\alpha_1\mu b \left((1 - f_w)\sqrt{\rho_i} + f_w\sqrt{\rho_w}\right) \left(\frac{\dot{\epsilon}}{\dot{\epsilon}_0}\right)^{1/m^*}$
Kabliman <i>et al</i> [25]	ρ	$\sigma = \sigma_0 + M(\tau_{ath} + \tau_{ss} + \tau_d)$
Nes [7]	ρ_i, δ	$\sigma = \sigma_0 + M(\tau_{ath} + \tau_\delta)$
Nes <i>et al</i> [24]	ρ_i, δ	$\sigma = \sigma_0 + M(\tau_{ath} + \tau_\delta + \tau_g + \tau_d)$
Roters <i>et al</i> [9]	ρ_m, ρ_i, ρ_w	$\sigma = M((1 - f_w)\tau_i + f_w\tau_w) + \tau_d$
Roters** [44]	ρ, ρ_m	$\sigma = M(\alpha_1\mu b\sqrt{\rho + \rho_m} + \tau_{eff})$

* In this model, ρ is a function of ρ_i and δ , so the model effectively features 2 variables.

** In that last model, ρ_m is a variable but has no evolution rate. Instead ρ_m is optimized on the run to best match the experimental results.

Table 1.1: Expression of the flow stress according to various authors. The internal variables evolve during deformation, thus they are assigned an evolution rate. τ_{ath} in this table is always given by equation (1.10).

1.3.9 Evolution rates

The general form of the evolution rates consists in combining one or several production term(s) with one or several reduction term(s) (equation (1.19)). The challenge is to find the physical mechanisms behind the evolution of the internal variables and to translate them mathematically. Good examples on that practice are given in [9, 14], among others.

In their 3-internal-variable model (3IVM) for example, Roters *et al* [9] consider the following mechanisms for the evolution rate of ρ_m , ρ_i and ρ_w . First, the mobile dislocations cannot travel a distance longer than their mean free path. Considering equation (1.6) at large enough strains, \bar{l} must be replaced by L and the velocity term in equation (1.7) cancels out:

$$\dot{\gamma} = \dot{\rho}_m^+ bL \quad (1.49)$$

$\dot{\rho}_m^+$ is a production term, hence the + mark. In addition, segments of dislocations can annihilate spontaneously by glide, be stored as dipoles, or be locked, meaning that they cannot glide any more. The formation of jogs for example leaves behind an edge dislocation segment whose Burgers vector is collinear with the dislocation line, thus that segment cannot glide. Each of those mechanisms reduces the density of mobile dislocations and their evolution rate reads:

$$\dot{\rho}_m = \dot{\rho}_m^+ (Orowan) - \dot{\rho}_m^- (glide) - \dot{\rho}_m^- (dipoles) - \dot{\rho}_m^- (lock) \quad (1.50)$$

The dislocation locks are stored in the cell interiors. They can annihilate by climb, and their evolution rate reads:

$$\dot{\rho}_i = \dot{\rho}_m^- (lock) - \dot{\rho}_i^- (climb) \quad (1.51)$$

It is a common assumption that all dipoles eventually end up in the subgrain walls, and they can also annihilate by climb. It proceeds:

$$\dot{\rho}_w = \dot{\rho}_m^- (dipoles) - \dot{\rho}_w^- (climb) \quad (1.52)$$

The detailed expressions of all the terms in the last three equations are derived in [9]. The expression of the evolution rates depends on which mechanisms are considered. In opposition, equation (1.28) does not explore the mechanisms. Rather it settles for dynamic and static phenomena, without entering the details of dislocation interaction.

More recently, Kablman and Sherstnev [25] developed a single variable model for work hardening during hot deformation of Al-Mg-Si alloys. Instead of detailing the mechanisms of dislocation interaction, their approach of the dislocation evolution rate consists in summing a dynamic production term with a dynamic and a static softening term:

$$\frac{\partial \rho}{\partial t} = \dot{\epsilon} \left(\left(\frac{\partial \rho}{\partial t} \right)_{dynamic}^+ - \left(\frac{\partial \rho}{\partial t} \right)_{dynamic}^- \right) - \left(\frac{\partial \rho}{\partial t} \right)_{static}^- \quad (1.53)$$

In equation (1.53), when $\dot{\epsilon} = 0$, only static recovery can occur, which allows the model to deal with static recovery between deformation passes.

Other microstructure based models have been developed. Some values of the dislocation density and subgrain size evolution are given hereafter as basis for comparison. Starting with a well recovered Al-1%Mg, Duan *et al* [10] predict a rapid increase (from 10^{11} to $4 \times 10^{13} \text{ m}^{-2}$) in dislocation density during rolling at 500°C and 2 s^{-1} , followed by a small decrease during static recovery. They also predict a dynamic drop in subgrain size from 9 to 6 – 7 μm . Roters *et al* [9] predict a similar rapid increase for both ρ_i and ρ_w (from 10^{10} to $2 - 9 \times 10^{13} \text{ m}^{-2}$) during deformation of two aluminium-copper alloys at 350°C and 10^{-3} s^{-1} . Nes and Marthinsen [48] predict a stabilization of ρ_i at $2.5 - 8 \times 10^{13} \text{ m}^{-2}$ during deformation at room temperature of two aluminium alloys 1050 and 3207. They also predict a continuous decrease of the subgrain size from 3 to 0.5 μm , for a deformation grade of 2.

In general when a model includes several kinds of dislocations, it is assumed that those are all edge dislocations, with corresponding mechanisms. Prasad *et al.* [49] tried to introduce a screw character, but this evolution was not retained in the later models.

1.4 Recrystallization modelling

At high temperature, whether during or after deformation, two phenomena are known to happen: recovery and, if the deformation grade and the temperature are large enough, recrystallization. Both have been reviewed intensively by Humphreys and Hatherly in [6]. From a modelling point of view, recovery is dealt with by the reduction term in the evolution rates of the internal variables (equation (1.19)). Recrystallization is usually dealt with by a Johnson-Mehl-Avrami-Kolmogorov type model, the content of which is detailed below.

Recrystallization is a two-phase process: first a non classical nucleation of new grains, i.e. without pre-nucleation clusters, and second their growth. The former remains not fully understood because it happens at very short times, making it difficult to observe. Growth however is a pretty straightforward, diffusion driven process.

At this point, it is necessary to introduce the concepts of stored energy of deformation and pressure on a boundary.

1.4.1 The energy of deformation

During cold deformation, the quantity of dislocations increases in the material. Dislocations are line defects that deform the microstructure elastically. As such, they carry an elastic strain field and an elastic energy. The energy per unit length of dislocation line E_{disl} reads [5]:

$$E_{disl} = E_c + E_{el} \quad (1.54)$$

E_c is the energy of the dislocation core itself, which is often neglected. E_{el} is the strain energy arising from the matrix distortion, which depends on the type of dislocation. The elastic field of a mixed dislocation can be seen as the superposition of the fields of its edge and screw components. They yield the line energy:

$$E_{el} = \frac{\mu b^2}{4\pi} \frac{1 - \nu/2}{1 - \nu} \ln \left(\frac{R}{R_0} \right) \quad (1.55)$$

R is the upper cut-off radius of the dislocation, i.e. the outer reach of the strain field, proportional to $\rho^{-0.5}$. R_0 is the inner cut-off radius of the dislocation, within which the dislocation core is located, and usually taken equal to a couple of times b .

Assuming a negligible interaction between the dislocations, the volume energy E_D of the material is given by:

$$E_D = \rho E_{disl} \quad (1.56)$$

Which is often approximated by:

$$E_D = \alpha \mu b^2 \rho \quad \alpha \approx 0.5 \quad (1.57)$$

Sandström and Lagneborg [42] argue that the wall dislocation density being much higher than the cell interior dislocation density, equation (1.57) should rewrite:

$$E_D = \alpha\mu b^2 f_w \rho_w \quad (1.58)$$

It is however more generally accepted that, when the dislocations re-arrange in a cell/subgrain structure, their elastic fields are brought in a configuration of lower energy. The volume energy of the material reads:

$$E_D \approx \frac{1.5\gamma_{sg}}{\delta} \quad (1.59)$$

Where γ_{sg} is the surface energy of the subgrain boundary.

1.4.2 Pressure on a boundary

Let us consider a grain or a subgrain boundary separating two crystals or two regions of a crystal. If the latter have not been subjected to the same deformation, their respective volume energies differ from an amount ΔE_D . In order to minimize ΔE_D , the lowly strained crystal must grow into the highly strained crystal. This gives rise to an effective pressure on the boundary P_D :

$$P_D = \Delta E_D \quad (1.60)$$

P_D is called the driving pressure for recrystallization. It is involved in both the nucleation and the growth processes.

Because the grains have boundaries, and those boundaries have a surface energy, they are subject to capillarity effects, which translate into a capillarity pressure P_C :

$$P_C = \frac{3\gamma_g}{D} \quad (1.61)$$

Where γ_g is the surface energy of the grain boundaries and D the grain diameter. During nucleation, the capillarity pressure tends to shrink the newly formed nuclei and opposes the driving pressure for recrystallization. Once the nuclei have reached a critical size, capillarity assists their growth and P_C adds to P_D .

When the microstructure is populated with second-phase particles, those particles have a retarding effect on the moving grain boundaries. That phenomenon is the so-called Zener pinning. For a homogeneous distribution of spherical particles with a volume fraction F_V and uniform radii R_p , the number of particles per unit volume N_V reads [6]:

$$N_V = \frac{3F_V}{4\pi R_p^3} \quad (1.62)$$

The number of particles intersecting a unit area of the boundary N_S reads:

$$N_S = 2R_p N_V = \frac{3F_V}{2\pi R_p^2} \quad (1.63)$$

The Zener pressure opposing the driving pressure is defined as:

$$P_Z = \frac{3F_V \gamma_g}{2R_p} \quad (1.64)$$

The total pressure on a grain boundary resulting from the stored dislocations, the capillarity and the Zener pinning, reads:

$$P = P_D \pm P_C - P_Z \quad (1.65)$$

The Zener pinning arises from boundaries moving in the field of second-phase particles. Thus, it applies only to moving boundaries; the grains do not shrink because of it when the driving pressure is less than P_Z , but recrystallization / grain growth ceases.

1.4.3 Nucleation

When dealing with static recrystallization after cold deformation, two processes are usually held responsible for the nucleation of new grains. First, second-phase non-shearable particles leave a zone of high deformation in their wake. The larger the particles, the larger the deformation zone and the deformation gradient. New grains of random orientation can nucleate from this highly deformed zone. This process is named Particle Stimulated Nucleation (PSN). The second process, called Strain Induced Boundary Migration (SIBM), was introduced by Bailey in [50, 51]

and will be detailed more thoroughly here. In aluminium alloys, it is generally recognized that SIBM is the dominant nucleation mechanism.

During deformation, the grains do not undergo the same amount of slip because of their different orientations, thus they do not all store the same quantity of energy. Let us consider a fraction of a boundary separating two grains of different stored energies. If the pressure on the boundary is large enough, the latter can bulge into the grain of higher energy, leaving a crystal free of dislocations in its wake, hence a recrystallized grain. Bulging is a diffusion driven process. Atoms from the highly deformed grain have to jump into the new grain through the boundary. Burke and Turnbull calculated the jump frequency of an atom through a boundary in [52] using the absolute reaction rate theory. Bailey used it in [50] to define the critical radius R_b that a semi-spherical bulge must have in order to start growing:

$$R_b > \frac{2\gamma_g}{P} \quad (1.66)$$

Note that Bailey wrote ΔE_D instead of P , because he worked with pure metals and neglected to consider the Zener opposing pressure.

1.4.4 Grain growth

When stable, the nuclei start growing. The rate of growth \dot{R}_g is related to the driving pressure on the boundary through the mobility of the boundary M_b :

$$\dot{R}_g = M_b P \quad (1.67)$$

Where M_b is assumed to have an Arrhenius form.

At the beginning of recrystallization, the microstructure consists entirely of highly energetic deformed material. After an incubation time, $R_g > R_c$ the nuclei grow rapidly. Recrystallization stops either when the microstructure is fully recrystallized, or when the deformed material becomes highly recovered, i.e. $P = 0$. When recrystallization is complete, only the capillarity effects remain to promote grain growth. P_C being usually much lower than P_D , grain growth following recrystallization, if it happens, extends on a much longer time scale.

1.4.5 Recrystallized fraction

The original theory of Avrami [53, 54] has been extensively reviewed, used and modified. We will only report it in its most general form here, taken from [6, 55]. Let us assume a uniform nucleation rate \dot{N} per unit volume. Assuming that all the nuclei grow unhindered by each other, meaning that they can overlap each other, the extended volume of recrystallized material V_{ext} at time t reads:

$$V_{ext}(t) = \int_0^t \dot{N}(t') V(t, t') dt' \quad (1.68)$$

Note that V_{ext} is a dimensionless quantity. $V(t, t')$ is the volume at time t of a grain nucleated at time t' :

$$V(t, t') = f \left(\int_{t'}^t \dot{R}_g(z) dz \right)^a \quad (1.69)$$

f is a shape factor, equal to $4\pi/3$ for equiaxed grains. a is the Avrami exponent, whose value depends on the growth dimension. $a = 3$ for three dimensional growth.

The evolution of the fraction of recrystallized material χ_{RX} is then given by:

$$\chi_{RX} = 1 - \exp(-V_{ext}) \quad (1.70)$$

Ideally, the recrystallization model is built in such a way that it makes use of the microscopic variables defined in the flow stress model to calculate the stored energy of deformation. Vatne *et al.* [56] use this approach for deformation at high temperature and subsequent static recrystallization, with the stored dislocation density as single internal variable. Their model predicts a decrease of the recrystallized grain size with the stored energy of deformation and is able to keep track of the fraction of cube textured grains fed as an input.

1.5 Problem formulation

In the course of his Ph.D. thesis [25, 57], P. Sherstnev developed a model dealing with physically based constitutive modelling at high temperatures in an aluminium alloy 6082 provided by the company AMAG, Austria Metal¹. His model was

¹<https://www.amag.at>

designed to predict the flow behaviour above 400 °C, where a steady-state is rapidly reached, based on the evolution of the total dislocation density as single internal variable. One strong point of his model was the introduction of static recovery between passes in addition to dynamic recovery during deformation. Below 400 °C however, the persistent strain hardening cannot be captured by the model. The model also lacked the ability to predict the yield stress of the material as a function of temperature and strain rate. The output of the constitutive model was then used as input in a semi-empirical model for static recrystallization, in order to cover phases II and III in figure 1. The flow and recrystallization models represented a whole package for simulating multipass hot rolling with static recrystallization happening between passes and during subsequent cooling.

In order to cover a wider range of their production process and better understand the microscopic features involved, the model of Sherstnev was extended to lower deformation temperatures, and the recrystallisation model was reviewed accordingly. The resulting model is aimed to be used in a multipass rolling process where hot and cold rolling as well as heat treatments are involved, using only one physical model.

In view of the literature reviewed above, it seems that the approach proposed by Sherstnev can be extended to lower temperatures by adding extra variables into the model. The use of ρ_i and ρ_w (section 1.3.8) based on the structure of cell forming alloys showed great results and shall be further expanded here. The evolution rates however shall remain simple enough in order to ease their integration in a finite element engine. In order to account for the deformation, it also seems reasonable to make use of the mobile dislocation density ρ_m . However, because the kinetics of ρ_m are much slower than that of industrial deformation, it is the author's opinion that ρ_m should remain constant during deformation, as supported by equation (1.8).

Regarding the constitutive equation, the use of an effective stress (section 1.3.6), in addition to capturing the effects of the conditions of deformation on the work hardening, links those effects to microscopic features and therefore shall be retained. It will be showed in chapter 6 that relating τ_{eff} to the overtaking of local obstacles by cross-slip cannot account for all deformation temperatures. A new hybrid approach combining the formation of jogs and cross-slip is developed, that offers a better comprehension of the microscopic mechanisms involved in deformation at low temperature, and allows for a better grasp of the dependency of the yield stress on the deformation conditions.

The most critical point when modelling recrystallization is perhaps the nucleation of new grains. The number of nuclei is quite often an empirical parameter that has to be optimized. It usually does not take into account the amount of strain in the

material, or static recovery. The latter not only slows down the kinetics of grain growth, it also prevents the nucleation of new grains. Thus, a proper nucleation criterion needed to be worked out, that: i. relates to the microscopic variables used in the constitutive model, ii. takes into account the deformation grade of the material, and iii. grasps the competition between recovery and recrystallization.

Following those considerations, the main goals of this thesis are:

- develop a physically based constitutive model applicable to cold, intermediate and hot working over a wide range of strain rates
- develop a model for static recrystallization with a tailored nucleation criterion that takes into account the three constraints mentioned above
- implement the models in a finite element macroscopic code

Throughout this document, the reader will often encounter the triplet (**RD**, **ND**, **TD**). It is designed to serve as spatial reference frame when dealing with rolled products. **RD** stands for “Rolling Direction”, **ND** for “Normal Direction” and **TD** for “Transverse Direction”. The three directions are orthogonal to each other and are defined as shown in figure 1.4. This convention will be used in the remainder of this document.

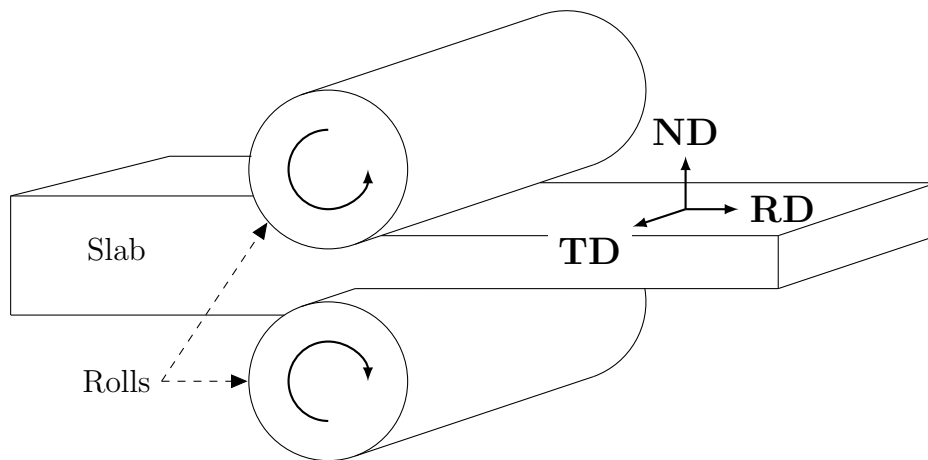


Figure 1.4: Definition of the reference frame triplet (**RD**, **ND**, **TD**).

Chapter 2

Materials Characterization

Physically based models cannot be developed without adequate material characterization, whether it is to research a path for modelling, to initialize some of the parameters, or to validate the output. Plates from a commercial aluminium alloy 6082, whose chemical composition is given in table 2.1, were delivered by the company AMAG Austria Metall in the following conditions.

1. HR1: hot rolled between 550 °C and 450 °C to a thickness of 4.9 mm and slowly cooled down to room temperature.
2. HR2: hot rolled between 550 °C and 450 °C to a thickness of 3.9 mm and slowly cooled down to room temperature.

The 3.9 mm thick hot rolled state was the initial state for this study. It was investigated by means of Light Optical Microscopy and Scanning Electron Microscopy combined with image analysis. Samples in this state were then deformed in plane-strain condition at various strain rates and temperatures. Cold deformed samples were additionally oven annealed to induce recrystallization and observed with Scanning Electron Microscopy. The 4.9 mm thick hot rolled state was only used to assess the effect of the plate thickness on the flow stress of the material during cold forming. It appeared that the flow curves at room temperature of materials 1 and 2 superimposed perfectly for all investigated strain rates. The cold rolled state was used in a parallel experimental study of the grain size after annealing [58] and to assess the subgrain size after industrial deformation.

Si	Fe	Cu	Mn	Mg	Cr	Ni	Zn	Ti	Al
0.88	0.39	0.07	0.43	0.81	0.02	0.01	0.04	0.04	Compl.

Table 2.1: Chemical composition of the studied AA6082 alloy, in weight percent.

2.1 Methodology

2.1.1 Plain strain tests

Plane strain compression tests are known to exhibit the same mechanical characteristics as the rolling process of flat products. The stress-strain curves of the material under two-dimensional sollicitation were obtained by conducting plane-strain compression tests in a Gleeble[®] 3800 System. The tests were conducted on the hot rolled material of thickness 3.9 mm (HR2). The test configuration is illustrated in figure 2.1. The sample size is 10 mm in the rolling direction by 20 mm in the transverse direction, and the contact length between the anvils and the sample is 5 mm. A nickel based suspension was used as lubricant to reduce the friction between the anvils and the samples. In the Gleeble[®] 3800, heating is done by resistance heating. An electrical current is brought directly by the anvils and flows through the sample. In those experiments, a J-type (iron-constantan) thermocouple was welded as illustrated in figure 2.1 for temperature control. Care was taken to weld the thermocouple horizontally on an isothermal plane. The two branches of the thermocouple were welded as close as possible to prevent them from spreading out of between the anvils during deformation.

The samples were heated up to the deformation temperature by resistance heating at a rate of $5\text{ }^\circ\text{C s}^{-1}$ and soaked 10 to 15 s for temperature stabilization. The samples were then deformed to a macroscopic true strain of 1 and air cooled to room temperature (figure 2.2). During heating and soaking, the upper anvil was let free to move in order to account for the thermal expansion of the whole system – machine and sample. The testing conditions are reported in table 2.2.

The true strain $\bar{\epsilon}$ and the true flow stress of the material σ are given by equations (2.1) and (2.2), respectively [59]:

$$\bar{\epsilon} = \frac{2}{\sqrt{3}} \ln \left(\frac{h_0^s}{h_0^s - \Delta h} \right) \quad (2.1)$$

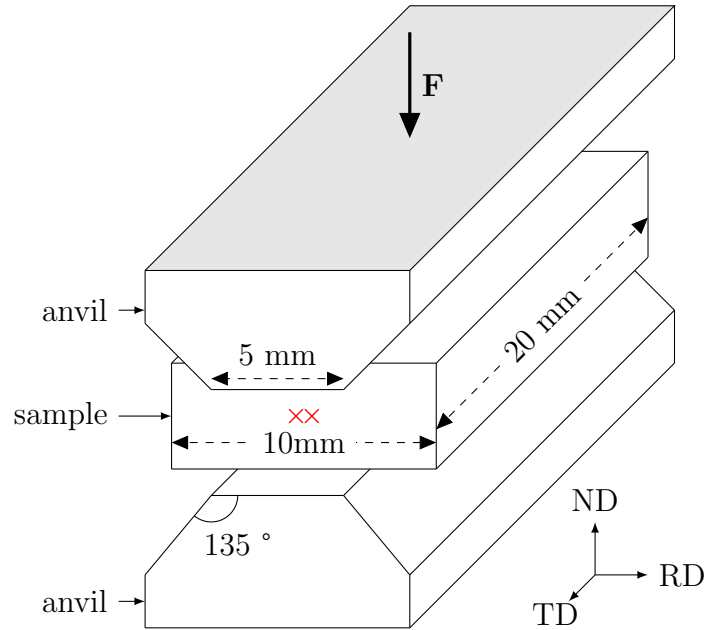


Figure 2.1: Geometry of the plane-strain compression test. The deformation force \mathbf{F} is applied on the shaded surface. The thermocouple welding position is marked by the red crosses (xx).

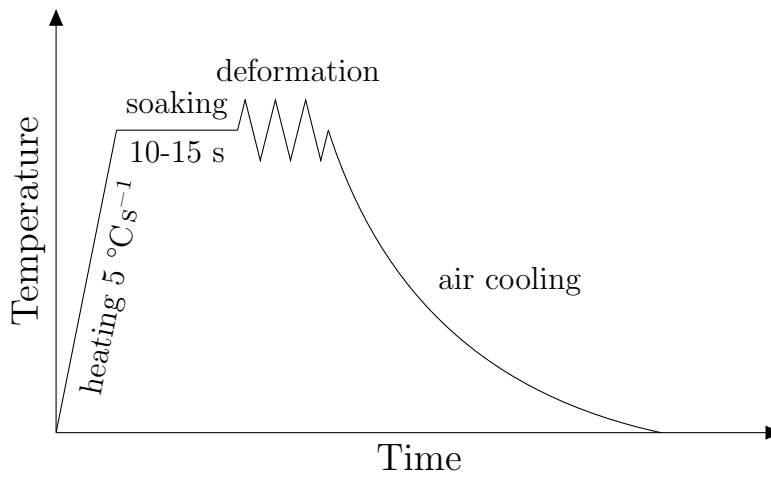


Figure 2.2: Thermomechanical schedule of the plane-strain compression tests.

Strain rate (s ⁻¹)	Temperature (°C)								
	25	50	100	150	200	250	300	350	400
0.01	✓	✓	✓	✓	✓	✓	✓	✓	✓
0.1	✓	✓	✓	✓	✓	✓	✓	✓	✓
1	✓	✓	✓	✓	✓	✓	✓	✓	✓
10	✓	✓	✓	✓			✓	✓	✓

Table 2.2: Grid of plane-strain experiments.

$$\sigma = \frac{\sqrt{3}}{2} \frac{|F_{app}|}{A} \quad (2.2)$$

Where h_0^s is the initial thickness of the sample, Δh the thickness reduction, F_{app} the applied force and A the contact area.

Two to three tests were carried out per deformation conditions. The obtained flow curves were smoothed, sampled with a strain period of 10^{-3} and averaged over the 3 samples. The linear elastic part was manually removed as it also includes the elastic deformation of the anvils. The results of the tests are given in chapter 3, where they are compared with the results of the flow stress model. Figure 2.3 shows the raw flow curves of two samples deformed at 100 °C and 0.01 s^{-1} superimposed with the treated data.

2.1.2 Sample preparation for microscopy

Before any microscopic observation, the samples were cold embedded with a Varidur 3000/3003 cold mounting compound from Buehler, mechanically ground with sandpaper grading from 180 to 4000 for 1 to 2 min per paper, polished with a suspension of DP-Paste P 3 μm diamond particles from Struers for 1 to 2 min and further polished with a NonDry colloidal silicon suspension (OP-S) from Struers for 1 to 5 min. The samples were rinsed with water between each step. In the latter step, the samples and polishing cloth were rinsed with water every minute to avoid crystallization of the suspension. Directly after polishing, the remaining impurities at the surface of the sample were removed with acoustic waves in an ethanol bath. A subsequent step of electrochemical etching with a Barker's reagent was made to identify the grain structure in section 2.1.5.

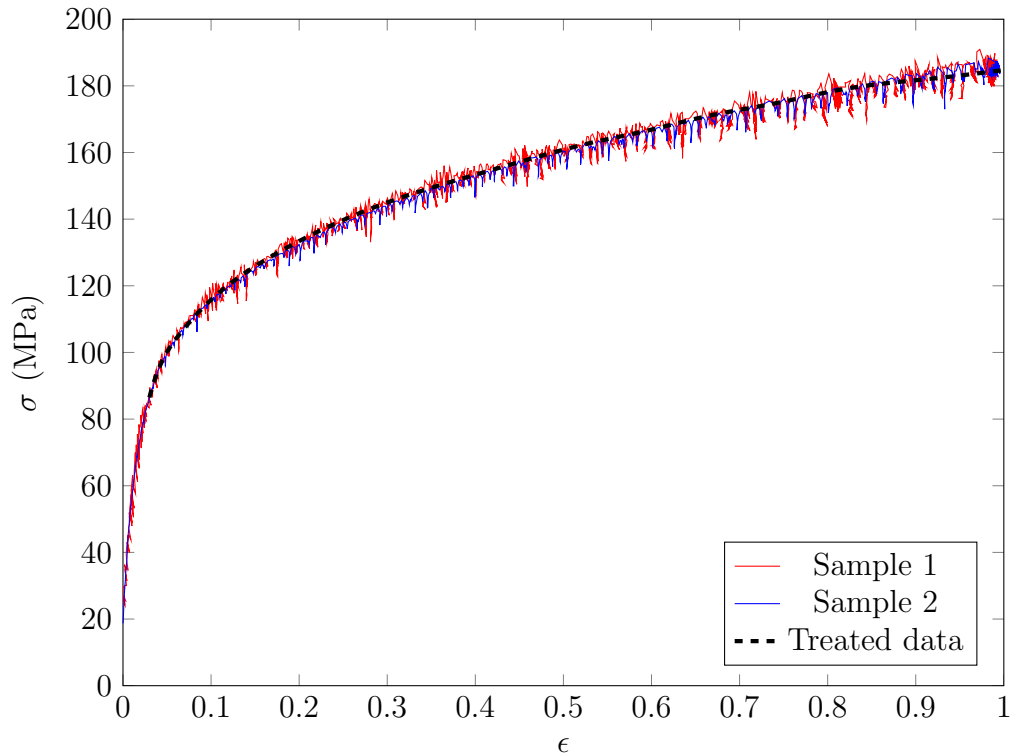


Figure 2.3: Deformation at $100\text{ }^{\circ}\text{C}$ and 0.01 s^{-1} . Superimposed raw and treated data. The elastic part was removed manually.

2.1.3 Microscopic equipment

All microscopic investigations were carried out by means of Light Optical Microscopy and Scanning Electron Microscopy with the following devices:

1. Light Optical Microscope Zeiss Axio Observer.71m in bright field mode or in polarized light mode (after Barker's etching).
2. Scanning Electron Microscope Zeiss Ultra 55 at the Austrian Center for Electron Microscopy and Nanoanalysis FELMI-ZFE in Back Scattered Electron (BSE) mode (section 2.1.4) and Electron Back Scattered Diffraction (EBSD) mode (section 2.1.5).

2.1.4 Observation of second-phase particles

The first step of characterization of the second-phase particles was to determine their type, their size and their spatial distribution. This was done by means of

light optical microscopy in bright field mode and by scanning electron microscopy in backscattered electron mode, based on the chemical contrast of the particles.

The pictures were analyzed with the software ImageJ [60, 61]. They were first turned into 8-bit grayscale images. After adjusting the levels of brightness and contrast, the particles of interest were selected with an appropriate threshold. Particles intersecting the edges of the picture were removed from the mask of the threshold, as well as all the particle whose area was smaller than a critical value A_c . A_c had to be determined according to the type of particle being analyzed.

The density of particles N_S intersecting the sample surface was calculated using:

$$N_S = \frac{N_P}{h_p l_p} \quad (2.3)$$

Where N is the number of particles intersecting the sample surface and h_p and l_p are the respective picture height and length.

The particle radius was determined as follows. Let (Oz) be the normal direction to the observation plane. The average area $\langle A_I \rangle$ of the circle created by the random intersection of a sphere of radius R_s with a plane perpendicular to (Oz) can be calculated by averaging the area of intersection over $[-R_s; R_s]$:

$$\langle A_I \rangle = \frac{1}{2R_s} \int_{-R_s}^{R_s} \pi (R_s^2 - z^2) dz = \frac{2\pi}{3} R_s^2 \quad (2.4)$$

Where z is the position of the intersecting plane along (Oz) . Assuming that the particles of interest are randomly distributed spheres of radius R_P , then all particles whose centre is located within a distance R_P under the sample surface and all those whose centre was located within a distance R_P above the sample surface are visible in the picture. If N_S is large enough, R_P is determined by replacing $\langle A_I \rangle$ by the average measured particle area $\langle A_P \rangle$ and R_s by R_P in equation (2.4):

$$\langle A_P \rangle = \frac{2\pi}{3} R_P^2 \quad (2.5)$$

Equation (2.5) can be corrected to take into account the removal of undercritical particles by averaging the area of intersection over $[-R_c; R_c]$, where $R_c = \sqrt{A_c/\pi}$:

$$\langle A_P \rangle = \frac{1}{2R_c} \int_{-R_c}^{R_c} \pi (R_P^2 - z^2) dz \quad (2.6)$$

Which yields:

$$\langle A_P \rangle = \pi \left(R_P^2 - \frac{R_c^2}{3} \right) \quad (2.7)$$

The particle volume fraction is then given by combining equations (1.63) and (2.5):

$$F_V = N_S \langle A_P \rangle \quad (2.8)$$

Or by combining equations (1.63) and (2.7), without the undercritical particles:

$$F_V = \frac{2}{3} N_S \pi \left(\frac{\langle A_P \rangle}{\pi} + \frac{R_c^2}{3} \right) \quad (2.9)$$

2.1.5 Annealing tests

Cold plane-strain deformed samples were oven annealed at 300 °C and 400 °C for 10 s, 1 min, 5 min, 20 min and 1 h to induce recrystallization. The samples were placed cold in the hot furnace and water quenched after annealing. Three consecutive EBSD mappings from the middle of the sample to the centre of a deformation cross were made on each sample, except for the sample recrystallized at 400 °C for 10 s, where only the middle of the sample was mapped.

The light optical micrograph in polarized light mode in figure 2.4 shows the deformation zone of a sample deformed in plane-strain condition at room temperature, in the (ND, RD) plane. The microstructure displays two deformation crosses, hence a heterogeneous distribution of strain. A finite element analysis of the plane-strain test was made with the software DEFORM2D™ [62] (see chapter 5). It reveals that the true strain is equal to the macroscopic strain of 1 in the middle of the sample, in between the deformation crosses. In the centre of the crosses, a true strain of 1.5 is achieved.

In a simultaneous study, P. Loidolt [63] carried out annealing tests of cold plane-strain deformed samples from the material HR2.

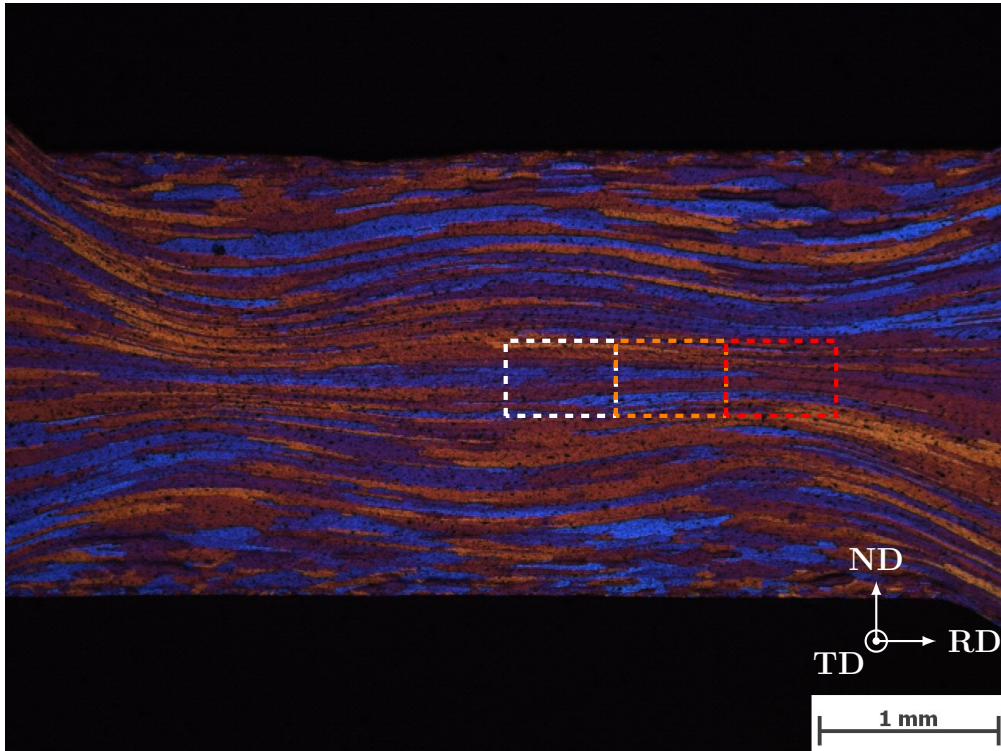


Figure 2.4: Light Optical Micrograph of a cold sample deformed in plane-strain condition, magnified 15x. The consecutive zones studied in EBSD are dashed. The true strain increases from 1 (white) to 1.5 (red)

2.1.6 Grain and subgrain characterization

The recrystallization kinetics were studied with the software OIMTM Data Analysis 7 [64]. The three maps were first merged together using the merging function of OIMTM. The data was cleaned up with a iterating grain dilation, using a grain tolerance angle of 10° and a minimum grain size of 20 pixels, i.e. $\approx 17 \mu\text{m}^2$. The grain tolerance angle determines the angle of misorientation above which two neighbouring data points belong to different grains. It was set to 10 degrees. The grain orientation spread is the spread of orientations of all the data points within a grain with respect to the average orientation of the grain. Grains whose orientation spread was lower than 3 degrees were considered as recrystallized.

The experimental results are shown in chapter 3, where they are used to validate the recrystallization model.

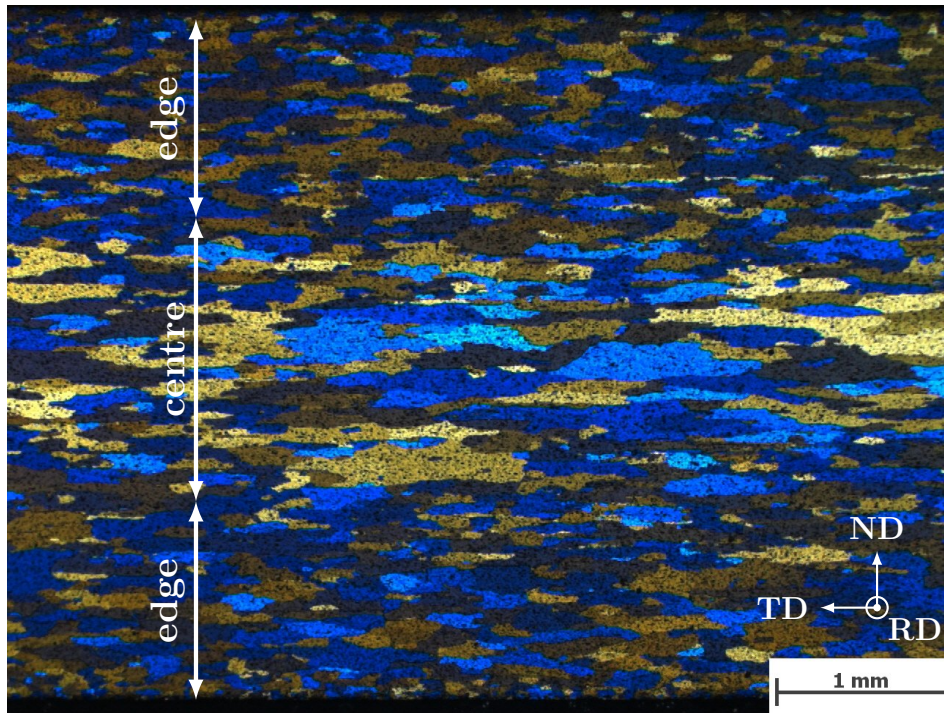


Figure 2.5: LOM micrograph of the hot rolled plate perpendicular to the transverse direction.

2.2 As received condition characteristics

The grain size in the 3.9 mm thick hot rolled material (HR2) was investigated in a prior study by P. Loidolt [58]. Figure 2.5 shows a light optical micrograph in polarized light mode of the plate in the normal direction. The grain dimensions clearly appear bigger in the centre of the plate than on the edges. The grains were assumed to be ellipsoids — they are disks in 3D, appear as ellipses in 2D. Their length l_0 , width w and height h_0 was defined as shown in figure 2.6. They were measured by a mean linear interception method and the measurements are reported in table 2.3. As the variation in grain width is assumed to be negligible in further cold deformation, w is not attributed an index. No stereological corrections were made.

The precipitation state was investigated in the 3.9 mm thick hot rolled material. The light optical micrographs in bright field mode (figures 2.7 and 2.8) show second phase particles of various sizes. The biggest particles appear to be aligned in the rolling direction and display rather complex “Chinese” morphologies, while the smallest ones appear blocky and disperse.

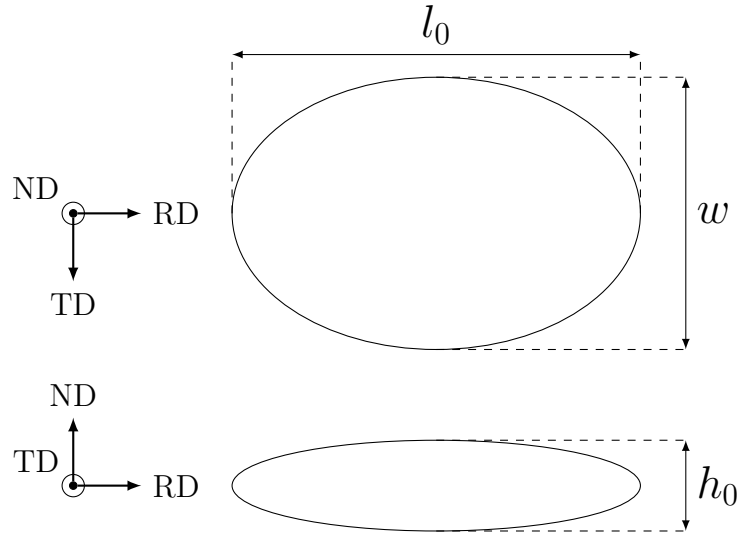


Figure 2.6: Grain geometry. The view is given by the reference frame.

	Central region	Edges
l_0 (μm)	680	200
w (μm)	430	190
h_0 (μm)	85	70
h_0/l_0	0.125	0.350
h_0/w	0.198	0.368

Table 2.3: Grain size measured by mean linear interception in light optical micrographs [58].

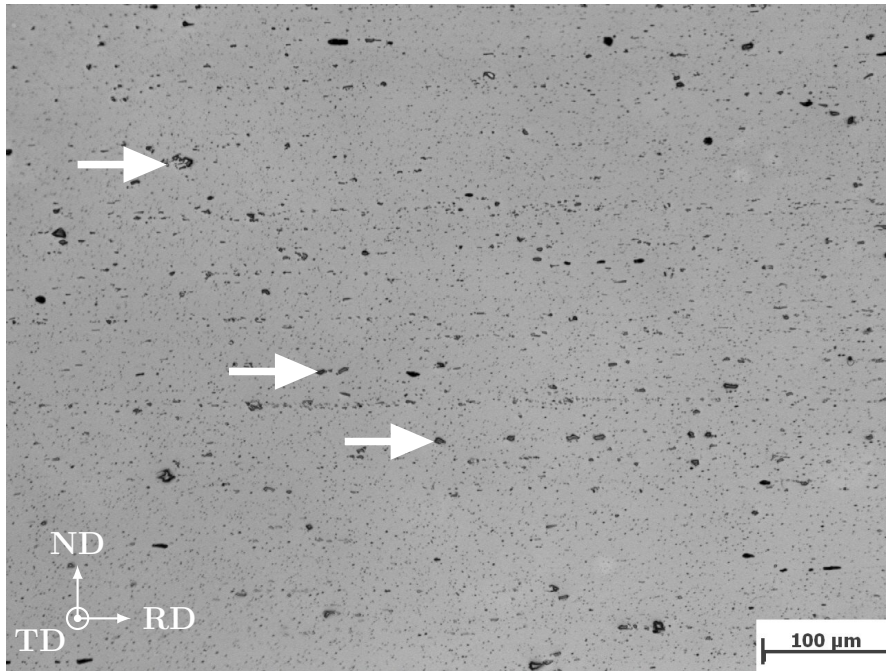


Figure 2.7: LOM micrograph of the hot rolled plate. The arrows indicate large Al-FeMnSi particles aligned in the rolling direction.

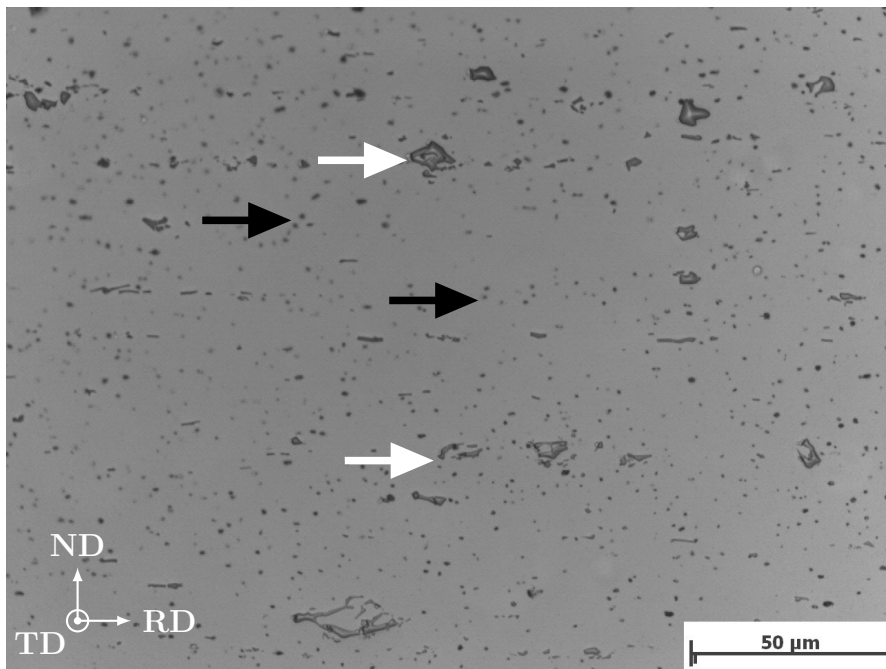


Figure 2.8: LOM micrograph of the hot rolled plate. The white arrows indicate large Al-FeMnSi particles and the black arrows blocky Mg₂Si.

The backscattered electron mode in scanning electron microscopy gives pictures with a chemical contrast (figures 2.9 to 2.12). The background contrast in those micrographs comes from the sample preparation, where long OP-S polishing times have an etching effect. Three kinds of particles could be clearly identified with the help of EDX analysis: large white FeMnSi aluminides with “Chinese” morphologies, blocky black Mg₂Si of intermediate size and small, finely disperse FeMnSi aluminides with spheroidal morphologies. The average surface density, radius and volume fraction of each type of particle is given in table 2.4.

Particle type	N_S [μm^{-2}]	R_P [μm]	F_V [%]	$\sqrt{F_V}/R_P$ [μm^{-1}]
Large Al-FeMnSi	0.0015	2.5	1.7	0.52
Mg ₂ Si	0.039	0.35	1.0	2.9
Small Al-FeMnSi	1.1	0.06	0.83	15

Table 2.4: Measured particle characteristics in the 3.9 millim thick hot rolled material (HR2). The ratios $\sqrt{F_V}/R_P$ are indicated because they play a role in dislocation pinning and will be used in equation (3.4).

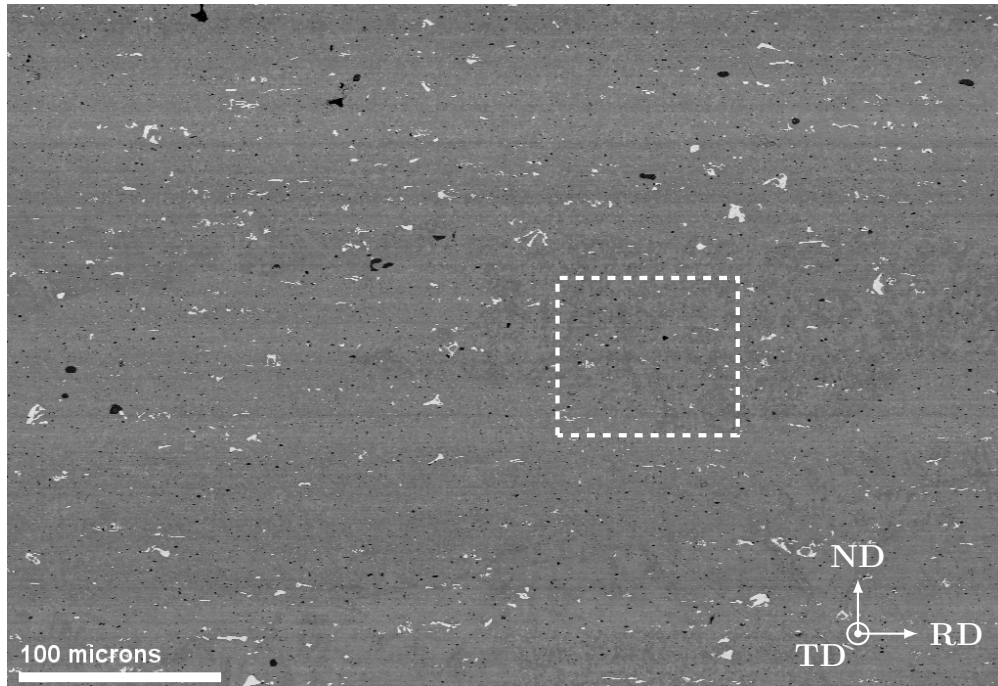


Figure 2.9: SEM Micrograph of the 3.9 millim thick hot rolled material.

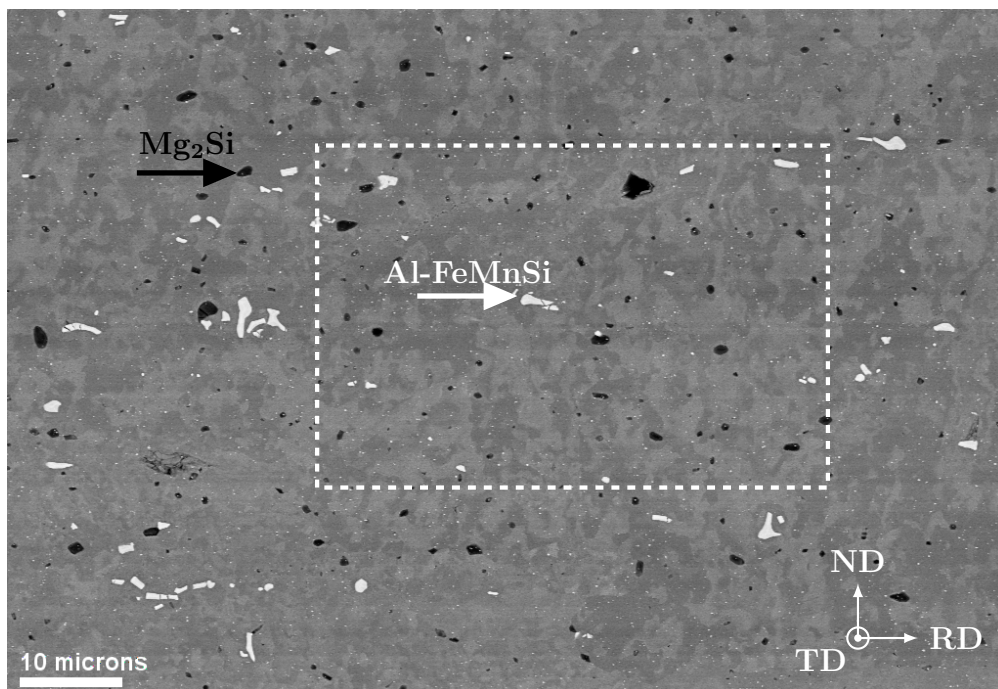


Figure 2.10: Magnification in figure 2.9.

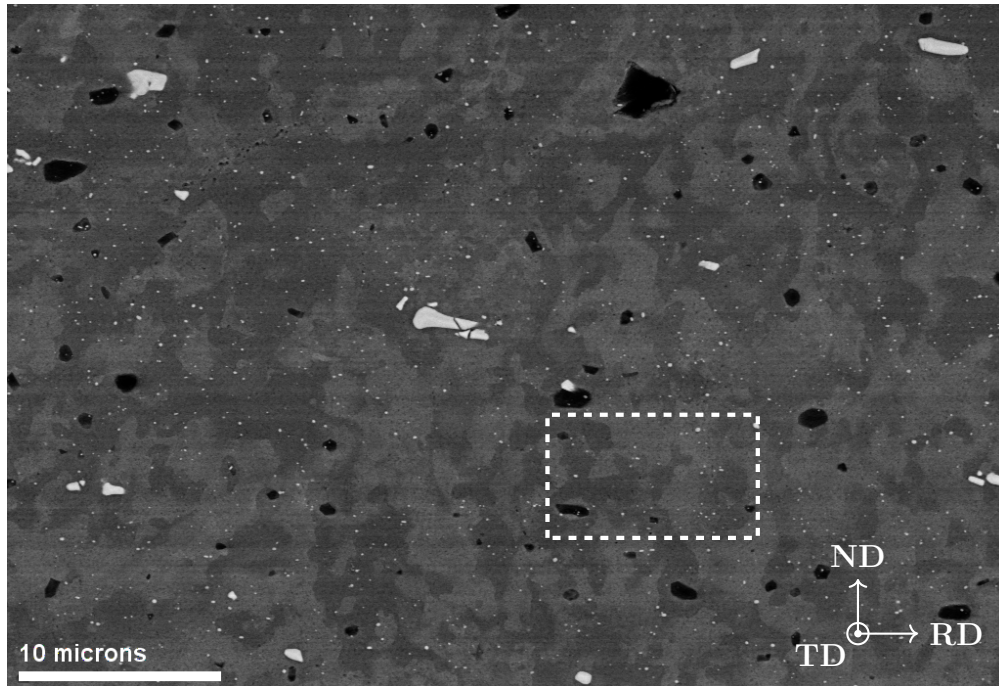


Figure 2.11: Magnification in figure 2.10.

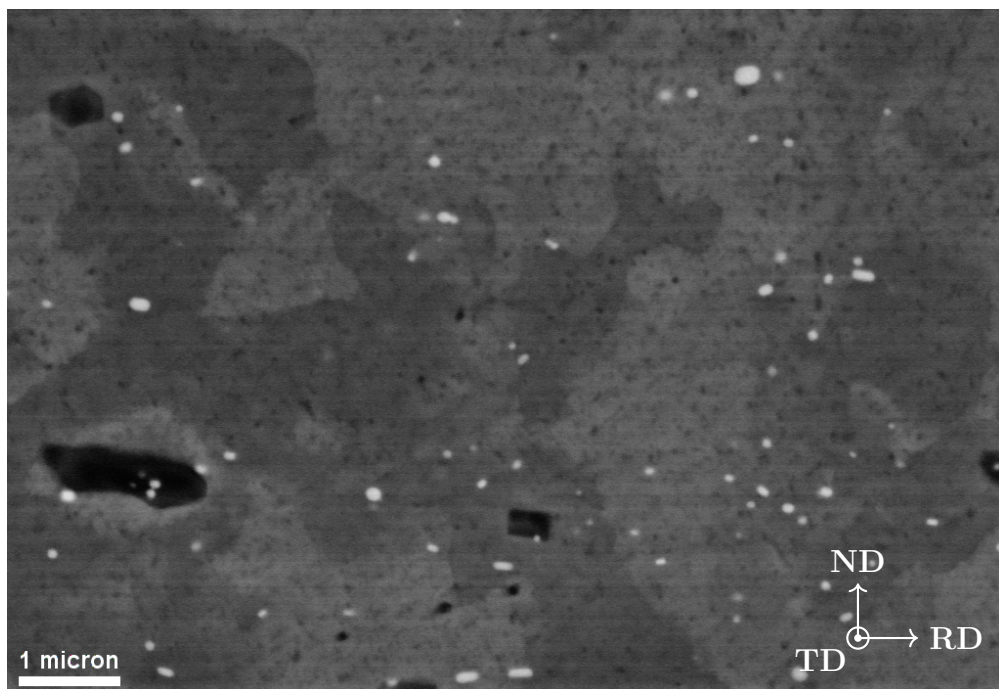


Figure 2.12: Magnification in figure 2.11.

Chapter 3

Flow stress model

At high temperatures, the flow stress saturation can be easily modelled on the basis of one internal variable, like the total dislocation density or the subgrain size, that saturates after some strain. At moderate and low temperatures however, modelling the work hardening requires at least two internal variables with their own evolution kinetics. Especially, the successive stages III and IV of hardening are respectively linked to the rapid storage of dislocations and their rearrangement in subgrain boundaries.

A model featuring three kinds of dislocation densities was developed. One of them appears as a strain rate dependent parameter, while the two others vary with strain and strain rate. The flow stress is determined from the contributions of long range elastic interactions and short range physical interaction between dislocations, as well as their interaction with second-phase particles.

A model structure as defined in section 1.3 was adopted.

3.1 Model set up

3.1.1 Microstructure representation

The microstructure is assumed to be composed of well defined subgrains, whose walls and interiors are populated with dislocations of respective densities ρ_w and ρ_i . We emphasize that, although ρ_w classically stands for the dislocation density *within* the subgrain walls, it here represents the total length of wall dislocations per unit volume *of material*. The later definition yields lower densities than the

former. Additionally, mobile dislocations of density ρ_m are present to account for the plastic deformation. Mobile dislocation loops can extend across several subgrains before being stored and transformed into interior dislocations that do not move, and contribute to ρ_i . The wall dislocations are created by rearrangement of the interior dislocations in a configuration of lower energy. The density of stored dislocations ρ reads:

$$\rho = \rho_i + \rho_w \quad (3.1)$$

And the total dislocation density reads:

$$\rho_t = \rho + \rho_m = \rho_i + \rho_w + \rho_m \quad (3.2)$$

Figure 3.1 shows the microstructure representation described above. Some simplifications were done in figure 3.1 to gain clarity:

- Only edge dislocations are represented here. This is correct for the subgrain walls, but there are also screw dislocations in the subgrain interiors.
- All dislocations have the same orientation. In reality, there are roughly as many dislocations of opposite orientation.
- Dislocations actually glide on different slip systems, which is not visible here.

Note that the dislocations are ordered and densely packed within the subgrain walls, but disordered and less densely packed in the subgrain interiors.

The subgrain wall and subgrain interior dislocations are immobile and act as pinning agents for any mobile dislocation on its way through the crystal. As such, they contribute to work hardening. The mobile dislocations offer in comparison a weak resistance to the imposed stress as they are free to glide. Their contribution to the work hardening is negligible.

3.1.2 Constitutive equation

The constitutive equation links the dislocation densities to the flow stress of the material. Because the latter is polycrystalline, the flow stress σ relates to the resolved shear stress τ through the Taylor factor M (equation (1.3)).

The shear stress results from multiple contributions. Here, only three of them are considered, namely the athermal stress τ_{ath} (equations (1.10), (1.11) and (3.1)),

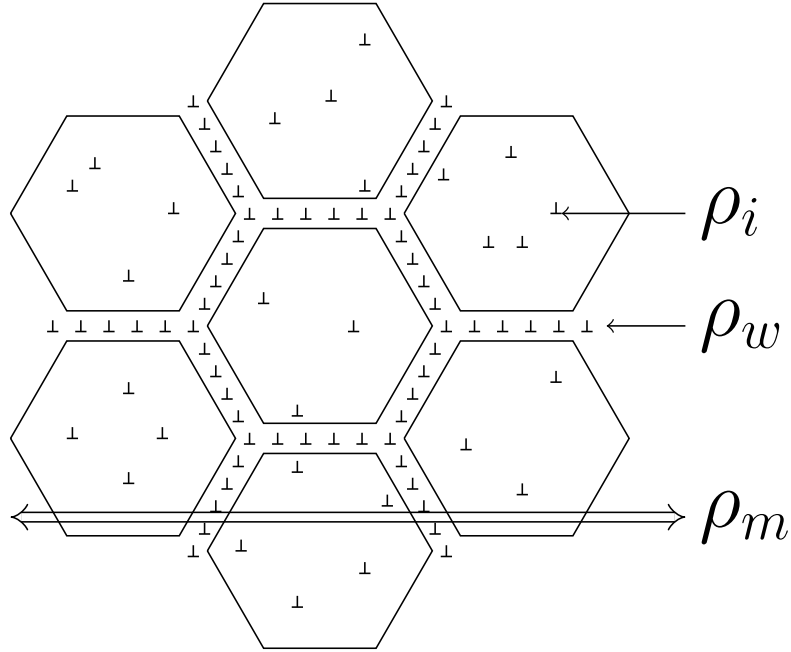


Figure 3.1: Representation of the microstructure. The subgrain wall dislocations have a density ρ_w , the subgrain interior dislocations a density ρ_i . The mobile dislocations can travel through several subgrains before being stored. They have a density ρ_m .

the contribution from second-phase particles (equation (1.21)) τ_d and the effective stress τ_{eff} (equation (1.37)).

$$\tau = \tau_{ath} + \tau_{eff} + \tau_d \quad (3.3)$$

The linear summation is generally accepted. For a discussion on the superposition of the contributions to the shear stress, see [65].

As mentioned in section 1.3.8, the school of Gottstein encourages to decompose the contributions from the cell walls and the cell interiors into a hybrid model (equation (1.48)). Rollett and Kocks [13] however argue that the flow stress is determined by the percolation of the mobile dislocations past the forest dislocations and the “hard spots”, i.e. the local fluctuations in dislocation density due to the presence of cell/subgrain walls. Because of that, the flow stress within the hard spots does not affect the measured flow stress. Therefore, the approach of Gottstein and co-workers is not retained here.

Combining equations (1.3), (1.10), (1.11), (1.21), (1.23), (1.37), (2.8), (3.1) and (3.3)

and assuming that forest dislocations, separated by a distance $\rho^{-0.5}$, are the major obstacles to mobile dislocation motion, it comes:

$$\sigma = M \left(\alpha_1 \mu b \sqrt{\rho_i + \rho_w} + \frac{Q_{act}}{V_{act}} + \frac{k_B T}{V_{act}} \ln \left(\frac{M \dot{\epsilon}}{\rho_m b \nu_d} \sqrt{\rho_i + \rho_w} \right) + \frac{\mu b \sqrt{F_V}}{\chi'' R_p} \right) \quad (3.4)$$

Where χ'' is a constant of the order of $\sqrt{2}$. Note that when several kinds of second-phase particles coexist in the microstructure, their individual contributions have to be added in equation (3.4). In our case, we are dealing with an overaged material, where the typical Mg_2Si hardening precipitates are too large to have an effect on the strengthening. However, the finely disperse FeMnSi aluminides with a ratio $\sqrt{F_V}/R_p$ much greater than the other kinds of precipitate are believed to contribute to τ_d . Those small Al-FeMnSi are present in the initial state, and do not dissolve during deformation at high temperature. Their contribution is considered constant in equation (3.4).

3.1.3 Evolution rates

During thermomechanical processes, the quantity of microstructural defects varies; this phenomenon is at least partially responsible for the hardening or the softening of the material.

The Orowan equation in its differential form (equation (1.8)), used to establish the constitutive equation (3.4), implies per se that the mobile dislocation density remains constant during deformation, at given conditions of strain rate and temperature. To our knowledge, all the models featuring the mobile dislocation density as internal variable have an evolution rate for it, with a production term and an annihilation term as in equation (1.19). Although it is true that mobile dislocations are emitted, for example by Frank and Read sources, and stored or annihilated, the Orowan equation indicates that there is a balance between the production and the reduction of the mobile dislocation density for a constant strain rate. It may still very well be a function of the processing conditions, i.e. the deformation rate and the temperature.

ρ_i and ρ_w however must evolve during plastic deformation and subsequent recovery. Their evolution rate is split into a dynamic (D) and a static (S) part:

$$\frac{\partial \rho_x}{\partial t} = \left(\frac{\partial \rho_x}{\partial t} \right)_D + \left(\frac{\partial \rho_x}{\partial t} \right)_S \quad (x = i, w) \quad (3.5)$$

The static/dynamic splitting allows for work hardening as well as for recovery after deformation and between deformation passes. In industrial processes where the strain rate is high, the dynamic part always dominates during deformation.

Because both internal variables are dislocation densities, their dynamic evolution has a form similar to the one suggested by Kocks in equation (1.18):

$$\left(\frac{\partial \rho_x}{\partial t}\right)_D = \dot{\epsilon} \left(\frac{h_{1,x}}{b} \sqrt{\rho_x} - h_{2,x} \rho_x\right) \quad (x = i, w) \quad (3.6)$$

Where $h_{1,x}$ and $h_{2,x}$ are model parameters, that depend on the deformation temperature and strain rate. The static part is assumed to be governed by climb and follows the form suggested by Caillard and Martin [28] in equation (1.30).

$$\left(\frac{\partial \rho_x}{\partial t}\right)_S = -K_x \frac{\mu b^3}{\pi(1-\nu)} \frac{D}{k_B T} (\rho_x - \rho_{x,eq})^2 \quad (x = i, w) \quad (3.7)$$

The K_x are model parameters. Equilibrium dislocation densities $\rho_{x,eq}$ have been inserted. They correspond to the dislocation densities of a fully recrystallized material. This prevents the stored dislocation density to drop to very small or negative values, which would be non physical. The diffusion coefficient follows an Arrhenius type law:

$$D = b^2 \nu_D \exp\left(-\frac{Q_{bulk}}{k_B T}\right) \quad (3.8)$$

Where Q_{bulk} is the activation energy for bulk-diffusion. It can be argued that the activation energy for pipe diffusion Q_{pipe} makes more sense for growing dislocation loops. Assuming that one knows the respective weights β_p of pipe and β_b bulk diffusion in the climb mechanism, one can calculate an effective activation energy for diffusion Q_{diff} as:

$$\frac{1}{Q_{diff}} = \frac{\beta_p}{Q_{pipe}} + \frac{\beta_b}{Q_{bulk}} \quad (3.9)$$

With $\beta_p + \beta_b = 1$. In the following, only bulk diffusion is considered and equation (3.8) is used.

3.1.4 Model parameters

Determination of the initial values of ρ_i and ρ_w

The yield stress of the material is given by equation (3.4) at zero deformation. It depends on the temperature and on the strain rate through the effective stress τ_{eff} . As mentioned in section 1.3.6, if the processing temperature exceeds a critical temperature, τ_{eff} cancels out. The flow stress becomes:

$$\sigma = M (\tau_{ath} + \tau_d) \quad (3.10)$$

And the yield stress reads:

$$\sigma (\epsilon = 0) = M (\alpha_1 \mu b \sqrt{\rho_{i_0} + \rho_{w_0}} + \tau_d) \quad (3.11)$$

Where ρ_{i_0} and ρ_{w_0} are the dislocation densities at 0 strain. If the second-phase particles are stable in the test conditions, τ_d is constant. Assuming that ρ_{i_0} and ρ_{w_0} are equal and low — which is a reasonable assumption at the very beginning of the deformation when the initial material is partially recrystallized — one only needs to know the value of the yield stress above the critical temperature to assess the initial dislocation densities.

If τ_{eff} does not cancel out, the values of ρ_{i_0} and ρ_{w_0} have to be provided from the literature or from experimental measurements [66]. If we take into account that τ_{eff} is necessarily positive:

$$\tau_{eff} \geq 0 \quad (3.12)$$

Then, from equations (1.3), (1.3) and (3.3) at yield, it comes:

$$\sqrt{\rho_0} \leq \left(\frac{\sigma}{M} - \tau_d \right) / (\alpha \mu b) \quad (3.13)$$

Where $\rho_0 = \rho_{i_0} + \rho_{w_0}$. This gives a criterion on the maximum initial dislocation densities that can be taken for the model. After hot forming and subsequent recovery during slow cooling, the dislocation density is very low. Values in the range 10^9 to 10^{12} m^{-2} are often used [9,25]. Using the parameter values in table 3.1, we find $\rho_0 \leq 1.7 \times 10^{11} \text{ m}^{-2}$.

Determination of ρ_m , Q_{act} and V_{act}

Consider once again the Orowan equation in its differential form (equation (1.8)). If we assume that the dislocation velocity is independent of the deformation temperature, then the mobile dislocation density is only a function of the strain rate $\dot{\epsilon}$.

Let us call $\hat{\sigma}_Y$ the measured values of the yield stress and σ_Y the modelled yield stress. σ_Y is given by substituting ρ_i and ρ_w to ρ_{i_0} and ρ_{w_0} in equation (3.4). At any given strain rate, σ_Y is now a linearly decreasing function of the temperature. Figure 3.2 displays $\hat{\sigma}_Y$ as a function of the temperature, obtained from the plane strain compression tests at 4 strain rates.

Under 100 °C, the yield stress varies slightly with the temperature. The predicted linear decrease really starts only above 100 °C, but does not reach a plateau. This indicates that the critical temperature for this material lies above 400 °C, for every strain rate considered here. The data points also superimpose up to 200 °C. This shows that the strain rate has little to no effect on the yield stress up until 200 °C. Looking at the higher temperatures (300 °C and 400 °C), the yield stress only varies from ≈ 5 to 10 MPa when the strain rate varies one order of magnitude, and the same variation is observed when the temperature increases 50 °C. The strain rate has a much lower effect on the yield stress than the temperature.

Above 100 °C, the assumption that the dislocation velocity is independent of the temperature seems to hold. This means that $Q_{act} - \tau_{eff}V_{act}$ in equation (1.35) has a first order dependency on the temperature.

The value of $\rho_m(\dot{\epsilon})$ is determined by least square regression of σ_Y with $\hat{\sigma}_Y$ above 100 °C. Typically, for a given strain rate, if the flow curves were obtained at I conditions of temperatures, the following objective function is minimized:

$$f_{obj}^1 = \sum_{i=1}^I [\sigma_Y(\rho_m, T_i) - \hat{\sigma}_Y(T_i)]^2 \quad (3.14)$$

If the literature does not provide satisfactory values of Q_{act} and V_{act} , it is possible to include them in the least square regression. For I temperatures and J strain rates, the objective function to be minimized now reads:

$$f_{obj}^2 = \sum_{i=1}^I \sum_{j=1}^J [\sigma_Y(T_i, \dot{\epsilon}_j, Q, V_{act}, \rho_m(\dot{\epsilon}_j)) - \hat{\sigma}_Y(T_i, \dot{\epsilon}_j)]^2 \quad (3.15)$$

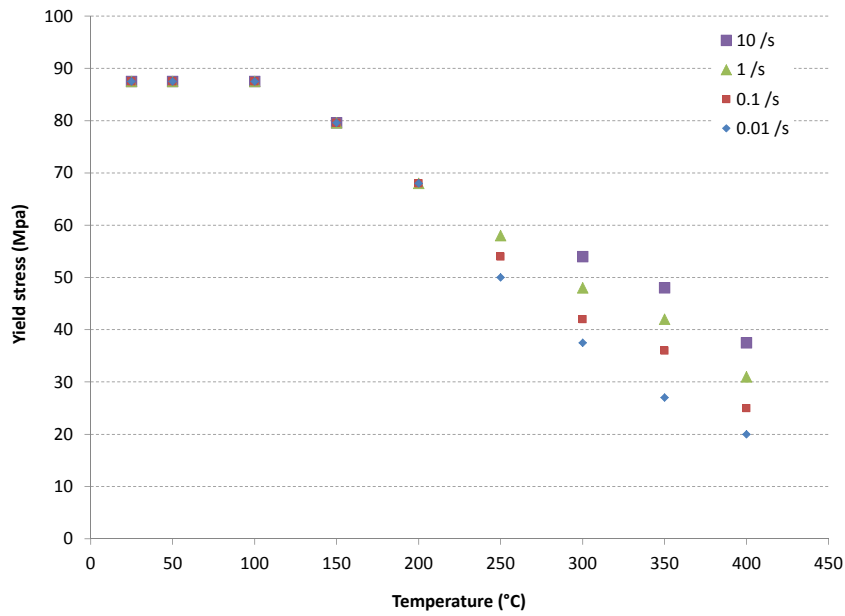


Figure 3.2: Measured yield stress from plane strain compression tests as a function of temperature. The estimated error on each measurement point is ± 7 MPa.

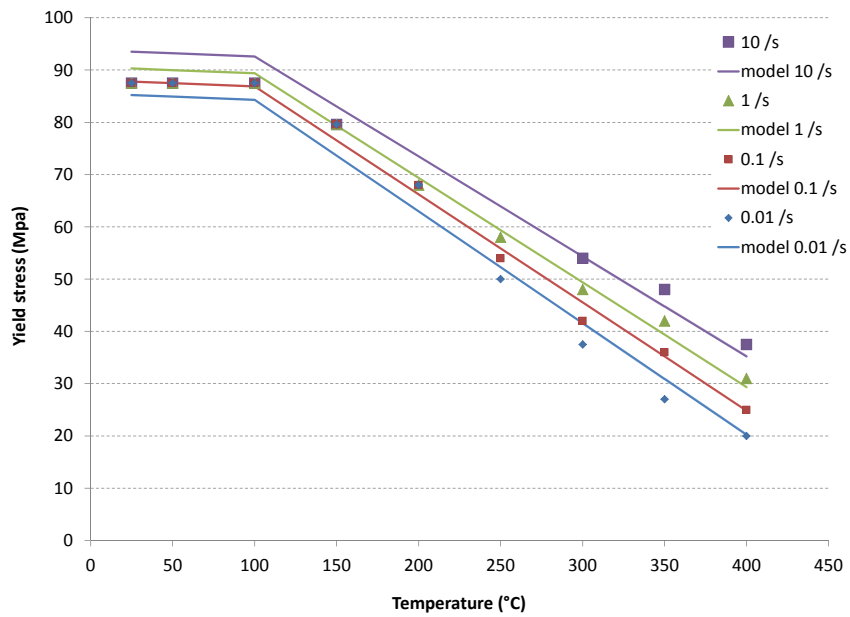


Figure 3.3: Superimposed modelled and measured yield stress as a function of temperature.

Where Q , V_{act} and the values of ρ_m for all strain rates have to be optimized simultaneously. The uniqueness of the solution can be guaranteed by providing a number of data points equal or greater than the number of unknown parameters. In the current study, the system was overdetermined by using 22 data point.

After optimization, the following relationship was determined:

$$\ln \left(\frac{\rho_m}{\rho_m^*} \right) \approx 0.65 \ln \left(\frac{\dot{\epsilon}}{\dot{\epsilon}^*} \right) + 2.28 \quad (3.16)$$

With $\rho_m^* = 10^{10} \text{ m}^{-2}$ and $\dot{\epsilon}^* = 1 \text{ s}^{-1}$ being the normalization dislocation density and strain rate, respectively. Alternatively:

$$\frac{\rho_m}{\rho_m^*} \approx e^{2.28} \left(\frac{\dot{\epsilon}}{\dot{\epsilon}^*} \right)^{0.65} \quad (3.17)$$

Coming back to equation (1.8), this yields the following form of relationship between the dislocation velocity and the strain rate:

$$\bar{v} = p \frac{(\dot{\epsilon})^{1-q} (\dot{\epsilon}^*)^q}{b\rho_m^*} \quad (3.18)$$

With $p = Me^{-2.28}$ and $q = 0.65 < 1$ in our case.

The modelled yield stress is showed in figure 3.3. Below 100 °C, the effective stress was made to be only affected by the strain rate. The initial small decrease in yield stress with temperature is due to the decrease of the shear modulus. The model shows a good fit with the experiments at higher temperatures, and an acceptable fit at lower temperatures.

Parameter values

The values of the parameters used in the model are given in table 3.1. They were obtained from the literature or from optimization of the yield stress of the material.

Parameter	Value	Unit
b	2.86×10^{-10}	m^{-1}
k_B	1.38×10^{-23}	J K^{-1}
K_x	[0.01–1]	-
M	3.06	-
Q_{act}	[1–3]	eV
Q_{bulk}	[0.5–1.5]	eV
V_{act}	$[1–50] \times 10^{-27}$	m^3
α_1	0.5	-
μ	$(8.48 - 0.0406T)/(2(1 + \nu))$	GPa
ν	0.33	-
ν_D	1.5×10^{13}	s^{-1}
ρ_{i_0}	$[10^{10}–10^{12}]$	m^{-2}
ρ_m	$[10^{10}–10^{14}]$	m^{-2}
ρ_{w_0}	$[10^{10}–10^{12}]$	m^{-2}
$\rho_{x,eq}$	$[10^{10}–10^{12}]$	m^{-2}
χ''	$\sqrt{2}$	-

Table 3.1: Model Parameters

Temperature °C	$h_{1,i}$	$h_{2,i}$	$h_{1,w}$	$h_{2,w}$
25	0.018	12	0.0055	1.5
50	0.017	12	0.0055	1.5
100	0.0165	13.5	0.0055	1.5
150	0.016	14	0.0055	1.5
200	0.010	21	0.0030	1.5
250	0.008	25	0.0020	1.5
300	0.004	30	0.0015	1.5
350	0.002	35	0.0010	1.5
400	0.002	35	0.0010	1.5

Table 3.2: Average rate parameter value per temperature.

3.2 Model results

3.2.1 Flow curves and rate parameters

The output of the model depends obviously of the values given to the rate parameters $h_{1,x}$ and $h_{2,x}$ ($x = i, w$). Those can be optimized by comparing the model output with the experimental flow curves. An average value per temperature has been worked out for each parameter, and is reported in table 3.2.

Figure 3.4 shows the flow curves modelled with those parameters together with the experimental data. A seemingly good match was obtained. As expected, the strain hardening depends strongly on the temperature, especially at higher temperatures. One strong feature of the model is that it entirely captures the temperature and strain rate dependency of the yield stress of the material. Now by having a closer look, the flow stress generally appears overestimated at low strain rates, and underestimated at higher strain rates. This reflects the lack of dependency to the strain rate of the parameters $h_{1,x}$ and $h_{2,x}$ ($x = i, w$). Let us call ζ the mean square error of the model:

$$\zeta^2 = \frac{1}{J} \sum_{j=1}^J (\sigma_j - \hat{\sigma}_j)^2 \quad (3.19)$$

Where J is the total number of computed points, over all temperatures and all strain rate, the σ_j are the modelled values of the flow stress and the $\hat{\sigma}_j$ the corresponding experimental points. Using the coefficients in table 3.2 gives the error $\zeta = 76.4$ MPa. The strain rate dependency of the parameters was introduced via the following corrections:

$$h_{1,x}^{corrected} = h_{1,x} \left(1 + \xi \ln \left(\frac{\dot{\epsilon}}{\dot{\epsilon}_0} \right) \right) \quad (3.20)$$

$$h_{2,x}^{corrected} = h_{2,x} \left(1 - \xi \ln \left(\frac{\dot{\epsilon}}{\dot{\epsilon}_0} \right) \right) \quad (3.21)$$

Where $\dot{\epsilon}_0 = 1 \text{ s}^{-1}$, and ξ is the correction factor. Setting ξ to 1/75 brings ζ down to 9 MPa. Figure 3.5 shows the corrected flow curves.

In practice, one can determine the parameters for $\dot{\epsilon} = \dot{\epsilon}_0$, whereby $\ln \dot{\epsilon}/\dot{\epsilon}_0 = 0$, and use a correction factor for the other strain rates. The flow curves will be shifted down at strain rates lower than $\dot{\epsilon}_0$, and up at strain rates greater than $\dot{\epsilon}_0$.

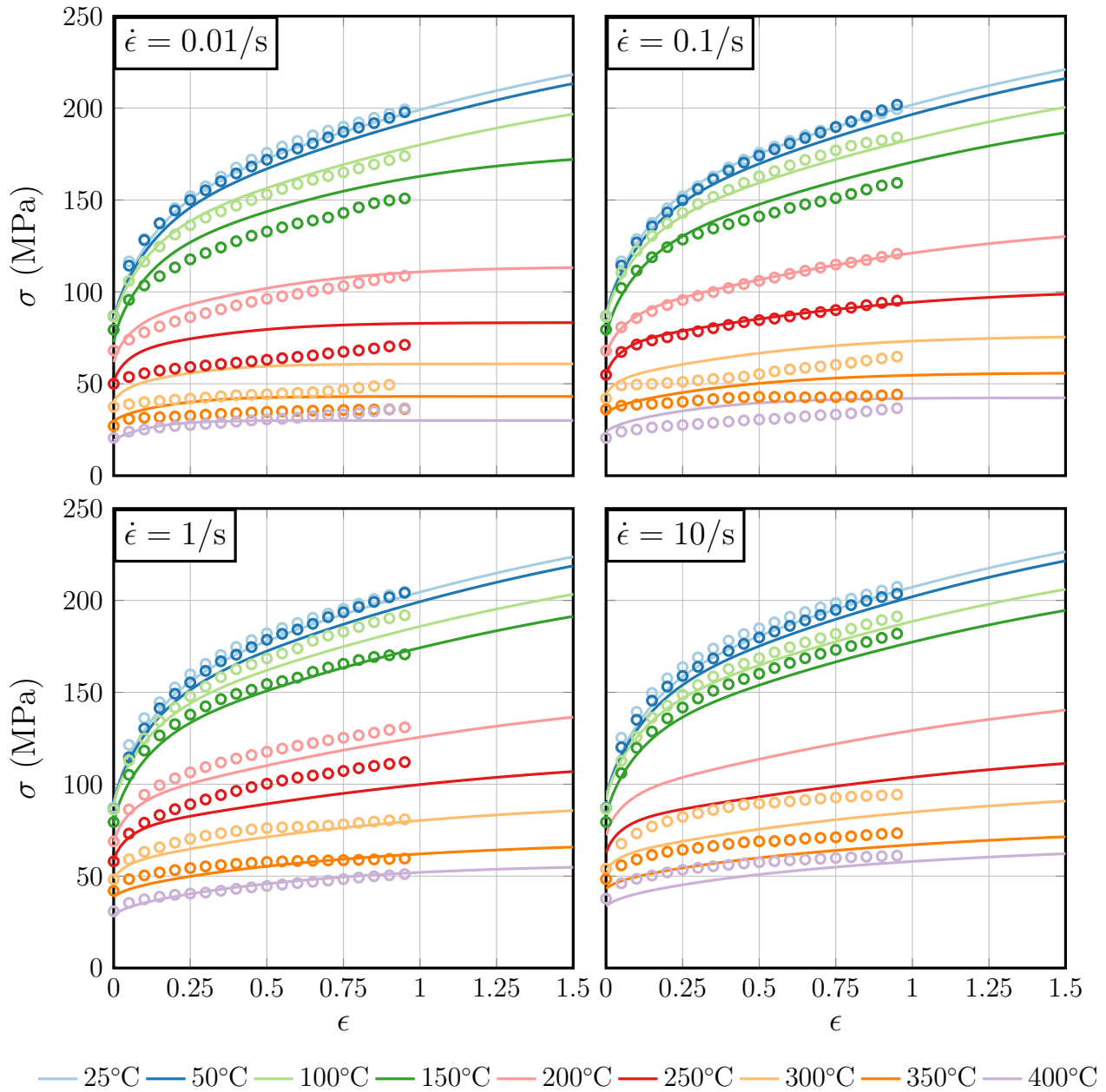


Figure 3.4: Superimposed modelled (lines) and experimental (markers) flow curves.

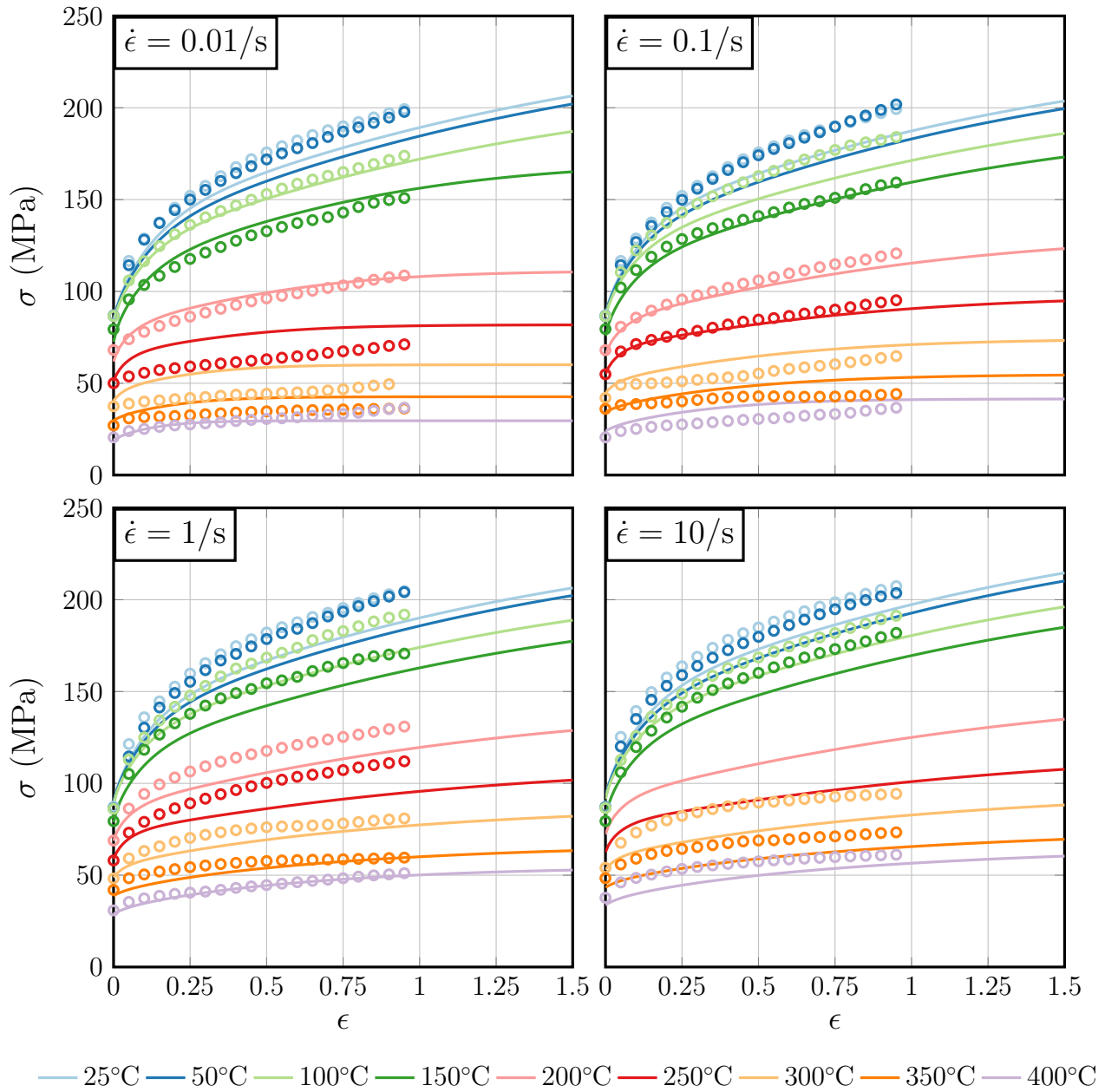


Figure 3.5: Superimposed modelled (lines) and experimental (markers) flow curves. The rate parameters are corrected by $\xi = 1/75$.

3.2.2 Athermal stress, effective stress

The athermal stress and the effective stress are reported in figures 3.6 and 3.7, respectively. The strain rate has no influence on them under 150 °C, which was expected since the flow stress has no dependency on the strain rate at low deformation temperatures.

τ_{ath} grows rapidly at 200 °C and under, and slower when the temperature increases. At 0.01 s^{-1} it even ends up saturating at moderate to high temperatures. This is due to the static part of the evolution rates that is not negligible any more.

τ_{eff} saturates at all temperatures and strain rates. The temperature has no influence under 100 °C, given the model design. Above 100 °C the curves are regularly spaced, following the linearity of equation (1.37). Note that the effective stress is never negative, even at 400 °C and 0.01 s^{-1} . If it had become negative, it should have been nullified for consistency.

3.2.3 Dislocation densities

The evolution of ρ_i and ρ_w is shown in figures 3.8 and 3.9, respectively.

ρ_i increases rapidly at the very beginning of the deformation and saturates very soon. There is no influence of the strain rate because the evolution parameters in table 3.2 are strain rate independent. The rapid saturation indicates that there is a limit to storage capacity of the subgrain interiors.

ρ_w also increases rapidly at the beginning of the deformation, and slower passed $\epsilon \approx 0.1$. It does not saturate, except at 0.01 s^{-1} above 200 °C where diffusion driven climb of dislocations kicks in. The kinetics of dislocation storage is slower at the beginning of the deformation than for ρ_i , but the persistent increase in ρ_w indicates that the dislocations keep re-arranging in subgrain boundaries. The subgrain boundaries however cannot receive an infinite number of dislocations [6], thus ρ_w can only keep increasing if the subgrain size decreases.

The predicted values of ρ_i and ρ_w at low temperatures are in the range of those predicted in [9, 10, 48] (10^{13} to 10^{14} m^{-2} see section 1.3.9), albeit for higher temperatures, which means that both ρ_i and ρ_w could raise more. The subgrain size however, as calculated by equation (3.22), corresponds approximately to that predicted in [10].

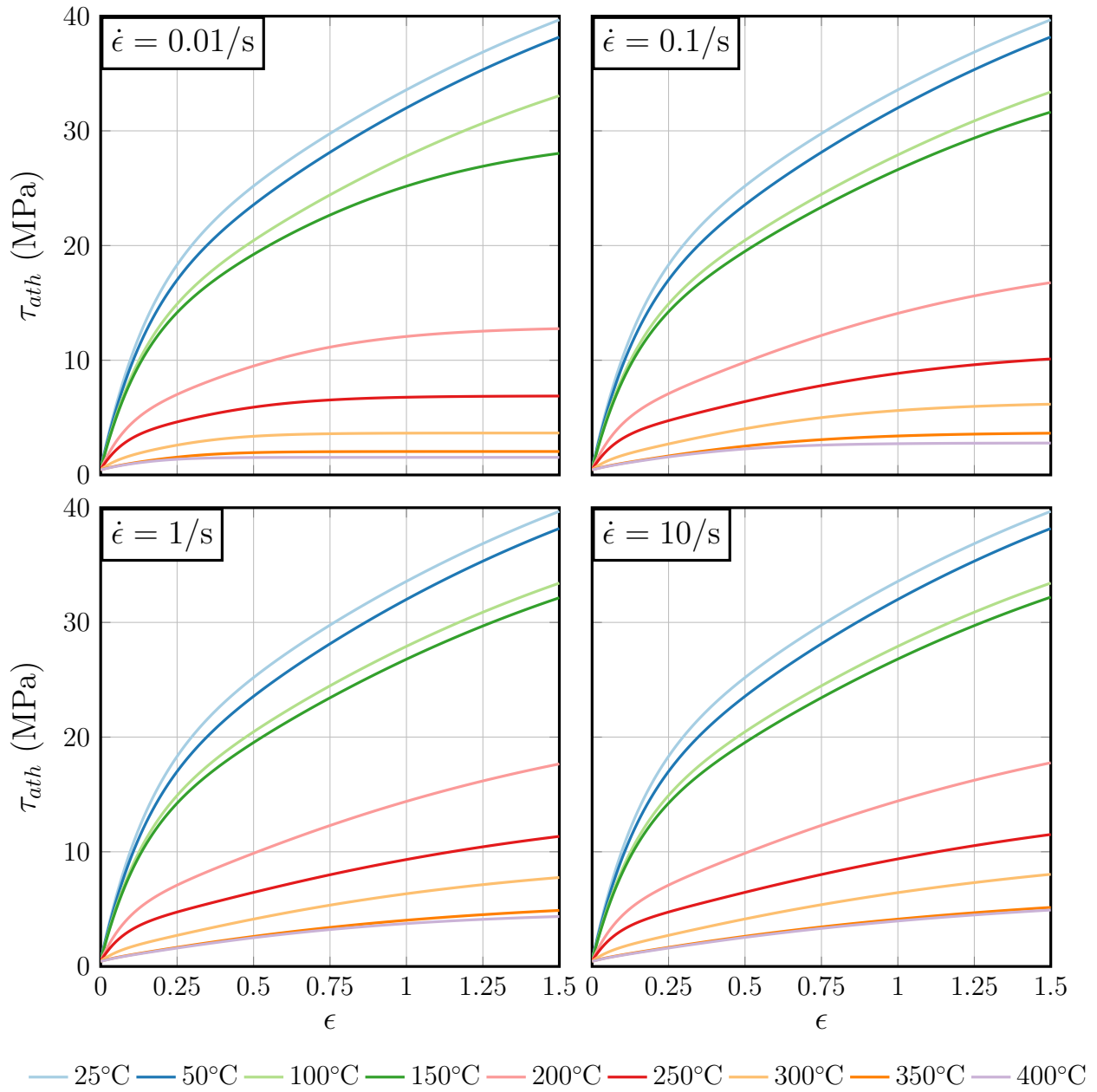


Figure 3.6: Modelled athermal stress.

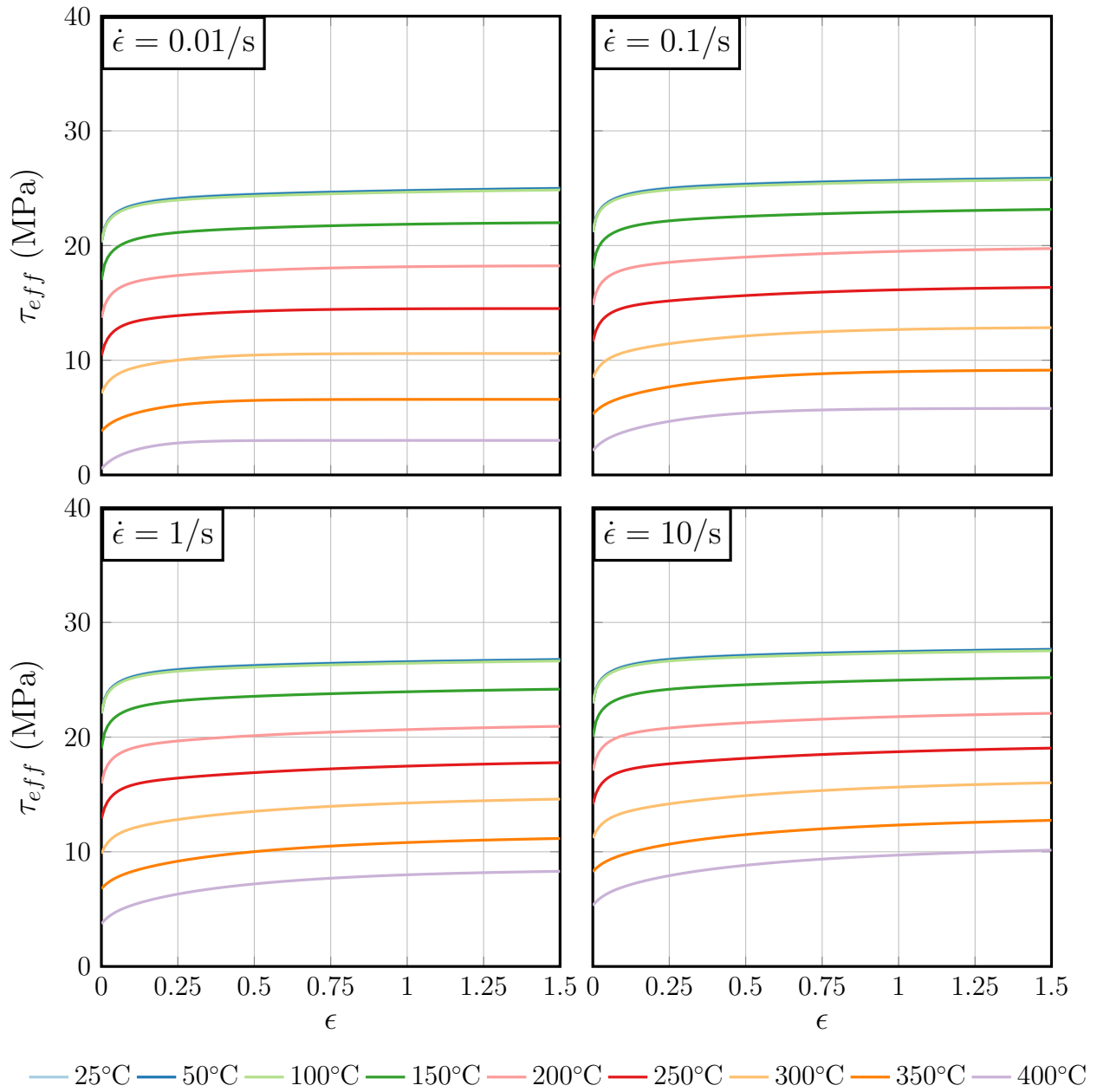


Figure 3.7: Modelled effective stress.

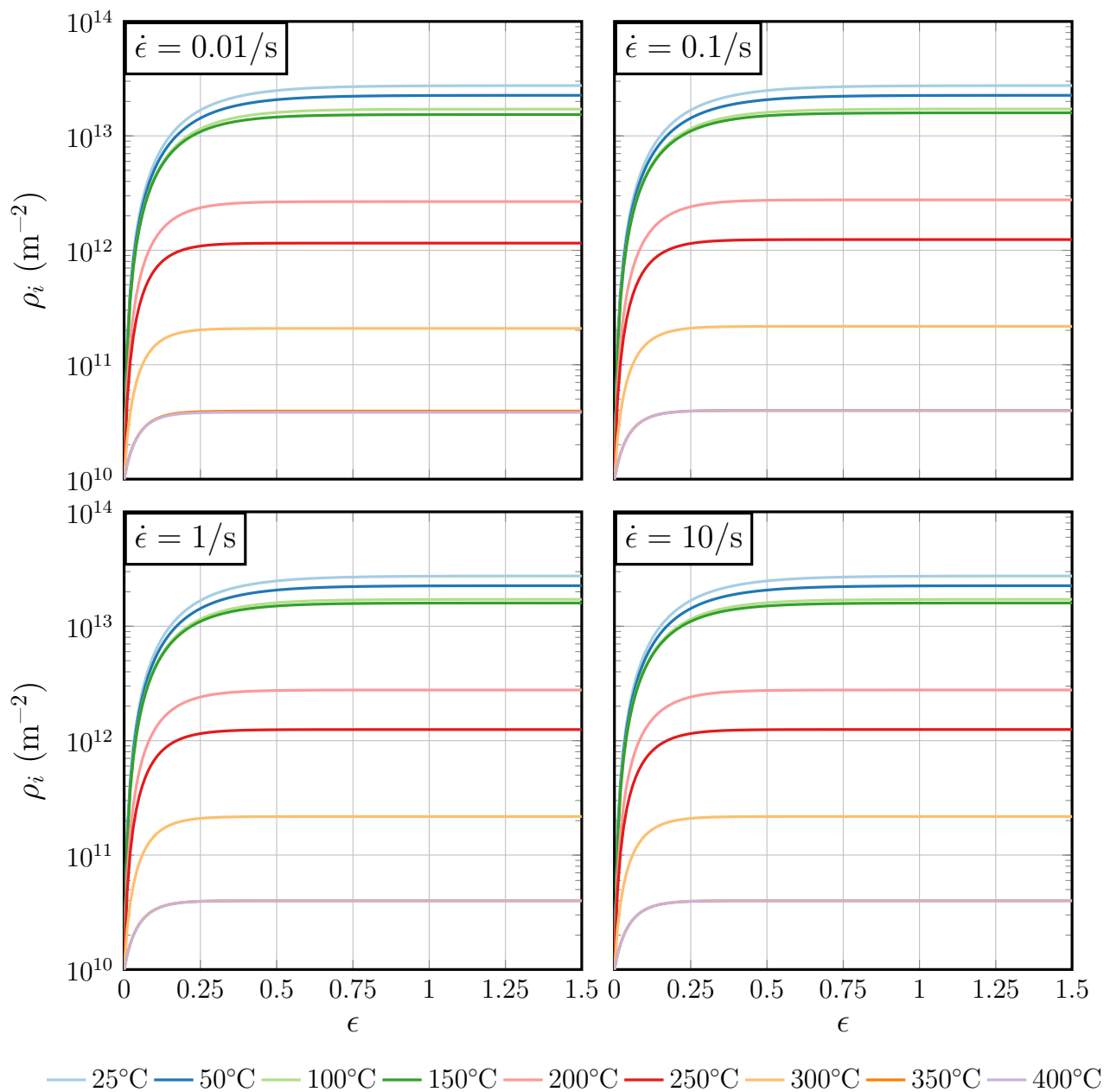


Figure 3.8: Modelled interior dislocation density.

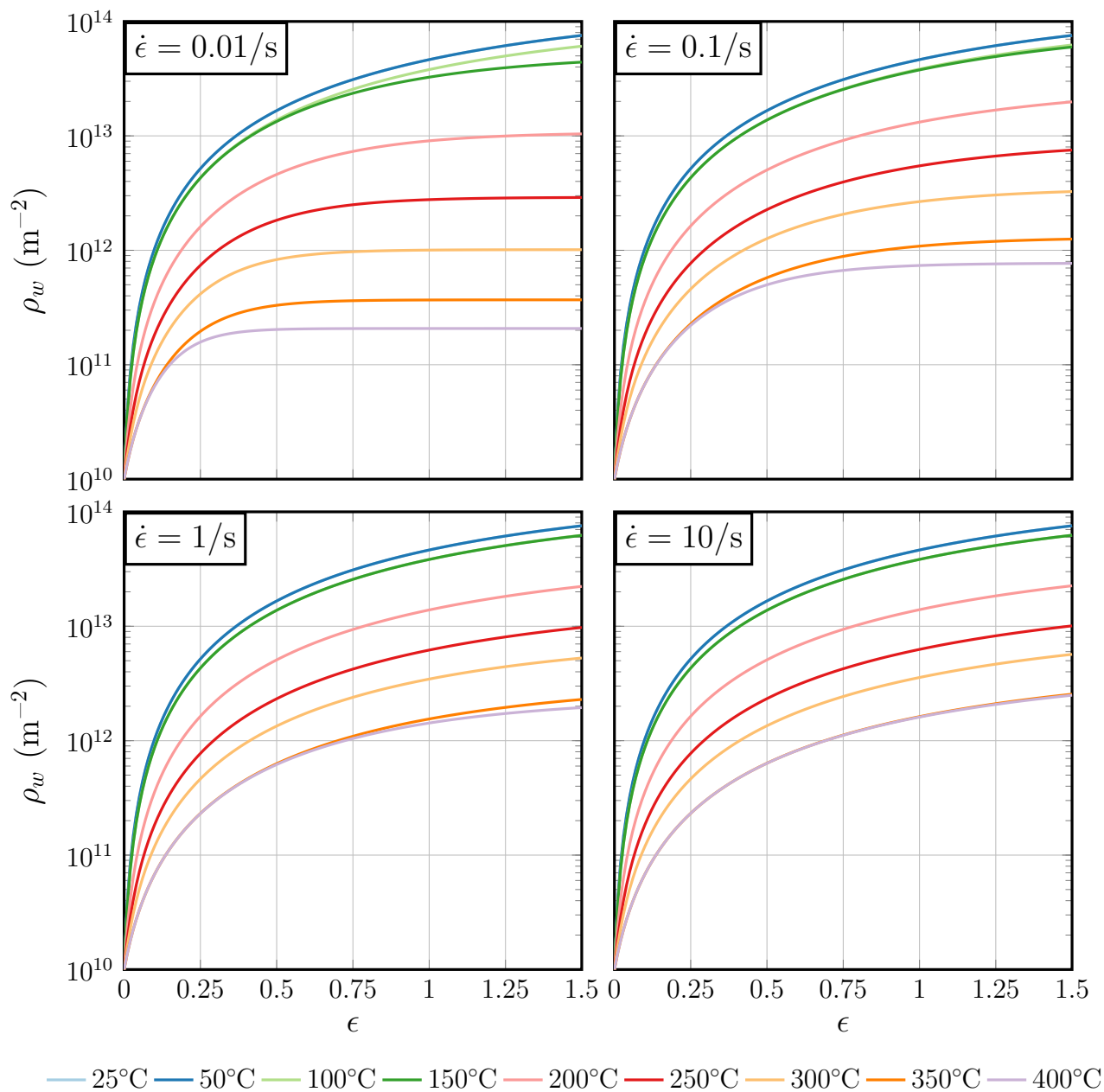


Figure 3.9: Modelled wall dislocation density.

3.2.4 Subgrain size

The subgrain size δ can be calculated from ρ_w in one of two ways [6, 10].

Physically, if the subgrain boundaries are assumed to be tilt boundaries of average misorientation $\bar{\theta}_{sg}$, and if the wall dislocation density can be averaged over the microstructure, then the subgrain size δ is given by [67]:

$$\delta = \frac{\kappa \bar{\theta}_{sg}}{b \rho_w} \quad (3.22)$$

Where κ is a shape factor and $\bar{\theta}_{sg}$ is the average subgrain misorientation angle. This approach assumes that the wall dislocations form a network so dense, that their density can be averaged over a whole representative element, even though they are by definition located in the subgrain boundaries only.

However, when the flow stress reaches a steady state during high temperature deformation, δ follows an empirical relationship of the form [56, 68]:

$$\delta \propto \rho_i^{-0.5} \quad (3.23)$$

In that context, when ρ_i reaches a plateau, so does the subgrain size, and no further hardening is observed.

In the scope of this work, hardening can be observed at all deformation conditions, therefore equation (3.23) cannot apply. Using equation (3.22), equation (3.1) rewrites as:

$$\rho = \rho_i + \frac{\kappa \bar{\theta}_{sg}}{b \delta} \quad (3.24)$$

Figure 3.10 shows the evolution of the subgrain size calculated using equation (3.22), with $\kappa = 3$ and $\bar{\theta}_{sg} = 3$ degrees. The steady increase in ρ_w , responsible for the persistent hardening, translates into substructure refinement.

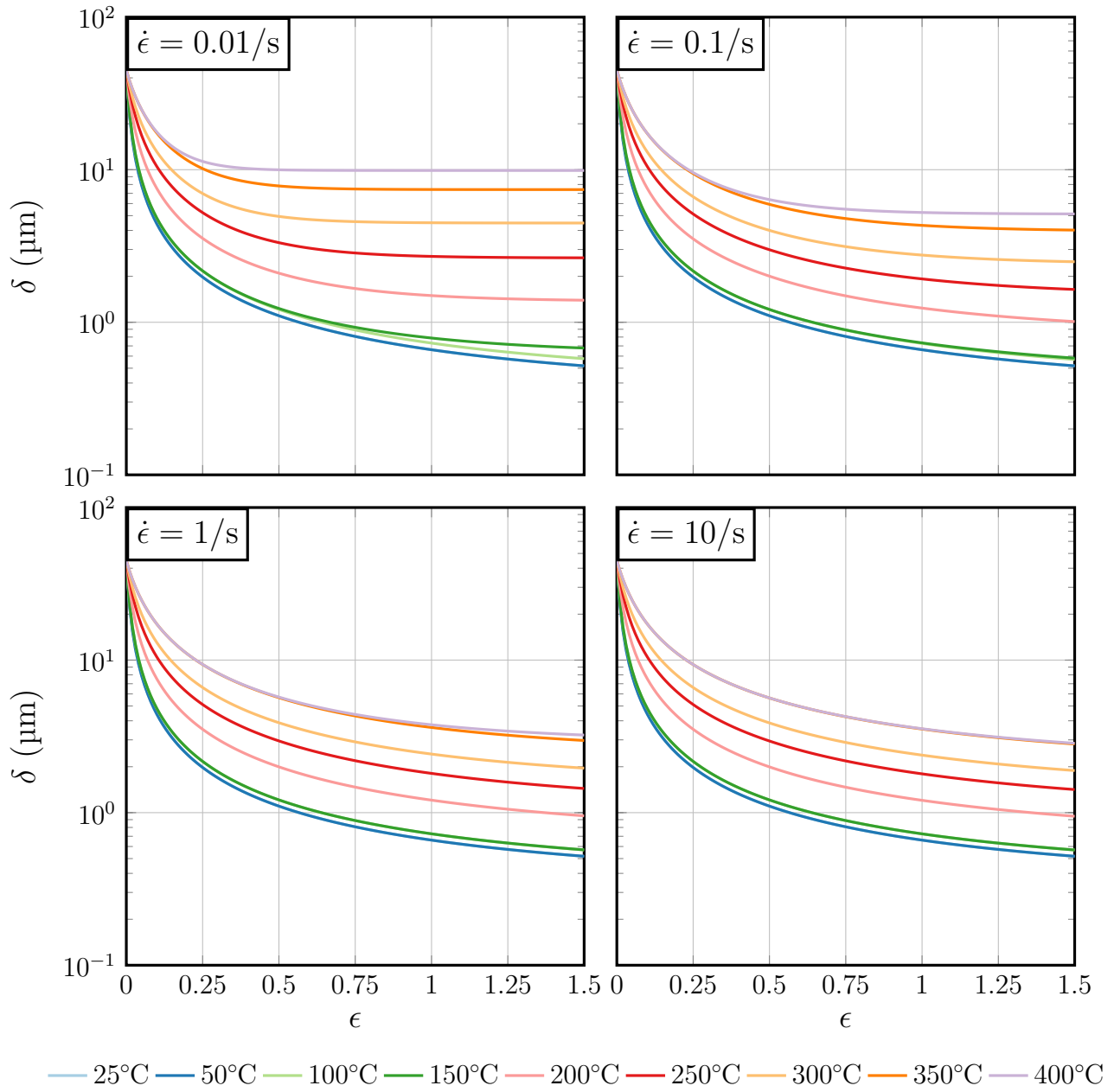


Figure 3.10: Modelled subgrain size.

Chapter 4

Recrystallization

Quite some work has already been done in modelling recrystallization and subsequent grain growth (section 1.4). The overall aim is to predict the evolution of the grain size and the recrystallized fraction during annealing. A recrystallization model has been developed here in the wake of the flow stress model developed in chapter 3. Experimental work has been carried out to observe recrystallization after cold deformation in order to calibrate the recrystallization model and validate its output.

4.1 Experimental characterization

4.1.1 Experiments

Samples deformed in plane strain compression at room temperature were further oven annealed at 300 °C and 400 °C to induce recrystallization. For each temperature, the treatment was interrupted after 10 s, 1 min, 5 min, 20 min and 1 h and the samples were water quenched. The microstructure evolution was observed with EBSD in regions of local strain 1 and 1.5. The experimental procedure is detailed in section 2.1.5. The analysis of the EBSD data was initiated in a collaborative project and is credited to M. Spuller [69].

In the annealing experiments, the samples were placed cold in a warm oven. The heat treatment was thus not isothermal and the heating rate was not controlled. In order to use the right heating rate for modelling, the temperature profile in the samples was determined by finite element simulations of the annealing tests. The simulations were run in DEFORM2DTM after plane strain compression at room

Temperature °C	Thermal capacity $\text{J kg}^{-1} \text{K}^{-1}$	Thermal conductivity $\text{W m}^{-1} \text{K}^{-1}$
20	888	160
100	924	169
150	947	175
200	970	187
250	992	199
300	1015	202
350	1038	201
400	1060	200
450	1083	199
500	1106	195
550	1128	188

Table 4.1: Thermal capacity and conductivity measured by DSC. Data provided by the Austrian Institute of Technology.

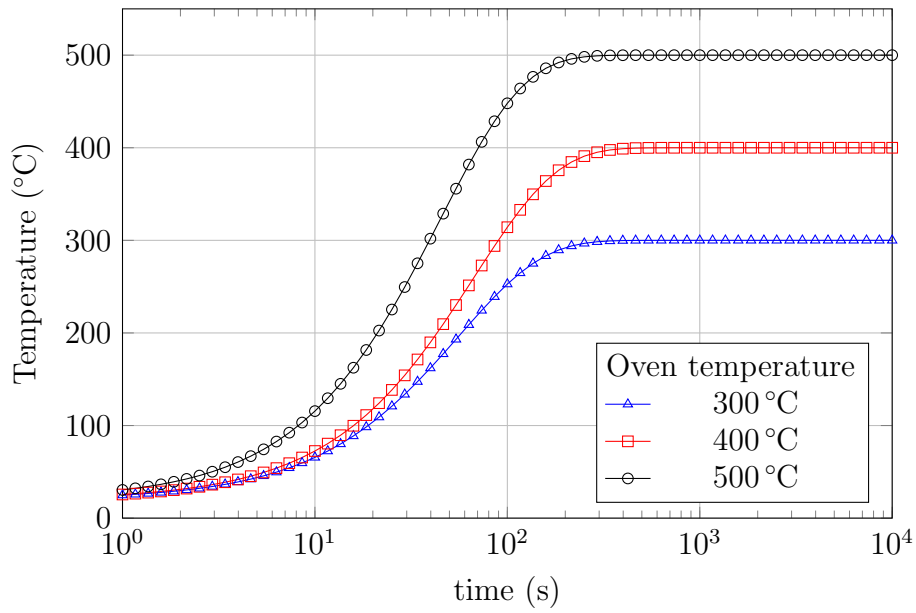


Figure 4.1: Temperature evolution in the workpiece during annealing at 300 °C, 400 °C and 500 °C.

temperature. The workpiece was placed in an air atmosphere at 300 °C or 400 °C for 1 h. An additional treatment at 500 °C was performed to test the prediction capability of the model. Heat exchange was allowed on the whole interface between the workpiece and the atmosphere, whose convective heat transfer coefficient was set to 0.02 N s⁻¹ mm⁻¹ K⁻¹. The thermal capacity and the thermal conductivity of the material were determined by Differential Scanning Calorimetry (table 4.1), and its emissivity was set to 0.7.

The temperature profiles in the middle of the sample during the first 10 minutes are shown in figure 4.1. They were fit with an equation of the form:

$$T = T_i + (T_a - T_i) \exp\left(-\frac{t}{t^*}\right) \quad (4.1)$$

Where T_i is the initial sample temperature, set at 20 °C, T_a is the temperature of the surrounding atmosphere, i.e. the oven temperature and t^* is a characteristic time to be determined. Least square regressions yielded the following values of t^* : 67.2 s at 300 °C, 56.2 s at 400 °C and 45.0 s at 500 °C.

4.1.2 Experimental results

Figure 4.2 shows the inverse pole figure of the microstructure in the cold deformed state. The deformed grains are elongated on several millimeters along the deformation path and contain internal boundaries due to local matrix rotations. A strain of 1.5 is achieved in the deformation cross, whereas a strain of 1 is achieved towards the edge of the picture. Accordingly the grains are much thinner in the cross than on the edges.

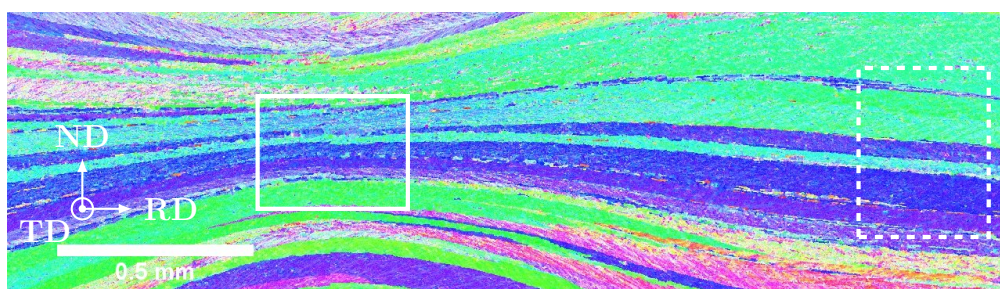


Figure 4.2: IPF map of a sample deformed in plane strain compression. The region of strain 1.5 is highlighted in plain and the region of strain 1 is highlighted with a dashed line.

Figure 4.3 shows the evolution of the grain structure after annealing at 300 °C. Black lines highlight boundaries with a misorientation larger than 10°. Recrystallization clearly occurs between 5 and 20 min in the deformation cross, where the stored energy of deformation is higher, i.e. where the driving pressure for recrystallization is higher. The recrystallized grains are free of inner boundaries, in contrast with the deformed matrix. After 1 h of annealing, the region of lower strain is also recrystallized. The grains are elongated in the direction of previous deformation and their thickness is similar to that of the deformed grains in figure 4.2, i.e. roughly 50 to 100 μm . The grains are longer in the region of strain 1 than in the deformation cross, where more grains are able to nucleate and impinge upon each other during growth.

Figure 4.4 shows the evolution of the grain structure after annealing at 400 °C. Black lines highlight boundaries with a misorientation larger than 10°. New grains are readily formed after 1 min of annealing within the deformation cross. After 5 min, the whole microstructure is recrystallized. The grain size varies also inversely to the strain grade, though in a lower extent than at 300 °C. The effect of strain on nucleation appears to be greatly reduced by the increase in temperature. In a general manner, the grains are much smaller than after annealing at 300 °C.

At both annealing temperatures, the sample temperature nears that of the oven after only 200 s of annealing (section 4.1.1). This time is well reflected at 400 °C, where new grains are formed within a minute, but not at all at 300 °C, where recrystallization is first observed after 20 min of annealing. This seems to indicate that there is an incubation time during which newly formed grains cannot grow.

In the light of those experiments, the following conclusions can be drawn and should be reflected in the model:

1. The nucleation process is affected by the strain grade achieved during deformation prior to annealing and by the annealing temperature.
2. The boundary pinning by bigger aluminides oriented in the direction of deformation effectively stops the boundary migration during recrystallization.
3. After being stopped in one direction, grain growth is two dimensional.
4. The boundary pinning by small aluminides can counter balance the capillarity effects.
5. Recrystallization happens, as expected, faster at higher temperature.

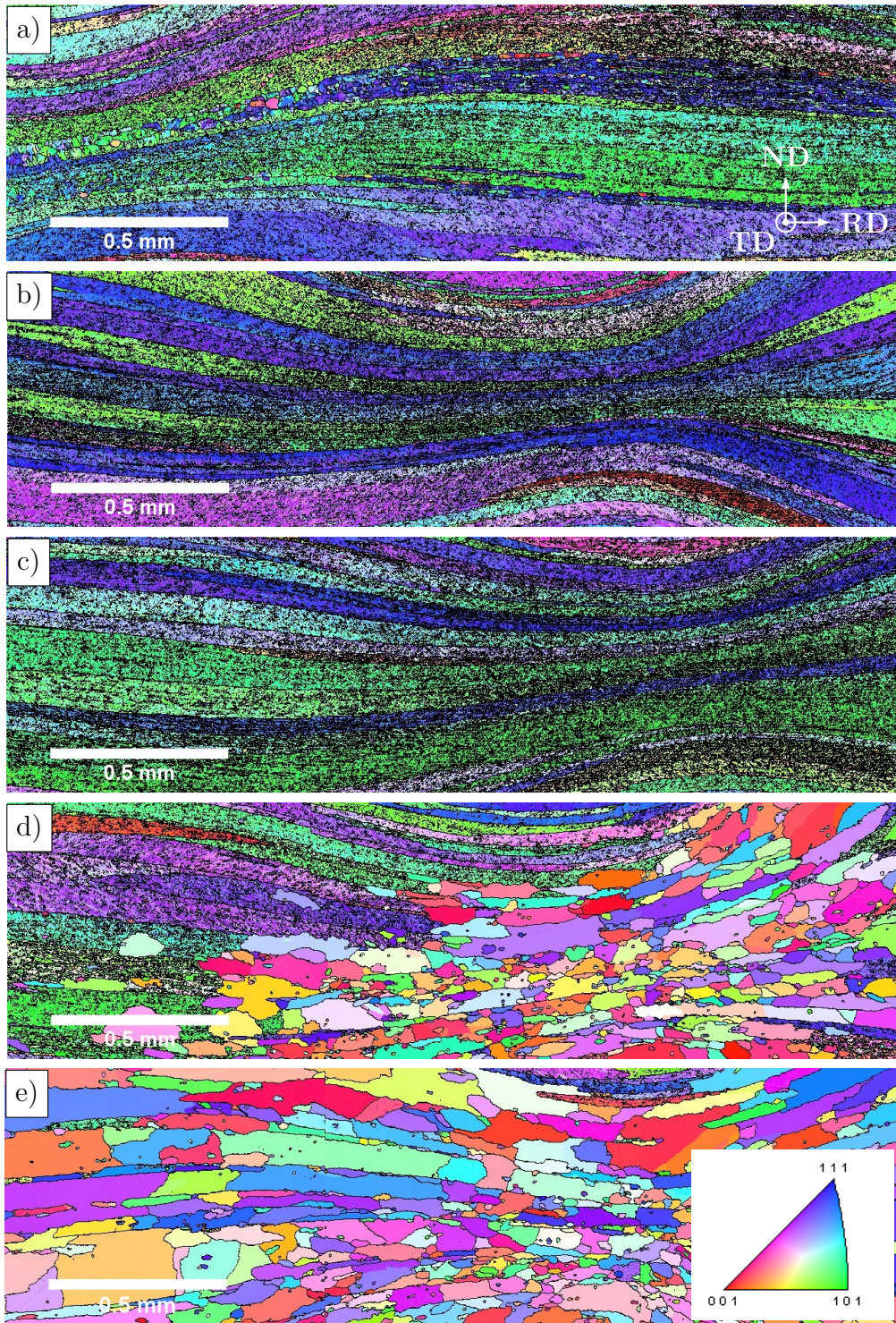


Figure 4.3: IPF maps of cold deformed samples annealed at 300 °C for a) 10 s, b) 1 min, c) 5 min, d) 20 min and e) 1 h.

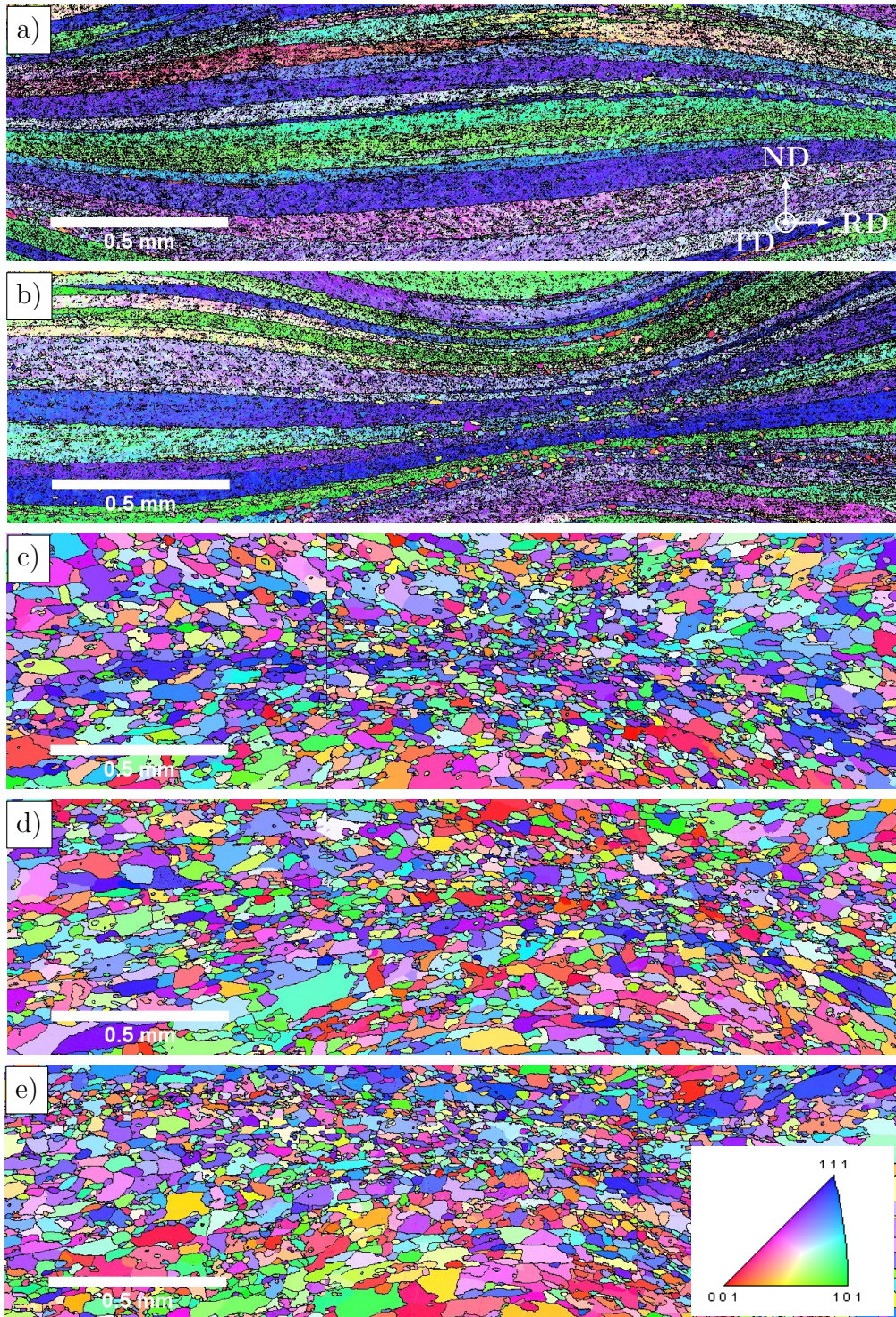


Figure 4.4: IPF maps of cold deformed samples annealed at 400 °C for a) 10 s, b) 1 min, c) 5 min, d) 20 min and e) 1 h.

4.2 Recrystallization model

4.2.1 Model set-up

Any recrystallization model must take into account two phenomena: the nucleation of new grains, and their growth. This can be done by supplying a Johnson Mehl Avrami Kolmogorov type equation either with adequate constants, or with adequate nucleation and growth rates. Although the latter is now pretty straightforward, properly assessing the nucleation rate remains an issue, which is often dealt with by supplying a phenomenological equation. Physically based models for nucleation exist, but they are often coupled with complex texture models (see [36, 37] for example) and are of little use for industrial applications.

Concurrently to recrystallization, the microstructure recovers during annealing. The stored energy decreases, and so does the pressure on the grain boundaries. This affects recrystallization in two ways:

- The critical radius for nucleation is inversely related to the pressure on the boundaries (equation (1.66)). When the stored energy drops, the critical radius increases, which heavily reduces the nucleation rate.
- The growth rate of the grains being proportional to the pressure on their boundaries (equation (1.67)), a decrease in the latter slows down the overall kinetics of recrystallization.

Additionally the experimental observations show that the level of strain reached during deformation prior to annealing can considerably influence the recrystallization kinetics.

The following model was developed as a follow up on the prior flow stress model. It makes use of the same internal variables, namely the cell interior dislocation density ρ_i and the cell wall dislocation density ρ_w and the mobile dislocation density ρ_m . The output of the constitutive model can therefore directly be used as input for this recrystallization model. Recovery is enabled by setting up the evolution rates of the internal variables.

The model addresses nucleation from a geometric point of view, which yields an explicit relationship to the local strain in the material. The nucleation rate is made time and temperature dependent in order to allow for recovery and non isothermal treatments.

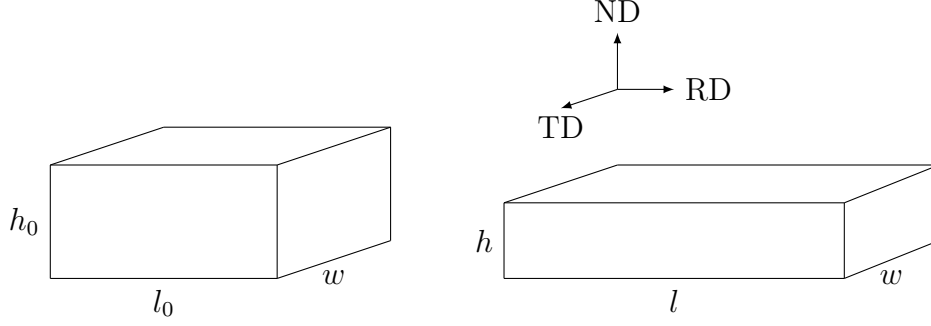


Figure 4.5: Grain geometry before (left) and after (right) deformation.

Nucleation rate

In a concurrent study by P. Loidolt [63], it was found that strain induced boundary migration was the dominant nucleation mechanism in our alloy, which is supported by the literature [6]. As bulging happens in consequence of thermal fluctuations in free energy, the probability of it happening is a function of temperature. The nucleation frequency per unit volume is often given an Arrhenius form.

Let us assume that the grains are rectangle parallelepipeds, as shown in figure 4.5. Prior to deformation, they have a length l_0 in the rolling direction, a height h_0 in the normal direction and a width w in the transverse direction, assimilated to the measured grain sizes in section 2.2. During plane strain compression as described in section 2.1.1, the deformation is two dimensional in the plane formed by the rolling direction and the normal direction. According to equation (2.1), the height h of a deformed grain reads:

$$h = h_0 \exp(-B|\epsilon|) \quad (4.2)$$

Where B is a constant equal to $\sqrt{3}/2$ for plane strain compression tests. The volume conservation of the grains reads:

$$lhw = l_0h_0w \Leftrightarrow l = \frac{l_0h_0}{h} \quad (4.3)$$

l being the length of a deformed grain. Combining equations (4.2) and (4.3) yields:

$$l = l_0 \exp(B|\epsilon|) \quad (4.4)$$

The grain boundary area of one deformed grain is $2(lh + lw + hw)$. In a regular network of deformed grains, each boundary is shared between two grains. Hence the area of grain boundary available in a volume element of size $l \times h \times w$ is equal to $(lh + lw + hw)$.

The volume density ρ_A of grain boundary area then reads:

$$\rho_A = \frac{lh + lw + hw}{lhw} \quad (4.5)$$

For a critical bulge radius R_b , the area of boundary that bulges is πR_b^2 (see section 1.4.3). Potentially, the number of bulges that can form reaches a maximum when the available grain boundary area is saturated with bulges. The maximum density of bulges ρ_b^{max} hence reads:

$$\rho_b^{max} = \frac{\rho_A}{\pi R_b^2} \quad (4.6)$$

Let us assume that at any given time t , there is a given volume density ρ_b of sites lying on the boundaries of deformed grains that have the potential to bulge in the neighbouring grain, in consequence of local variations in stored energy. ρ_b can be taken as a fraction χ_b of ρ_b^{max} . As the distribution of bulge sizes is not known, χ_b must be allowed to vary with the strain.

$$\rho_b = \chi_b(\epsilon) \rho_b^{max} \quad \chi_b \in [0; 1] \quad (4.7)$$

Combining equations (1.66), (4.2) and (4.4) to (4.7) yields:

$$\rho_b = \frac{\chi_b(\epsilon)}{4\pi\gamma_b^2} P^2 \left(\frac{1}{w} + \frac{\exp(B|\epsilon|)}{h_0} + \frac{\exp(-B|\epsilon|)}{l_0} \right) \quad (4.8)$$

P being the driving pressure for recrystallization. As recovery onsets, P decreases with time, and so does ρ_b .

Let ν_{nucl} be the frequency at which a bulging event happens. The nucleation rate $\dot{N}(t)$ per unit volume then reads:

$$\dot{N}(t) = \nu_{nucl} \rho_b(t) \quad (4.9)$$

As bulging happens in consequence of thermal fluctuations in free energy, the probability of it happening is a function of the temperature T . ν_{nucl} can be written under the form [53, 55]:

$$\nu_{nucl}(T) = \nu^* \exp\left(-\frac{Q_{nucl}}{k_B T}\right) \quad (4.10)$$

Where ν^* is a characteristic frequency and Q_{nucl} is the activation energy for nucleation.

Combining equations (4.8) to (4.10) yields the following nucleation rate:

$$\dot{N} = \dot{N}^*(\epsilon) \frac{P^2}{\gamma_b^2} \left(\frac{1}{w} + \frac{\exp(B|\epsilon|)}{h_0} + \frac{\exp(-B|\epsilon|)}{l_0} \right) \exp\left(-\frac{Q_{nucl}}{k_B T}\right) \quad (4.11)$$

With $\dot{N}^*(\epsilon) = \chi_b(\epsilon) \nu^*/4\pi$. This criterion includes both the thermal activation of recrystallization and the effects of recovery. In practice, $\dot{N}^*(\epsilon)$ is a model parameter that needs to be adjusted.

Recovery

The microstructure representation is the same as described in figure 3.1. The evolution rate ρ_i is simply given by equation (3.7), where only static recovery by climb is considered:

$$\frac{\partial \rho_i}{\partial t} = -K_i \frac{\mu b^3}{\pi(1-\nu)} \frac{D}{k_B T} (\rho_i - \rho_{i,eq})^2 \quad (4.12)$$

During recovery, the wall dislocations rearrange in stable arrays. Their density can no longer be averaged over the microstructure, and the subgrain size cannot be calculated from equation (3.22) anymore. Instead, it is preferable to use a capillarity driven growth mechanism for the subgrain boundaries [6]:

$$\frac{1}{2} \frac{\partial \delta}{\partial t} = M_{sg} \left(\frac{3\gamma_{sg}}{\delta} - P_Z \right) \quad (4.13)$$

Where γ_{sg} is the specific energy of the low angle grain boundaries, given by a Read and Shockley relationship of the form:

$$\gamma_{sg} = \frac{\mu b \theta}{4\pi(1-\nu)} \ln \left(\frac{e\theta_c}{\theta} \right) \quad (4.14)$$

θ being the subgrain average misorientation, θ_c the critical misorientation for a low angle boundary to turn into a high angle boundary (typically 10–15°), e the natural exponential and ν the Poisson coefficient of the material.

M_{sg} is the mobility of the subgrain boundaries, which has an Arrhenius form (see equation (4.23)).

It has to be mentioned here that both γ_{sg} and M_{sg} are highly dependent on the subgrain misorientation. Humphreys and Hatherly [6] have reported that the average subgrain misorientation decreases during recovery, which should be taken into account in further developments.

P_Z in equation (4.13) is the Zener retarding pressure, as discussed further in equation (4.21).

Stored energy

Stored energy of deformed grains

Because the microstructure is composed of both disorganized dislocations in the cell interiors and dislocations located within the subgrain walls, the volume energy of deformation contributes from both equations (1.57) and (1.59). Within the subgrains, the stored dislocations are the interior and the previously mobile dislocations. The subgrain walls are composed of dislocations arranged in a lower energy configuration. The subgrain size is calculated in the same way than in the flow stress model and is given by equation (3.22).

Assuming a weak interaction between the wall dislocations, the dislocations within the subgrain interiors and the mobile dislocations, the energy of deformation reads:

$$E_D = \alpha \mu b^2 (\rho_i + \rho_m) + \frac{1.5 \gamma_{sg}}{\delta} \quad (4.15)$$

Stored energy of recrystallized grains

The crystalline structure of metallic alloys is not perfect, even for newly recrystallized grains. Those contain a small amount of dislocations, hence an volume energy. Usually, this energy can be neglected in regard of that of the deformed

grains. But because the equilibrium dislocation density in equation (4.12) was defined as the dislocation density of the recrystallized material, we need to consider its energetic contribution. We define the energy of recrystallized grains as:

$$E_D^{RX} = \alpha\mu b^2(\rho_{eq,i}) \quad (4.16)$$

Note that the contribution of the subgrain boundaries does not appear. Since subgrains form upon deformation, the recrystallized grains do not contain any subgrain boundary.

Driving pressure on the grain boundaries

As seen in section 1.4, the difference in volume energy ΔE_D between each side of the boundaries separating the recrystallized grains from the deformed matrix results in a driving pressure P for recrystallization on the boundary. This pressure plays a role in both the nucleation and the growth mechanisms. It is given by:

$$P = \Delta E_D + P_C - P_Z \quad (4.17)$$

P_C being the capillarity pressure and P_Z the retarding pressure of dispersoids.

Usually, the volume energy of the deformed material is considered a lot greater than that of the recrystallized material, and ΔE_D is taken equal to E_D , the volume energy of the deformed material. But because of our definition of an equilibrium dislocation density, ΔE_D reads:

$$\Delta E = E_D - E_D^{RX} \quad (4.18)$$

The capillarity pressure is very small with respect to ΔE_D and can be neglected during recrystallization. During subsequent grain growth however, there is no deformed material left and P_C is the only driving pressure acting on the boundaries. Numerically, recrystallization was considered complete when the fraction of recrystallized material reached 99 %. Equation (4.17) then rewrites as follows for grain growth:

$$P = P_C - P_Z \quad (4.19)$$

P_C is given by equation (1.61) where the grain diameter is replaced by 2 times the average grain radius (equation (4.28)):

$$P_C = \frac{3\gamma_g}{2 \langle R_g \rangle} \quad (4.20)$$

In presence of a dispersion of second-phase particles, the moving boundaries are hindered and grain growth is slowed. In figures 4.3 and 4.4, we have seen that the boundaries are stopped by the primary aluminides located on the former grain boundaries. The finely disperse aluminides and the β -Mg₂Si cannot effectively stop the moving boundaries, but they still exert a retarding pressure on them. Their individual contributions are each given by equation (1.64) and are linearly added:

$$P_Z = \frac{3}{2} \left(\frac{V_f^{al}}{R_{al}} + \frac{V_f^\beta}{R_\beta} \right) \quad (4.21)$$

V_f^{al} and V_f^β are the volume fraction of the small aluminides and the β -Mg₂Si, R_{al} and R_β are their radii, measured in table 2.4.

The larger aluminides, however, are not homogeneously dispersed and the Zener equation cannot be used to describe their contribution. They actually do not exert any effective retarding pressure before the moving boundaries reach their location and get pinned by them. This difficulty was circumvented by numerically limiting the growth in two directions and preventing the boundaries to move beyond the lines of primary aluminides. Figure 4.6 depicts a high angle grain boundary (in red) being stopped at the large white aluminides. The smaller aluminides and the blocky dark β -Mg₂Si retard the boundary motion without stopping it.

The particle drag can nullify the driving pressure, but cannot outwit it, because it would numerically result in a shrinking pressure on the boundaries. Hence whenever the total pressure was found to be negative, it was set to 0, for both recrystallization and growth.

Growth rate

The growth rate \dot{R}_g of recrystallized grains is simply the product of the total pressure P with the mobility of the boundaries M_g (equation (1.67)):

$$\dot{R}_g = M_g P \quad (4.22)$$

M_g is difficult to obtain from the literature because it highly depends on the chemical composition of the alloy, the material state and the direction of movement.

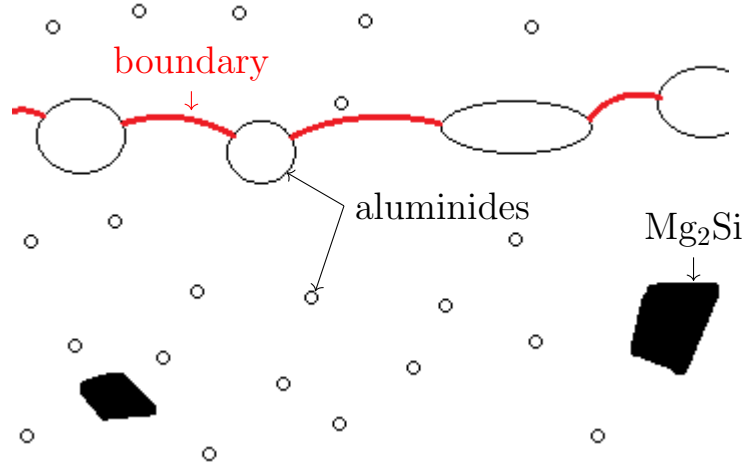


Figure 4.6: Schematics of a boundary (in red) being effectively pinned by the large aluminides.

Therefore, the mobility measurements are always carried out for low alloyed materials, if possible in given directions [70–73]. It is common to assume that the mobility has an Arrhenius form, both for subgrain and grain boundaries:

$$M_y = M_y^* \exp\left(-\frac{Q_{mob}^y}{k_B T}\right) \quad (y = g, sg) \quad (4.23)$$

Any review of the literature yields ranges of mobilities too wide to pinpoint a value suiting our needs (see table 4.2). In the model, the activation energies are picked between 0.5 and 2.5 eV and the pre-exponential factor is fitted adequately.

Extended volume

It is common practice to use Avrami’s approach to determine the recrystallized volume fraction [53–55]. The extended volume fraction is defined as the volume fraction of the recrystallized grains if *both* nucleation and growth were unaffected by the already recrystallized material, i.e. if new grains could nucleate in the recrystallized material and overlap each other upon growth. It is given by:

$$V_{ext}(t) = \int_0^t \dot{N}(t') V(t, t') dt' \quad (4.24)$$

Where $V(t, t')$ is the volume at time t of a single grain nucleated at time t' . Because their growth is constricted by the lines of primary aluminides, the grains are

System	M_0 ($\text{m}^4 \text{J}^{-1} \text{s}^{-1}$)	Q (kJ mol^{-1})	Q (eV)	source
Al - 0.01 Mn - $40^\circ \langle 111 \rangle$	3.0	96.4	1.0	[74]
Al - 0.01 Mn	3.0	106	1.1	[74]
Al - 0.1 Mn	2.71	136	1.41	[75]
Al - 0.1 Mn	75.33	168	1.74	[75]
Al - 0.3 Mn	0.09	135	1.40	[75]
HP Al - $28^\circ / \langle 100 \rangle$	2.2×10^{-3}	66	0.68	[73]
Al - 0.05 Si - $40^\circ / \langle 111 \rangle$	0.15	87	0.90	[73]
Al - 0.1 Mg - $40^\circ / \langle 111 \rangle$	3.16	136	1.41	[73]
Al - 1 Mg - $40^\circ / \langle 111 \rangle$	376	171	1.77	[73]
Al - 1 Mg	367	170	1.76	[73]
Al - 3 Mg	189	353	3.66	[73]
Al - 3 Mn - $40^\circ / \langle 111 \rangle$	3.7×10^7	212	2.20	[73]

Table 4.2: Measured mobilities in various low alloyed aluminium materials.

assumed to expand mostly in two dimensions. In rolled products, the aluminides are stacked in parallel (**RD**, **TD**) planes. Limiting the growth in the direction **ND** to a maximum height h (equation (4.2)), the grains end up having a cylindrical morphology.

Considering the experimental results, this approximation is fully justified at 300°C , and at 400°C in the deformation crosses. In between the deformation crosses, the grain boundaries impinge on each other before reaching the lines of aluminides. The approximation is kept however for two reasons:

- The computed grain radius is an equivalent radius to a cylinder of same volume. This calculation should override the effects of the cylindrical approximation.
- In cold rolled products, the level of strain achieved is well above 1.5. The planes of primary aluminides are separated by a short distance, which highly prevents growth in the direction of **ND**.

$V(t, t')$ is then given by:

$$V(t, t') = h\pi R_g^2(t, t') \quad (4.25)$$

Where $R_g(t, t')$ is the radius at time t of an individual grain nucleated at time t' , given by integration of \dot{R}_g over $[t', t]$:

$$R_g(t, t') = \int_{t'}^t \dot{R}_g(z) dz \quad (4.26)$$

Recrystallized fraction

The recrystallized fraction is calculated after equation (1.70):

$$\chi_{RX} = 1 - \exp(-V_{ext}) \quad (4.27)$$

Average grain radius

Because of the Avrami approach, so called “phantom” grains are able to nucleate within the recrystallized material. Therefore the nucleation rate was made independent of χ_{RX} . When calculating the average grain radius, one must however consider only the grains that nucleated in the untransformed material. During a time interval dt' , the real number of grains that nucleate is $(\chi_{RX}(t)) \dot{N}(t) dt'$. These grains grow to a radius $R_g(t)$ given by equation (4.26). The average grain radius $\langle R_g(t) \rangle$ is then given by integrating \dot{R}_g over the nucleation time and normalizing by the total number of recrystallized grains:

$$\langle R_g(t) \rangle = \frac{\int_0^t \dot{R}_g(t, t') (1 - \chi_{RX}(t')) \dot{N}(t') dt'}{\int_0^t (1 - \chi_{RX}(t')) \dot{N}(t') dt'} \quad (4.28)$$

Equation (4.28) actually gives the “extended” radius of the grains, i.e. the radius that they would have if they were able to overlap. This might lead to overestimate the actual grain radius.

4.2.2 Model implementation

The model was implemented in Matlab[®] using the parameters in table 4.3. The quadratures were made using Euler explicit methods with a time step of 0.01 to 1 s.

Variable	Value	Unit
b	0.286	μm
B	$\sqrt{3}/2$	-
h_0	85	μm
k_B	1.38×10^{-23}	J K^{-1}
K_i	0.01	-
l_0	680	μm
M_g^*	30	$\text{m}^4 \text{J}^{-1} \text{s}^{-1}$
M_{sg}^*	0.5*	$\text{m}^4 \text{J}^{-1} \text{s}^{-1}$
\dot{N}^*	$[4 \times 10^4 - 1 \times 10^5]^{**}$	s^{-1}
Q_{diff}	0.98	eV
Q_{mob}^g	1.6	eV
Q_{mob}^{sg}	1.6*	eV
Q_{nucl}	2.1	eV
w	431	μm
α	0.5	-
γ_g	0.324	J m^{-2}
μ	$(8.48 - 0.0406T)/(2(1 + \nu))$	GPa
ν	0.33	-
ν_D	1.5×10^{13}	s^{-1}
$\rho_{i,eq}$	2×10^{10}	m^{-2}
θ	3	$^\circ$
θ_c	11	$^\circ$

Table 4.3: Model parameters.

* Zurob *et al.* [76] use $M_{sg} = [0.2 - 0.02] M_g$.

** Two levels of strain have been investigated, which was not sufficient to investigate the strain dependency of N^* . The reported values are for $\epsilon = 1$ and $\epsilon = 1.5$, respectively.

4.3 Results

4.3.1 Non-isothermal

In a first approach, we assume that the samples are placed cold in an oven at the annealing temperature, and we use the temperature profiles in section 4.1.1.

The kinetics of recrystallization, namely the time evolution of the recrystallized fraction and that of the mean grain diameter, are presented in figure 4.7, for both regions of strain $\epsilon = 1$ and $\epsilon = 1.5$. The experimental measurements and the modelling results are displayed together at 300 °C and 400 °C. At 500 °C, only modelling results are available. Note that at 300 s and 400 °C, the microstructure is fully recrystallized for both strain grades. Also, after 1200 s, all the experimental points not visible on the plot are simply superimposed with the red dots.

The experimental and modelling results are in reasonable agreement. As expected, recrystallization is faster at higher temperatures. It is noticeable that the level of strain reached before annealing has a bigger effect on the recrystallization kinetics at 300 °C than at higher temperatures.

At 300 °C and $\epsilon = 1$, the model results differ from that of the experiments in two ways. First the predicted volume fraction after 1200 s of annealing is 25 % higher, and second the mean grain diameter at the same time is lower by roughly a factor 2. The final recrystallized fraction and grain radius are however well within the uncertainty of measurement. Moreover, the time of beginning of recrystallization is correctly captured by the model.

At 300 °C and $\epsilon = 1.5$, the calculations are off by roughly 600 s, i.e. 10 min, in predicting the time of 100 % recrystallization. The grain size is predicted accurately.

The difference in strain reflects in the results by offsetting the recrystallized fraction for 500 to 1000 s. The final grain radius shows a difference of about 10 μm .

At 400 °C and $\epsilon = 1$, the recrystallization kinetics are accurately predicted.

At 400 °C and $\epsilon = 1.5$, the time of beginning of recrystallization is off by about 50 s, but the final grain radius is correctly predicted.

Note that at 400 °C, there is almost no more dependency of the previous strain on the evolution of the recrystallized fraction, but the grain diameter is still appreciably affected (about 5 μm).

The same observation can be made at 500 °C. At that temperature, recrystallization happens well at the beginning of annealing, during heating.

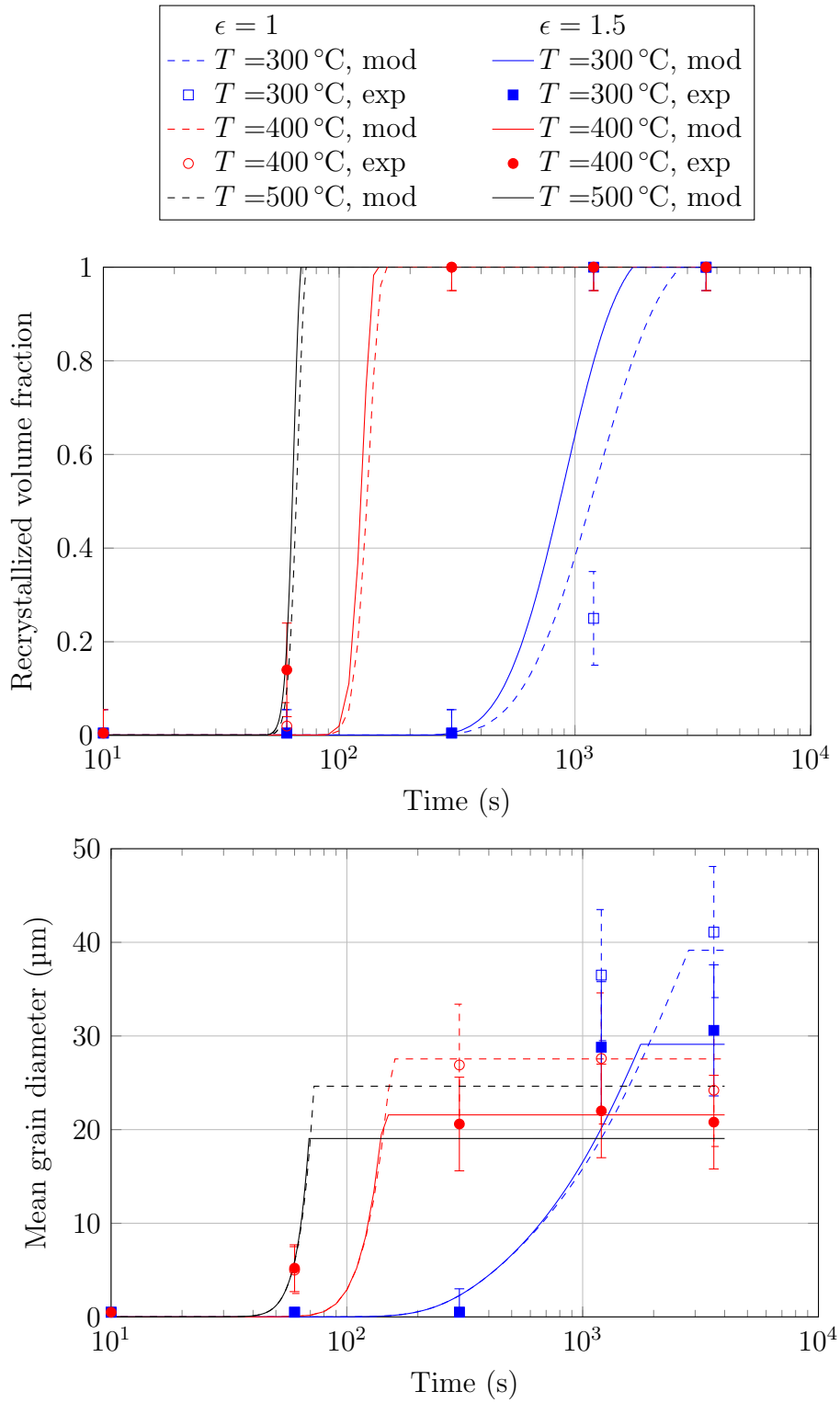


Figure 4.7: Modelled (mod) and experimental (exp) recrystallization kinetics.

When recrystallization is complete, the model does not predict further grain growth. This means that the particle pinning is strong enough to prevent grain boundary motion.

In addition, figures 4.8 and 4.9 show the evolution of ρ_i , δ , P and \dot{R}_g with time in the non recrystallized material. All curves stop when 100% recrystallization is reached, even P and \dot{R}_g , meaning that the particle drag is indeed strong enough to prevent grain growth.

Because of recovery, ρ_i decreases and δ increases, causing a drop in the driving pressure. The evolution of the kinetics is gradual because both recovery and static recrystallization are temperature activated phenomena. The sample temperature at the beginning of annealing being low, the kinetics are unaffected. As the temperature rises, recovery and recrystallization gradually occur. At 300 °C the evolution of \dot{R}_g shows a maximum at about 300 s. Initially, as the temperature increases, the grain growth rate increases accordingly. But as the temperature stabilizes, recovery rapidly takes over and \dot{R}_g starts decreasing. At 400 °C and 500 °C, the same trend can be observed but recrystallization stops before the maximum growth rate is achieved.

Figure 4.10 (top) shows the density of growth nuclei being created at each time step, in the yet non-recrystallized material. Nucleation being thermally activated, the density of nuclei increases as the sample temperature rises. All 6 curves display a maximum around the time where the sample temperature nears the oven temperature. Please be aware that those time evolutions are affected by the time step chosen for the simulations. Time step independent solutions can be obtained by plotting the number of nuclei per unit volume and per grain radius achieved, but they are much less intuitive to interpret and do not bring extra information.

Figure 4.10 (bottom) shows the grain radius achieved by growth nuclei nucleated at different times, during annealing at 300 °C for 100 s, 300 s, 1000 s and 3600 s. In every case, the earliest nucleated grains reach a near constant radius. When the nucleation time approaches the annealing time, the radius naturally drops towards 0 since the grains have very little time to grow. At the beginning of annealing, i.e 100 s, grains barely grow because the temperature is too low. After 100 s, the temperature is already high enough for individual grains to start growing. However figure 4.10 shows that the density of nuclei being nucleated within the first 100 s remains relatively low. Hence only the grains nucleated after 100 s effectively contribute to recrystallization. Same goes for further annealing for 1000 s and 3600 s.

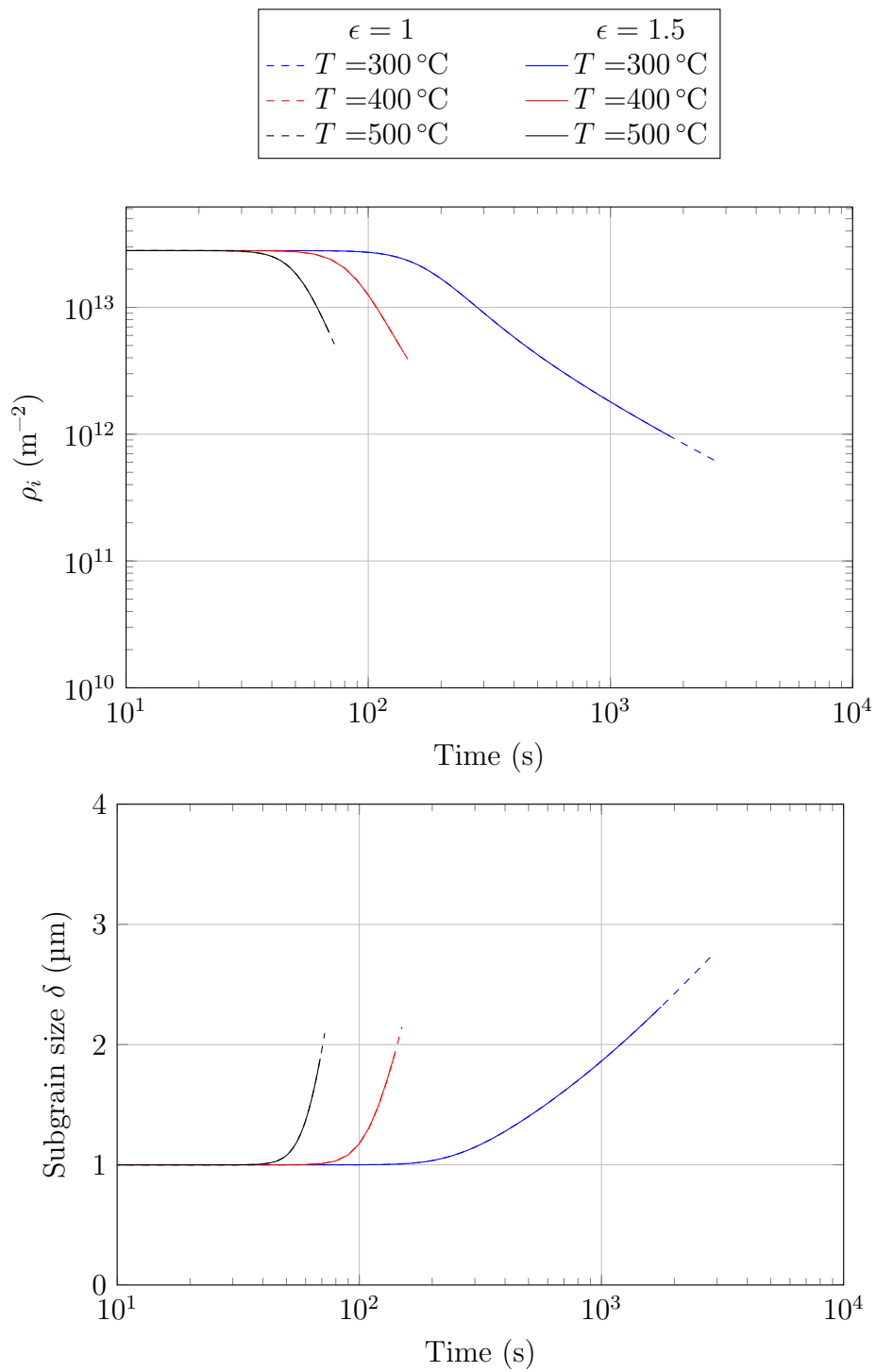


Figure 4.8: Modelled time evolution of ρ_i (top) and δ (bottom).

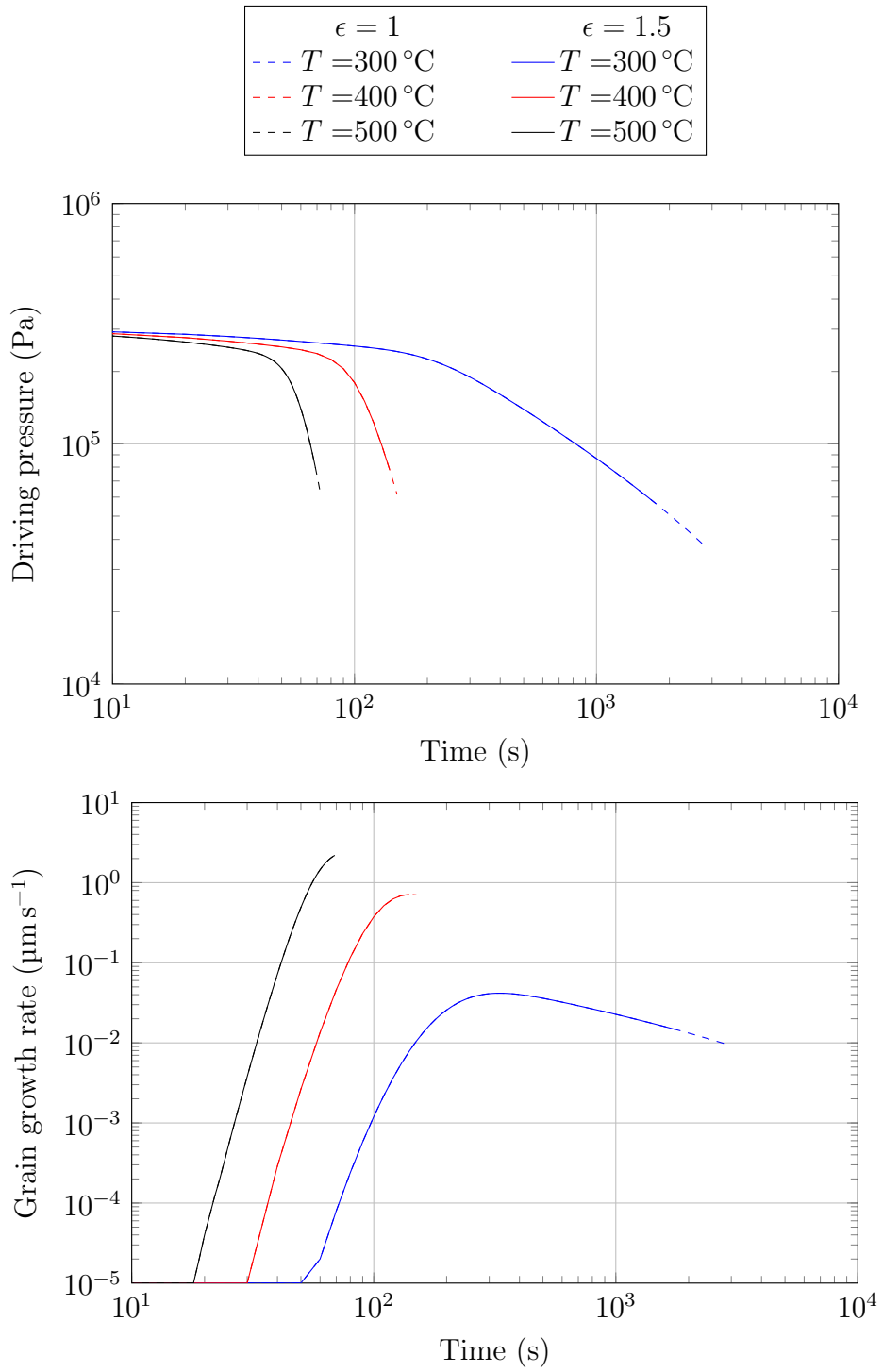


Figure 4.9: Time evolution of the driving pressure (top) and the grain growth rate (bottom).

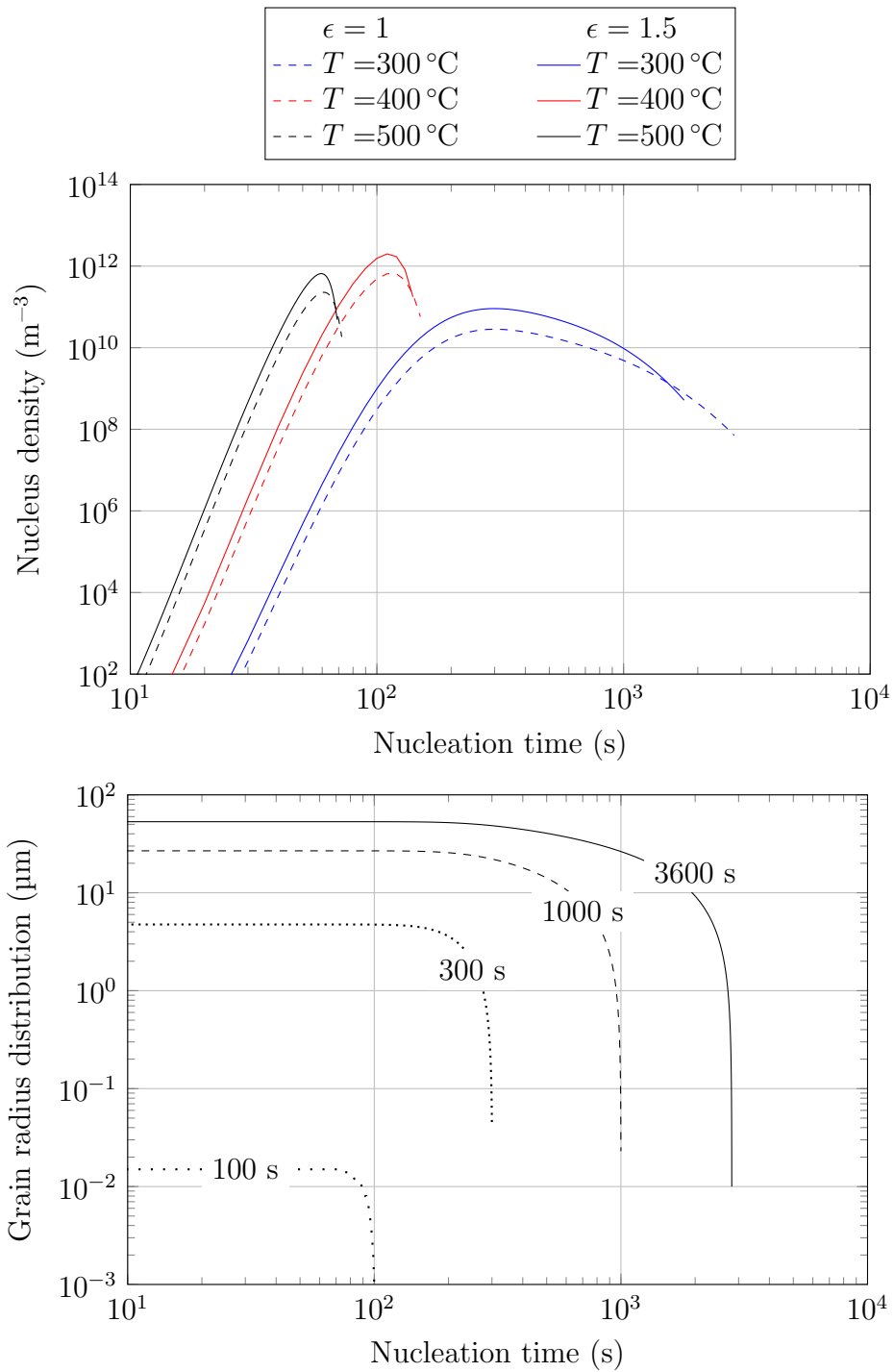


Figure 4.10: (top) volume density of growth nuclei being created at each time step ($dt = 1\text{s}$) and (bottom) radii of individual grains nucleated at each time step after holding at 300 °C for 100 s , 300 s , 1000 s and 3600 s ($\epsilon = 1$).

4.3.2 Isothermal

After calibration, the model was run with a constant sample temperature. Figure 4.11 compares the recrystallization kinetics in isothermal (I) condition to the recrystallization kinetics obtained in non-isothermal (NI) condition.

At 300 °C, the kinetics are almost unaffected. Recrystallization starts 200 s earlier than in the NI case, but ends only a couple of seconds earlier. The kinetics are slightly shifted, and the grain size is not affected in an appreciable way.

At 400 °C and 500 °C however, recrystallization is strongly accelerated by the change from non-isothermal to isothermal annealing. The kinetics of the reaction are accelerated by 2 orders of magnitude and more in the isothermal condition. The grain diameter is decreased by about 30 – 40 % (5–10 μm).

Comprehensively, under isothermal condition, new grains are created and start growing from the beginning of annealing because the temperature is sufficient to promote atomic diffusion. The driving pressure is readily at its maximum, since no recovery has occurred yet. The nucleation rate, given by equation (4.11), benefits from the maximum possible pressure and temperature, assuring that nuclei are formed very quickly.

The grain growth rate, given by equation (4.22), is plotted in figure 4.12. It also benefits from an early maximum pressure, ensuring that the new recrystallized grains start growing immediately and relatively fast. This impacts greatly the kinetics at 400 °C and 500 °C because relatively high growth rates are achieved very early. Figure 4.12 shows that the growth rates at those temperatures is at least one order of magnitude higher than the maximum growth rate achieved in the non-isothermal case. It also shows that the growth rate is maximum from the beginning. Recrystallization even stops (reaches 100 %) before recovery has time to consequently impact the growth rate.

At 300 °C however, even though a maximum growth rate is achieved early, it remains too low to consequently impact the overall kinetics. Figure 4.12 shows that the growth rate in isothermal condition is in the same order of magnitude as the maximum growth rate achieved in the non-isothermal case. Thus, the kinetics of recrystallization are only slightly affected.

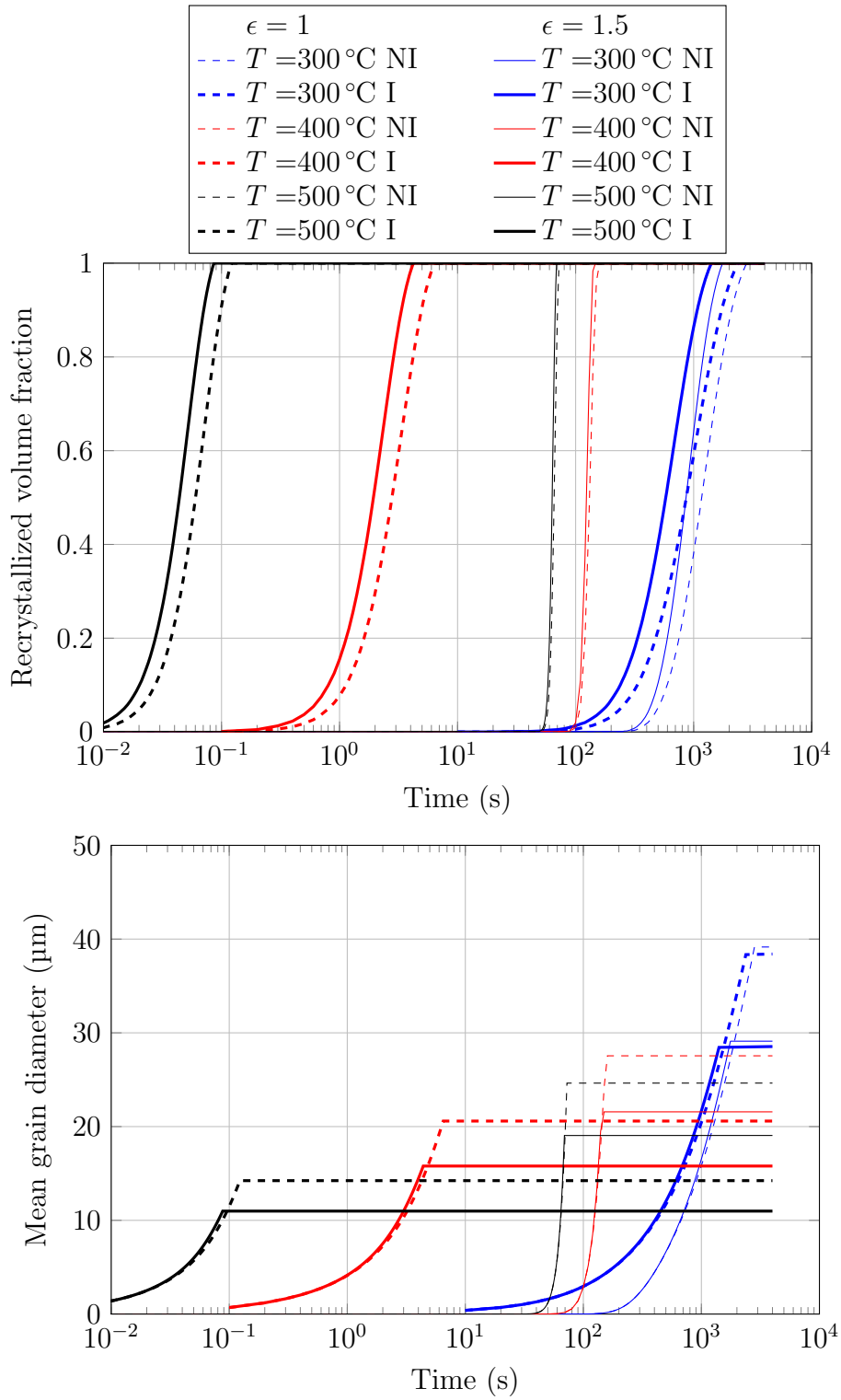


Figure 4.11: Recrystallization kinetics under isothermal (I, thick curves) and non-isothermal (NI, thin curves) conditions.

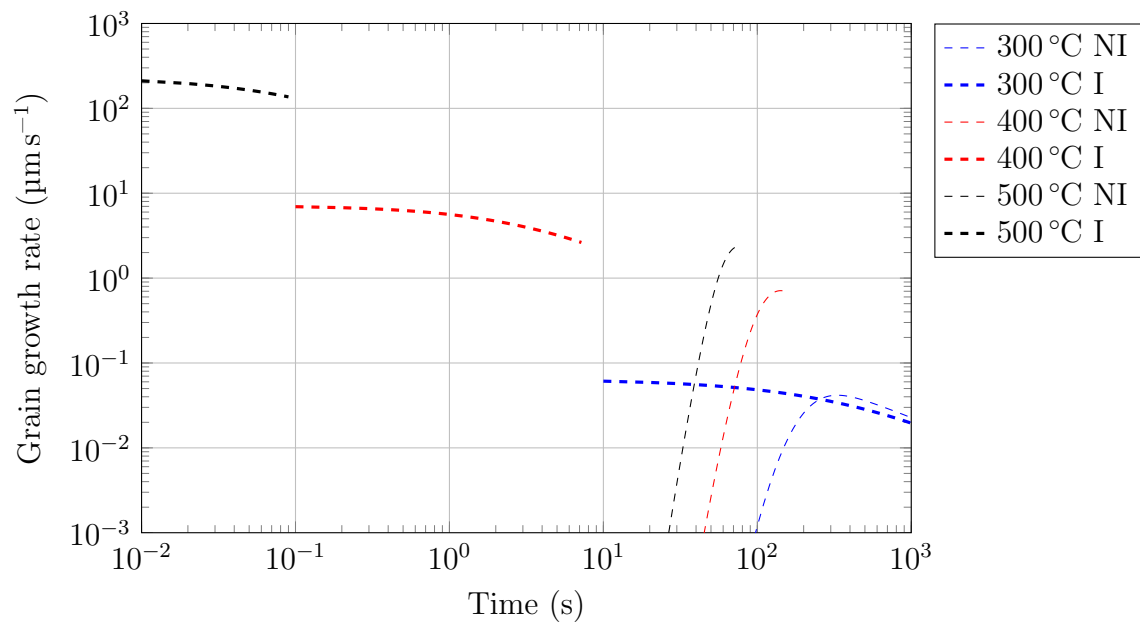


Figure 4.12: Grain growth rate during isothermal (thick) and non isothermal (thin) annealing ($\epsilon = 1$).

Chapter 5

Finite element simulations

Plane strain compression, multipass rolling and annealing were modelled by means of finite elements in the commercial code DEFORM2DTM. The objective of this part was to model the strain hardening during a mutlipass cold rolling operation, and then to calculate the grain size evolution during subsequent solution annealing. Because of the symmetry of the processes considered, all problems were set in 2D with a plane strain symmetry.

The DEFORMTM system comes with a set of customizable subroutines that allow the users to implement their own bit of code. The subroutines, called on the run, can be used to update some microstructural variables at every FE node or element, like the dislocation densities and the fraction of recrystallized material. The flow stress of the material can be computed in a dedicated routine that has access to all the user defined variables. Figure 5.1 shows the connections between the FEM engine and the subroutines.

In all the simulations, the mesh was generated automatically by DEFORM2DTM. Only an approximate total number of elements is required, as well as the number of elements in the thickness of the workpiece. In plane strain conditions, the elements are rectangular by default.

The finite element engine computes the temperature T , strain ϵ and strain rate $\dot{\epsilon}$ at the current step, and sends them along with the time step dt and the microscopic variables ξ at current time t to the microstructure routine. This routine, implemented by the user, updates ξ at time $t + dt$, and sends it back to the FEM engine or to the stress routine. The latter, if involved, calculates the flow stress σ at every node/element and sends all the data back to the FEM engine.

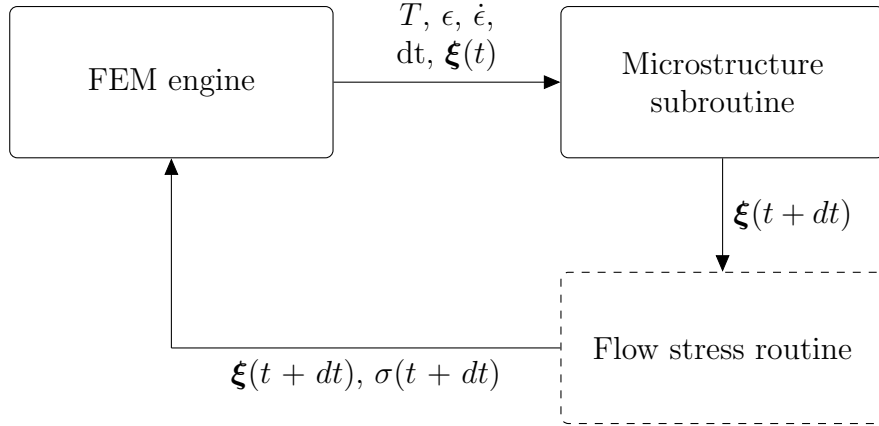


Figure 5.1: Structure of the microstructure and flow stress model implementations in DEFORM2D[®]. The Flow stress routine can be ignored if there is no deformation.

5.1 Implementation of the flow stress model

The flow stress model in chapter 3 was implemented and used to predict the microstructure evolution during plane strain compression. It was then applied to multiple industrial rolling operations.

5.1.1 Generalities about flow rules

The deformed material is always assumed to be rigid plastic. This means that all the strain that the material is subjected to is of plastic nature. The material was considered isotropic; the Levy-Mises flow rule applies. It relates the components of the stress tensor σ_{ij} to those of the strain rate tensor $\dot{\epsilon}_{ij}$ as follows:

$$\sigma_{ij} = \frac{1}{\dot{\lambda}} \dot{\epsilon}_{ij} \quad (5.1)$$

The proportionality parameter $\dot{\lambda}$ is determined from the flow stress σ of the material:

$$\dot{\lambda} = \frac{2}{3} \frac{\dot{\epsilon}}{\sigma} \quad (5.2)$$

$\dot{\varepsilon}$ being the equivalent strain rate. σ can either be provided by experimental investigations, or by the flow stress subroutine.

5.1.2 Plane strain compression

The plain strain geometry is a 2D replica of the test geometry in the Gleeble[®] 3800 experiments (figure 2.1) in the (RD, ND) plane (figure 2.1).

Coefficient of friction

Frictionless experiments would generate a homogeneous deformation. The deformation crosses observed experimentally in figure 2.4 are a consequence of friction between the tools and the sample. The samples deformed at room temperature often display an asymmetrical geometry, as showed in figure 5.2. This lack of symmetry is a clear indicator of a non-uniform friction between the tools and the sample.

In his master thesis, P. Loidolt [63] investigated the influence of an heterogeneous distribution of friction between the anvils and the sample by means of finite element analysis combined with an experimental investigation. The following conclusions were drawn:

- The measurements of the flow stress are overestimated if friction is omitted, thus the measured flow curves must be corrected for friction.
- The asymmetrical flow can be caused either by a non uniform friction distribution on the surface of the sample, due to bad lubrication for example, or to a misalignment of the anvils. The latter case is a methodology problem that was checked thoroughly.
- The comparison between the experimental sample geometry after deformation and the geometry predicted by the simulations showed that a shear friction coefficient of 0.02 was best suited for the simulations.

Simulation set-up

The dies are considered rigid, i.e. they are made of a hard material and their elastic deformation is negligible. The top anvil is mobile, while the bottom anvil does not move. The top anvil velocity v_{anvil} is obtained by differentiating equation (2.1) (see figure 5.3):

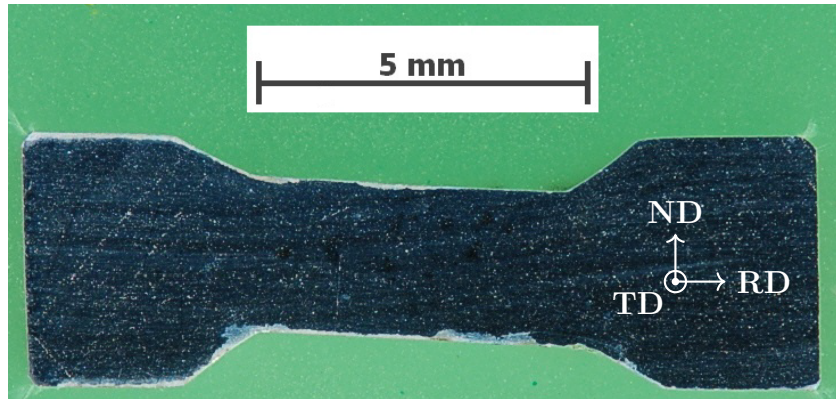


Figure 5.2: Cross section of a sample cold deformed in plain strain compression. The asymmetry indicates non homogeneous frictional effects.

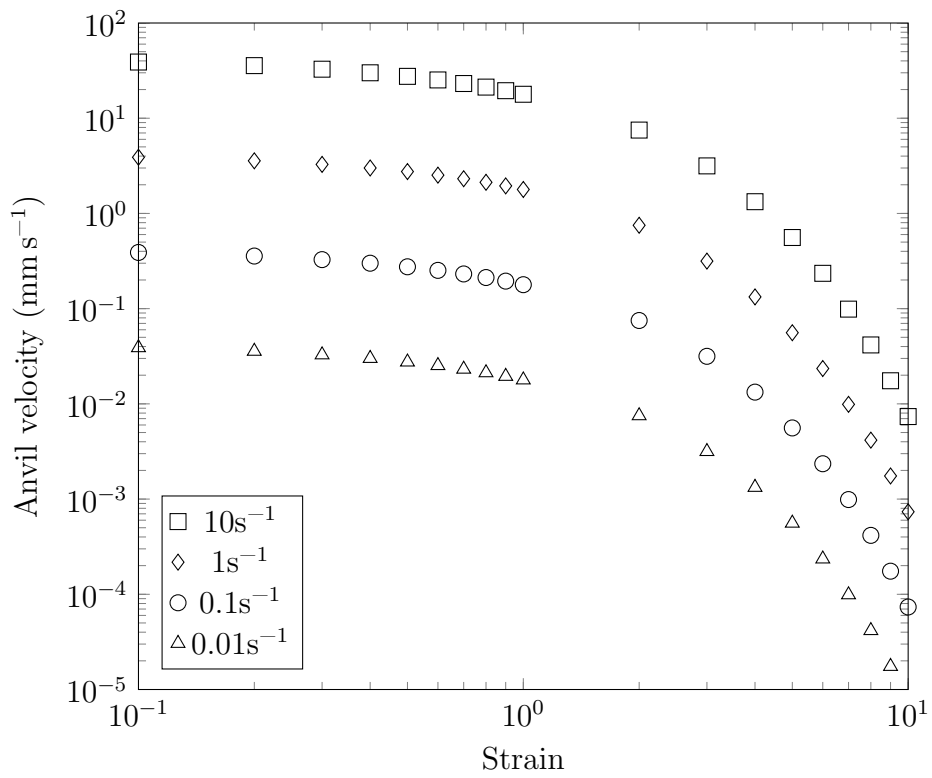


Figure 5.3: Anvil velocity as a function of strain, after equation (5.3) and for several strain rates.

$$v_{anvil} = \frac{\sqrt{3}}{2} h_0^s \exp\left(\frac{\sqrt{3}}{2} \dot{\bar{\epsilon}} t\right) \dot{\bar{\epsilon}} \quad (5.3)$$

The surface of the sample was made permeable to heat. The heat transfer coefficient with the anvils was $\text{N s}^{-1} \text{mm}^{-1} \text{K}^{-1}$ and the convection coefficient in air was $0.02 \text{ N s}^{-1} \text{mm}^{-1} \text{K}^{-1}$. The mesh had 504 elements, 12 in the thickness and 42 in the rolling direction. Remeshing was prohibited during deformation to avoid any loss of information regarding the internal variables calculated in the microstructure subroutine.

Simulation results

The simulation results of deformation at room temperature and $\dot{\epsilon} = 10 \text{ s}^{-1}$ are shown in figure 5.4. The effective strain $\bar{\epsilon}$ is defined from the coefficients of the strain tensor ϵ_{ij} as:

$$\bar{\epsilon} = \sqrt{\frac{2}{3} \sum_{i,j} \epsilon_{ij}^2} \quad (5.4)$$

After deformation to a macroscopic strain of 1, the effective strain distribution displays two deformation crosses, as observed experimentally in figure 2.4a). The true macroscopic strain of 1 is reached in between the deformation crosses. In the centre of the crosses, the strain reaches a value of 1.5.

The flow stress is calculated by the flow subroutine and is equated to the von Mises stress of the material. It raises to a maximum of 230 MPa in the deformation zone (figure 2.4b)).

The model predicts a homogeneous saturation of the cell interior dislocation density, while the wall dislocation density has the same distribution pattern as the effective strain, showing that the wall dislocation density keeps increasing with strain.

The asymmetry observed in the results, on the edges of the deformation zone, are simulation errors arising from a mesh distortion.

The subgrain size, given by equation (3.22), varies inversely proportional to ρ_w . Therefore, δ is expected to be smaller within the deformation crosses, and the stored energy higher.

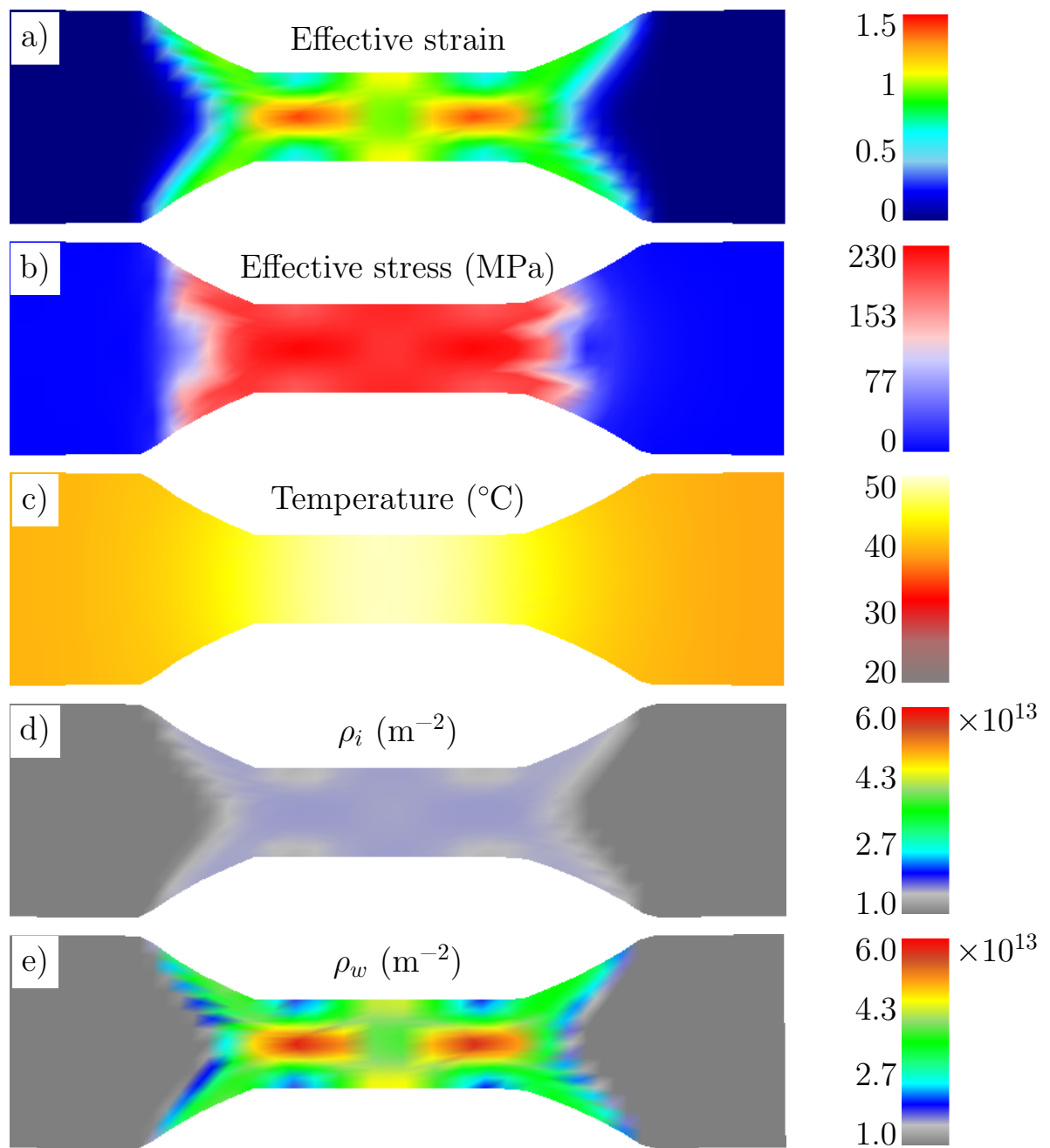


Figure 5.4: FEM simulation of the plane strain compression tests.

5.1.3 Multi-pass rolling

The rolling simulations were ran with only one roll and half the plate, since the behaviour of the other half is assumed to be symmetrical (figure 5.5). As such, a boundary condition was inserted on in the middle plane to fix its vertical velocity to 0. A pusher was used at the beginning to force the plate under the roll, until friction alone was enough to drag the plate forward. The geometry specifics were provided by the company AMAG Austria Metall to match the production process.

The roll was rigid, made of a stainless steel A-286. The material thermal data was taken from the DEFORMTM material database. The roll diameter was fixed at 430 mm and its angular velocity at 35 rads⁻¹.

In order to limit the computation time, the length of the plate was reduced to 200 mm (the initial plate thickness being approximately 10 mm thick). The initial mesh was made of roughly 4000 elements, with 8 elements in the thickness. Heat exchange was enabled on the whole outer surface of the plate. A constant heat exchange coefficient of 11 W m⁻² K⁻¹, recommended by DEFORM2DTM, was applied between the roll and the plate. The environment temperature was fixed at 20 °C with a convection coefficient of 0.2 N s⁻¹ mm⁻¹ K⁻¹, i.e. 10 times the standard value for air [77] in order to account for the wind created by the plate displacement.

A Coulomb coefficient μ_f was applied between the roll and the plate. Its influence on the strain rate in the plate was previously investigated (figure 5.6). A stick-slip situation gives birth to instabilities in the strain rate profile when $\mu_f < 0.3$. In the range 0.3 – 0.6, the plate still slips right after the entry points. Above 0.6, the plate sticks to the roll.

A unidirectional rolling schedules of 6 passes of cold deformation was simulated (table 5.1). A time lapse of 2 min was inserted between the passes for the material to cool down. Indeed, the material exiting the rolls does not come back between them before all the remaining plate is deformed and repositioned, which leaves some time for recovery to occur.

Figure 5.7 shows the results of the simulation in the 6th pass. The strain accumulates preferentially on the edge of the plate. Accordingly, the wall dislocation density is higher on the edge than in the centre of the plate. The internal dislocation density saturates and remains constant in the plate. Overall, the temperature does not increase over 100 °C.

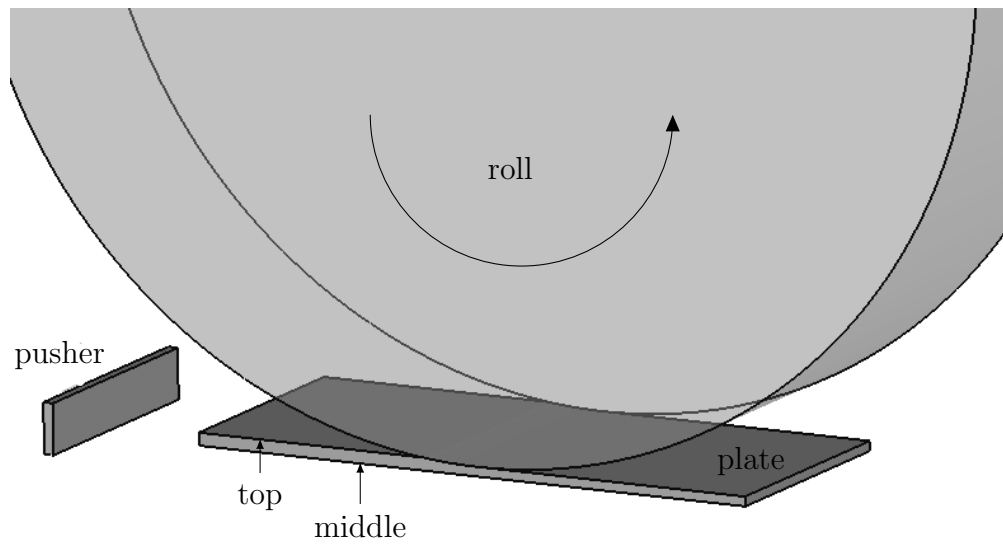


Figure 5.5: Rolling geometry. The plate is initially pushed under the roll by the pusher. The middle plane of the plate is a symmetry plane, thus only the top half of the process is simulated.

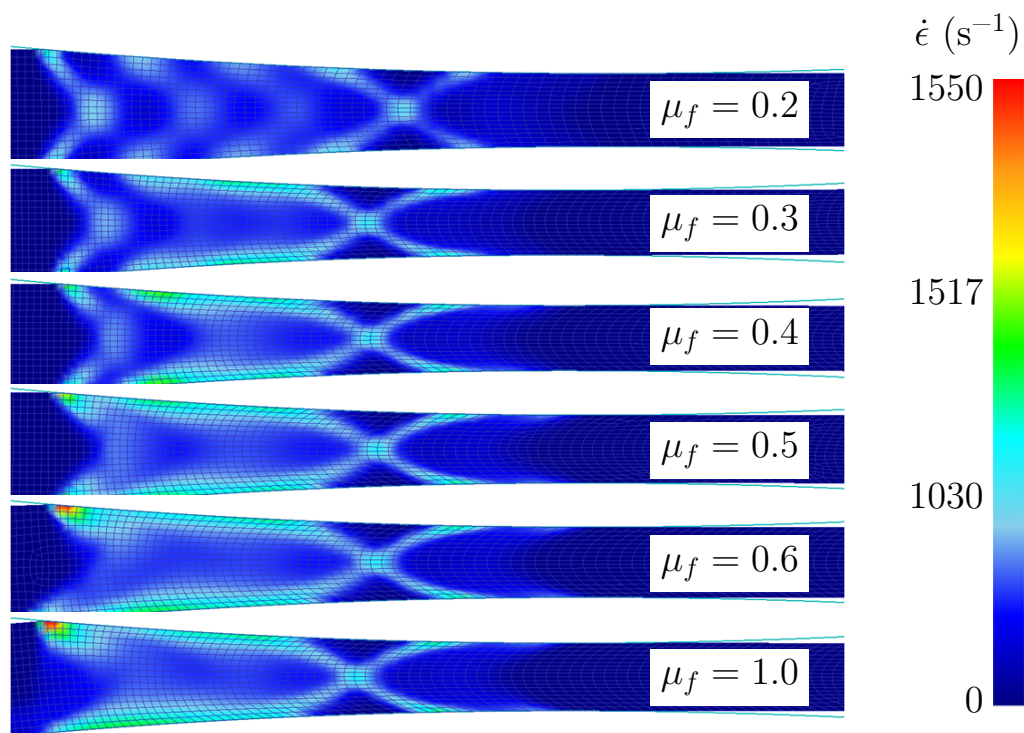


Figure 5.6: Influence of the friction coefficient μ_f on the strain rate in the plate.

Pass	Initial height	Thickness reduction
1	10	2.5
2	7.5	2.0
3	5.5	1.5
4	4.0	1.0
5	3.0	0.5
6	2.5	0.5

Table 5.1: Rolling schedule A. All heights are in mm.

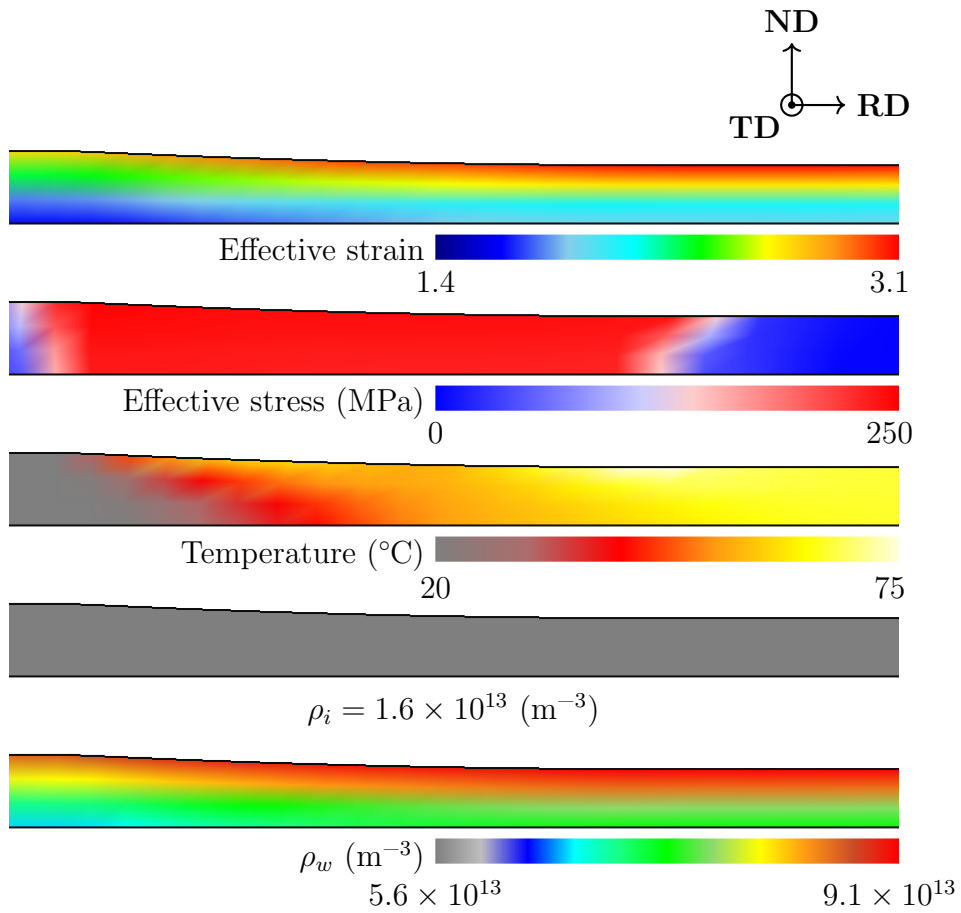


Figure 5.7: Cold rolling simulation, pass 6.

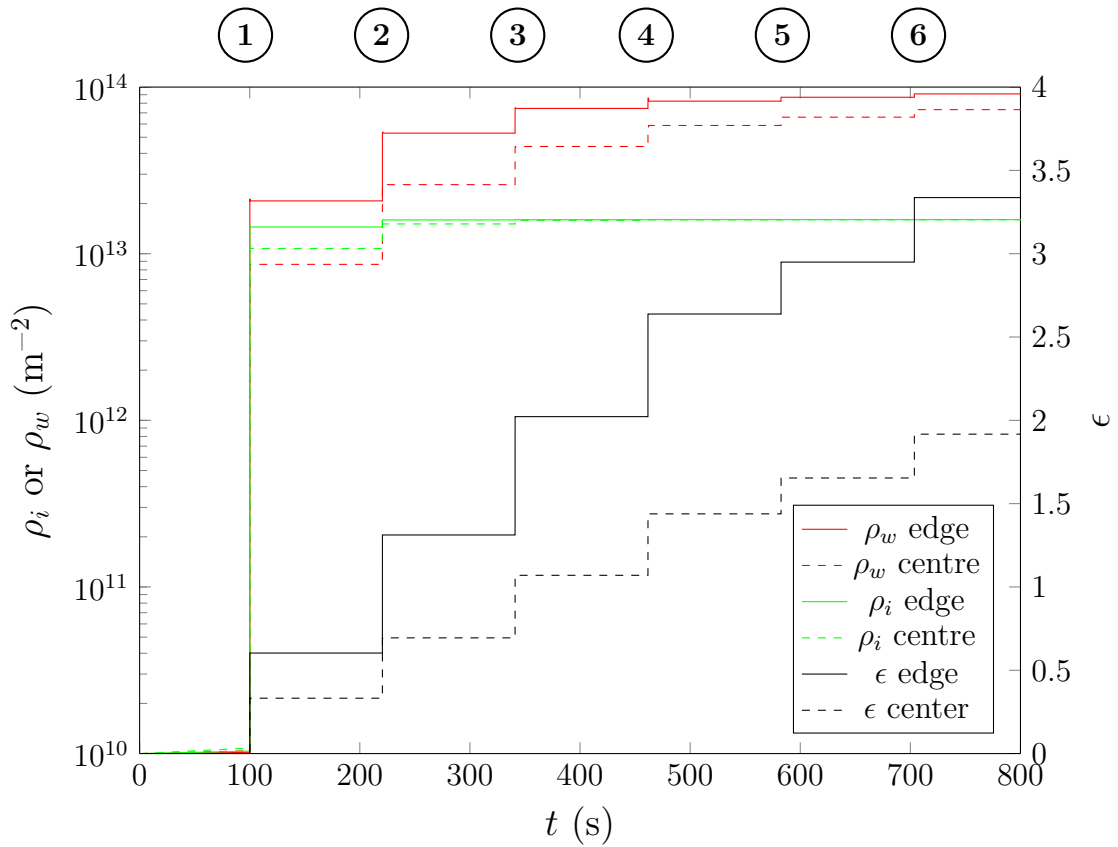


Figure 5.8: Strain and dislocation evolution during multipass cold rolling. The position of the passes are indicated in bold.

Figure 5.8 shows the evolution of the strain and the dislocation densities with time, in the centre and near the surface of the plate. The pass numbers are indicated in bold. At every pass, the strain increases very fast, and so do the dislocation densities. The strain increases more at the surface than in the centre of the plate. ρ_i saturates after two passes in the whole plate. ρ_w , however, keeps increasing at every pass, albeit less and less every time. The subgrain size is inversely proportional to ρ_w . It is therefore expected to decrease as one travels from the center of the plate towards the surface.

5.2 Implementation of the recrystallization model

One of the drawbacks of the DEFORMTM subroutines is that the stored microscopic variables must be scalar, i.e. DEFORMTM does not provide any solution for passing arrays between the FEM engine and the subroutines.

The calculation of the average grain growth as formulated in equation (4.28) requires to recall the whole nucleation history because the nucleation rate is not constant. Because DEFORM does not work with arrays, it is not possible to save the number of nuclei being formed at every time step, and the recrystallization model as formulated in chapter 4 cannot be implemented. What can be done, is to implement a simplified version of the recrystallization model.

5.2.1 Simplified recrystallization model

The objective of this section is to find a nucleation criterion in order to calculate the grain size evolution during annealing of the plate after cold deformation. Consider the volume density of nuclei N being formed during the process. It reads:

$$N = N^* \exp(\epsilon) \exp\left(\frac{-Q_{nucl}}{k_B T_a}\right) \quad (5.5)$$

Where N^* is a model constant and T_a is the annealing temperature. If the latter is high enough, all new grains are quickly formed at the beginning of the process, before recovery discards any possibility of bulging. Let us call t_0 the time at which no more nucleation event can occur. If t_0 is small enough, no consequent growth occurs before that time, and the average grain size is simply given by equation (4.28) where τ is replaced by t_0 :

$$\langle R \rangle (t_0, t) = \int_{t_0}^t \dot{R}(z) dz \quad (5.6)$$

With that model, there is no need to store any large array of information over the whole simulation, since R , and consequently the recrystallized volume fraction, are not any more a function of the nucleation rate.

5.2.2 Annealing of samples deformed in plane strain compression

The samples deformed in plain strain compression were annealed at 300 °C and 400 °C. The corresponding temperature profiles are given in section 4.1.1. After one hour, the whole microstructure is recrystallized. The grain size prediction are shown in figure 5.9. The results show a good agreement with the grain size observed experimentally (figures 4.3 and 4.4). The model also displays the observed grain refinement with increasing strain and annealing temperature, which validates the nucleation criterion in terms of predictability.

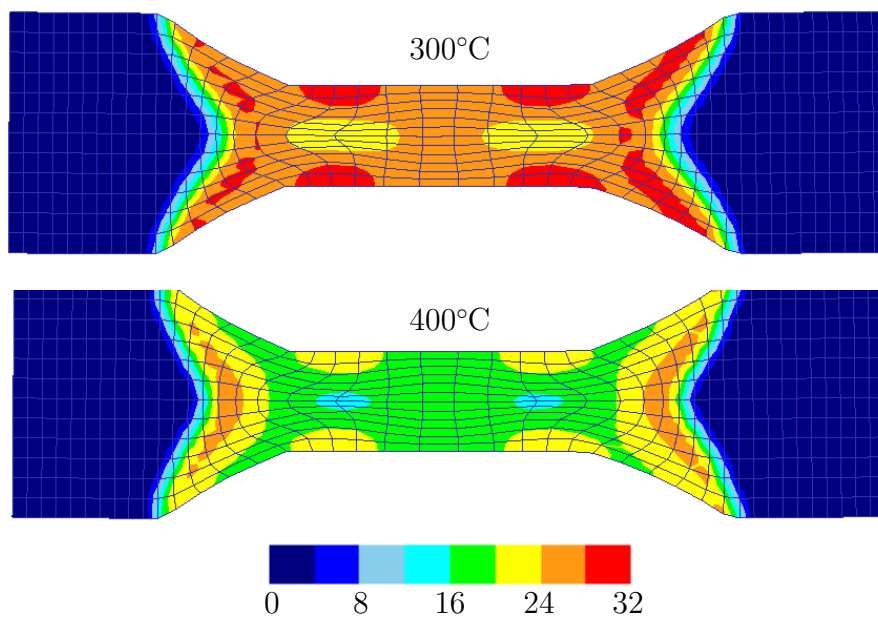


Figure 5.9: Average grain radius prediction after annealing one hour at 300 °C and 400 °C, in μm .

5.2.3 Solution annealing after rolling

The simplified model can be used to calculate the recrystallized fraction and the grain size after annealing of the deformed microstructures from rolling. The plate was deformed according to the rolling schedules A in table 5.1 and B in table 5.2. After rolling, a solution annealing step is used to dissolve the $\beta\text{-Mg}_2\text{Si}$ particles. Solution annealing of 6xxx aluminium alloys is carried out in the range of 500 to 600 °C. A coil of cold deformed material is uncoiled and continuously driven

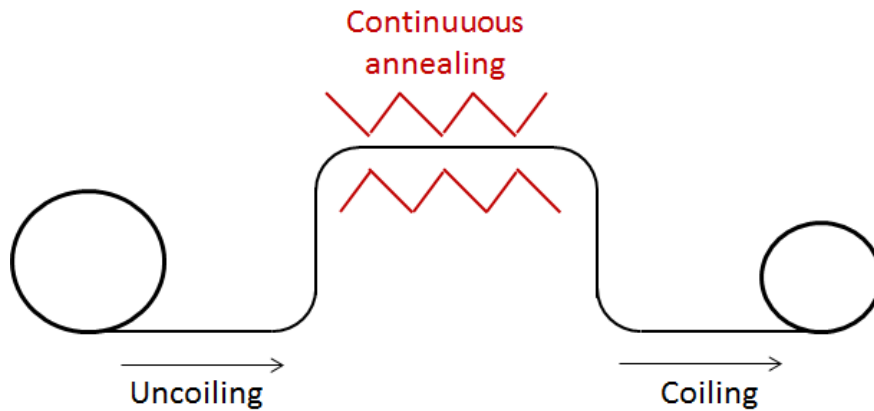


Figure 5.10: Continuous solution annealing. The plate is uncoiled, annealed, quenched and coiled.

into an oven at a speed of 2 m s^{-1} , where the material recrystallizes and some of the second phase particles dissolve. At the exit of the oven, the material is water quenched. The whole annealing process takes about 200 s. As the temperature is higher than in our experiments, the nucleation time is expected to be shortened and the model accuracy increased. Figure 5.11 shows the predicted grain size after solution annealing at $550 \text{ }^\circ\text{C}$ for 200 s. Note that no account is taken of the dissolution of the $\beta\text{-Mg}_2\text{Si}$ here. As discussed in chapter 4, those particles are not distributed in a way that they effectively hinder the grain growth. The smaller FeMnSi aluminides, homogeneously distributed, are much more efficient at slowing down the grain boundary migration. The bigger FeMnSi aluminides, aligned on the previous grain boundaries, effectively stop the boundary migration. Only the $\beta\text{-Mg}_2\text{Si}$ dissolve during the solution annealing, but they are not expected to have an appreciable effect on the recrystallization kinetics.

The model predicts full recrystallization after both cold rolling schedules. The grain radius lies in both cases between 5 and $10 \text{ }\mu\text{m}$, increasing from the surface towards the center of the plate, following the gradient of strain. This is consistent with the tendency observed in chapter 4, where the grain size varies inversely with the annealing temperature, in the presence of a strong grain boundary pinning. The grain radius dispersion is narrower after the rolling schedule A (from 6.4 to $8 \text{ }\mu\text{m}$) than after the rolling schedule B (from 6 to $10 \text{ }\mu\text{m}$).

Pass	Initial height	Thickness reduction
1	8.0	2.0
2	6.0	1.5
3	4.5	1.0
4	3.5	0.5
5	3.0	0.5
6	2.5	0.5

Table 5.2: Rolling schedule B. All heights are in mm.

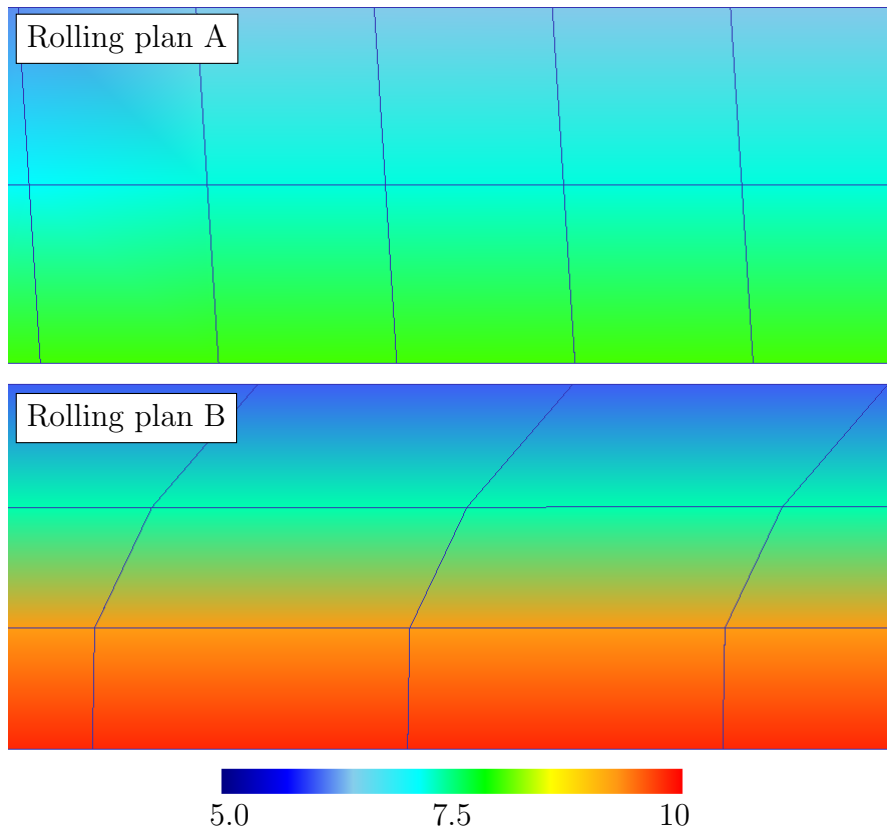


Figure 5.11: Grain radius prediction after solution annealing 20 s at 550°C, in μm .

Chapter 6

Additional Discussion

6.1 Deformation behaviour

The dislocation rate parameters are plotted against the temperature in figure 6.1. The strain rate corrections provided by equations (3.20) and (3.21) allow for $h_{1,x}$ and $h_{2,x}$ ($x = i, w$) to be independent of $\dot{\epsilon}$.

Except for $h_{2,w}$, all the parameters display the same behaviour in that they remain similar until 150°C and then start varying, i.e. the $h_{1,x}$ ($x = i, w$) strongly decrease and $h_{2,i}$ strongly increases. This is due to the fact that the flow curves at low deformation temperatures all display the same pattern and fall within a range of maximum 50 MPa from each other. The temperature variation in the model is sufficient to capture this behaviour without further need to act on the parameters. The decrease of $h_{1,i}$ with the temperature indicates that the storage of dislocations becomes less effective when the temperature increases, i.e. that the mobile dislocations travel a longer distance before being immobilized, reflecting an improved capacity for bypassing local obstacles when the temperature increases. The results also indicate that the hardening due to subgrain formation is promoted at lower temperatures since $h_{1,w}$ decreases with increasing temperatures also. As expected, $h_{2,i}$ increases with the temperature, meaning that dynamic recovery of cell interior dislocations is promoted. Interestingly, $h_{2,w}$ does not depend on the temperature. This seems to indicate that the wall dislocations, being already arranged in a configuration of low energy, are not appreciably affected by dynamic climb.

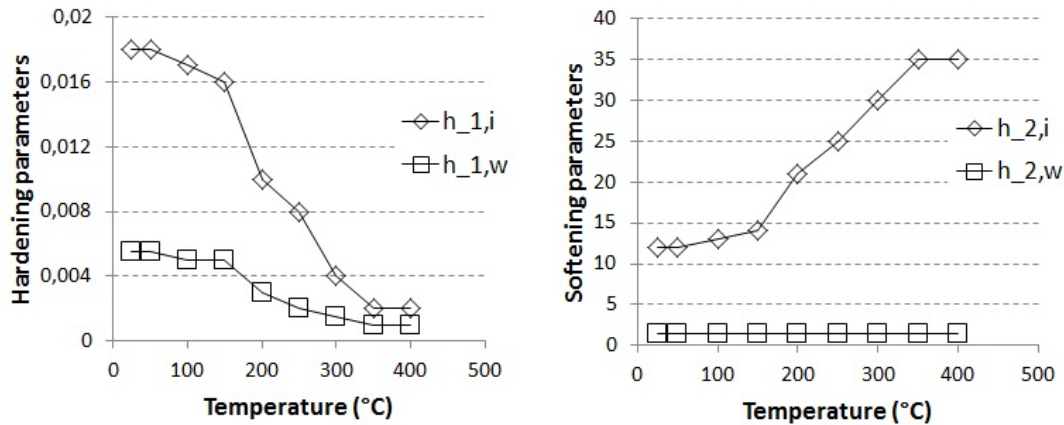


Figure 6.1: Hardening and softening parameters as a function of the temperature.

6.2 Recrystallization behaviour

The evolution of grain size after recrystallization in samples deformed by plane strain compression can be explained as follows. As the critical bulge size for Strain Induced Boundary Migration has an inverse relationship to the stored energy of deformation (equation (1.66)), more grains are able to nucleate in the middle of the deformation crosses, where the accumulated strain is larger, than in regions of lower strain. The new grains impinge on each other upon growth and limit the grain size in the deformation crosses.

Furthermore, the recrystallized grains are elongated in the direction of deformation. This is especially obvious during annealing at 300 °C (figure 4.3) between the deformation crosses, where the grain growth in the transverse direction is severely limited in comparison to the rolling direction (figure 4.3). It has been seen that the bigger aluminides are aligned in the direction of deformation (figure 2.7). In those regions where the particles are, their radius remains the same but their volume fraction increases drastically. The pinning effect on the moving boundaries increases accordingly, enough to stop them. At higher strain grades and annealing temperatures, surely the same trend would be observed if the grains did not impinge on each other before reaching the bigger aluminides. The small aluminides, homogeneously distributed, might still slow down the boundary migration but cannot completely pin the grain boundaries during recrystallization.

Within the time frame of the measurements, the grain size appears to be stabilized. As grain growth after recrystallization is driven only by capillarity effects, the

pressure on the boundaries is much lower than during recrystallization. Pinning by the homogeneously distributed smaller aluminides can then effectively counter balance this pressure and prevent any further boundary movement.

Above 350 °C, the Mg₂Si phase dissolves [78]. It however does not affect the recrystallization kinetics here, because the Mg₂Si particles are too coarse and too widely spaced to effectively pin the boundaries to begin with. The effects of the finely dispersed aluminides and of the lines of coarse aluminides are dominant.

It was mentioned in section 4.2.1 that the calculated average grain radius should be overestimated because it represents the radius of overlapping grains. However, the model parameters were chosen to favor the accuracy of the grain sizes over that of the recrystallization grades. The most critical parameter in determining the final grain size appeared to be density of nuclei. The more grains nucleate, the less space they have to grow and the lower is the final grain size. By slightly increasing the density of nuclei being created — through the parameters χ_b or Q_{nucl} — the predicted grain radius can be decreased to match the experimental measurements. In doing so the recrystallization grade becomes overestimated and 100 % recrystallization is reached at earlier times.

6.3 Modelling: further considerations

The measured yield stress of the material in figure 3.2, displays two distinct behaviours. Under 100 °C, $\hat{\sigma}_Y$ remains strain rate and temperature independent, whereas above 100 °C it becomes moderately strain rate dependent and strongly temperature dependent.

Overcoming obstacles to the dislocation motion is a thermally activated process (section 1.3), and the effective stress τ_{eff} needed to bypass the obstacles is temperature and strain rate dependent (section 1.3.6).

The obstacle approach shows good results at moderate to high temperatures, but seems ill advised at low deformation temperatures, since the measurements of the yield and the flow stress reported in figures 3.2 and 3.4 show almost no dependency to $\dot{\epsilon}$ and T under 100 °C. In the flow stress model presented in chapter 4, τ_{eff} was fixed at its value at 100 °C for low temperature deformation. This is however not physically supported.

In a first attempt to model the yield stress saturation at low temperature, we considered that τ_{eff} as defined in equation (1.35) was limited by the condition:

$$Q_{act} - \tau_{eff}V_{act} = 0 \quad \Longleftrightarrow \quad \tau_{eff} = \frac{Q_{act}}{V_{act}} \quad (6.1)$$

From equation (1.37), and since the temperature is not absolute zero, it comes:

$$\frac{M\dot{\epsilon}}{\rho_m b d \nu_{att}} = 1 \quad (6.2)$$

Taking $d = \rho^{-0.5}$ for values of ρ in the range $[10^9; 10^{12}]$, and strain rates between $0.1 - 10 \text{ s}^{-1}$, ρ_m falls in the range $10^{-1} - 10^5 \text{ m}^{-2}$. [9, 14] report much higher values of ρ_m m, in the order of $10^{10} - 10^{16} \text{ m}^{-2}$. Thus, this method cannot be retained.

In a second approach, it was considered that the obstacles to dislocation motion are the forest dislocations intersecting the slip plane. The mobile dislocations cut through the forest dislocations by forming jogs, therefore they increase the energy of the material by the energy of jog formation $E_j \approx 0.2\mu b^3$ [5]. The formation of jogs gives birth to an attractive force between the intersecting dislocations.

The force F per unit line required to move a dislocation is defined as the work done when a unit length of dislocation moves a unit distance b . If τ^* is the stress acting on the dislocation, $F = \tau^*b$. The work that needs to be done to move a dislocation segment of length λ on a unit distance b is therefore equal to $\tau^*b^2\lambda$.

In the absence of thermal activation, the work that needs to be done to break a mobile dislocation free of the attractive force of the jog is equal to E_j . It comes that:

$$\tau^* \approx 0.2 \frac{\mu b}{\lambda} \quad (6.3)$$

If the length of the dislocation segment that is affected by a single jog is the spacing between two forest dislocations, then λ is given by:

$$\lambda = C_\lambda \rho^{-0.5} \quad (6.4)$$

Where C_λ is a proportionality constant, and:

$$\tau^* = \frac{\mu b}{5C_\lambda} \sqrt{\rho} \quad (6.5)$$

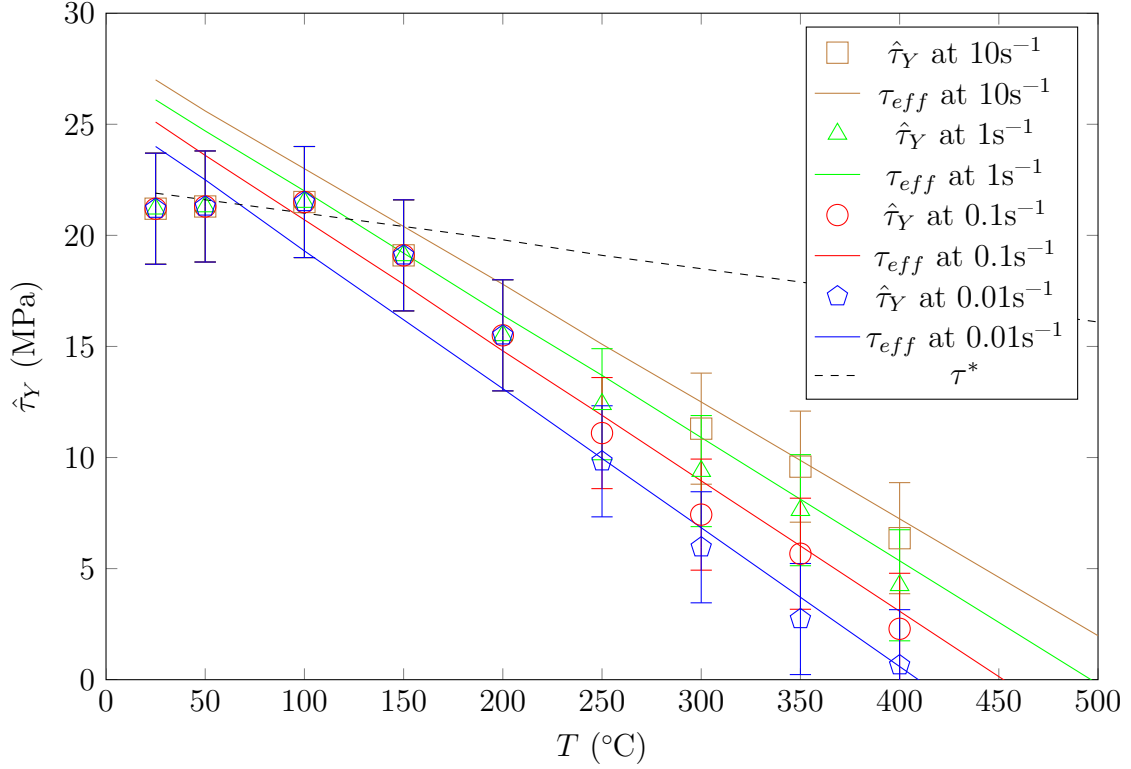


Figure 6.2: Superposition of the experimental yield stress with $\tau_{eff}(T, \epsilon)$ and $\tau^*(T)$ ($C_\lambda = 14$).

This approach is only valid for low temperatures, since equation (6.3) is defined in the absence of thermal activation. τ^* is independent of the strain rate and only slightly dependent on the deformation temperature through μ .

The yield resolved shear stress $\hat{\tau}_Y$ can be calculated from the measurements of $\hat{\sigma}_Y$ as:

$$\hat{\tau}_Y = \frac{\hat{\sigma}_Y}{M} - \tau_{ath} - \tau_d \quad (6.6)$$

$\hat{\tau}_Y$ is plotted as a function of temperature in figure 6.2, together with τ_{eff} , and τ^* . The activation energy in τ_{eff} was taken equal to the energy of jog formation ($Q_{act} = E_j$). At low temperatures, the data points fall on τ^* . When thermal activation kicks in, the data deviate from τ^* and align on τ_{eff} .

Therefore, τ_{eff} has to be redefined. It now consists of two parts representing two distinct concepts:

1. In the absence of thermal activation, $\tau_{eff} = \tau^*$ is the stress to break free from attractive junctions ensuing from the formation of dislocation jogs.
2. When the temperature is high enough, $\tau_{eff} = \tau_{th}$, where τ_{th} represents the temperature dependent stress required to cut through arrays of obstacles, and is defined as in equation (1.35).

In practice, one can define τ_{eff} as follows:

$$\tau_{eff} = \min(\tau^*, \tau_{th}) \quad (6.7)$$

This approach was developed on the late in this thesis, in an attempt to explain the break in the slope of the yield stress of the material. Let us note that taking a constant effective stress under 100 °C, as was done in the model presented chapter 3, does not affect much the simulation results, but it has no physical ground.

This bimodal approach to the effective stress is novel in several ways:

- It is brought about by on the observation of the yield stress of the material instead of its flow stress.
- It points out the saturation of the effective stress at low deformation temperatures. Up to now, only its cancellation at high enough temperature was considered — inherent to the definition of τ_{eff} .
- It precises the nature of the force acting on the mobile dislocations as they cut through the forest dislocations at low temperatures.
- Although the expressions of τ^* and τ_{th} have been known for a long time, they had never been used together before.

A consequence of this method is the introduction of a temperature of change T_{change} of mechanical behaviour. Figure 6.1 shows a clear change in the behaviour of 3 out of 4 evolution parameters at about 150 °C, which could be related to the change in mechanical behaviour introduced here.

The region of transition, here between 100 – 150 °C, still needs be investigated thoroughly, from a microscopic point of view, as the change in mechanical behaviour is most certainly coupled with changes in the microstructure. Indeed, one can assume that the actual behaviour of the material is not discontinuous as shown in figure 6.2, but rather continuously deviates from the attractive junction approach to the obstacle driven approach. Mathematically, such a continuous deviation could be implemented by weighing the contribution of each approach with respect to $T - T_{change}$ — with a sigmoid function for example. Physically, further work on the mechanisms of storage and annihilation of dislocations is clearly needed.

Conclusions

In the course of this thesis, the area of focus was the understanding, description and prediction of the microscopic mechanisms responsible for strain-hardening and recrystallization. A flow stress and a recrystallization model relying on a solid theoretical basis were developed to deal with those issues in an industrial grade AA6082.

The flow stress model introduced in chapter 3 uses a relatively common approach to constitutive modelling. A strong hypothesis, based on the Orowan equation, is that the mobile dislocation density depends only on the strain rate, and remains constant during deformation at constant strain rate. Measurements of the yield stress of the materials were used to calibrate some of the model parameters. It ensued that the effective stress deviates from the obstacle-driven approach at low deformation temperatures (below 100 °C in our case). This issue was further addressed in chapter 6, where it is introduced that the effective stress in the absence of thermal activation is limited by the stress needed to push dislocations away from the attractive junctions of jog formation. This bimodal approach relies on two well-known mechanisms that were not brought together up to now, at least to the author's knowledge.

The recrystallization model developed in chapter 4 introduces a nucleation criterion that depends directly on the pressure acting on the grain boundaries. As the temperature increases, it promotes the nucleation of new grains and their growth. Simultaneously, the microstructure recovers, which inherently inhibits nucleation and grain growth. The model revolves entirely around this competition. The pressure-related nucleation rate is necessary to limit the formation of growth nuclei, hence to control the kinetics of recrystallization.

In both the flow stress and the recrystallization model, the subgrain misorientation was taken constant on average, which resulted in a constant subgrain boundary surface energy. It is however known that the subgrain specific energy is highly dependent on the sub-boundary misorientation, and it should be taken into account in further developments.

The implementation of both models in a finite element code allows for the simulation of actual macroscopic processes. The validity for both models is however limited to the range of parameters in which they were defined. Extrapolation can be performed with caution, in which case the results can bring some insight about the influence of the process conditions on the final microstructure. For instance, the large deformation grades achieved during multipass rolling are not reached experimentally in the lab. The flow stress model predicts that the materials keeps hardening by subgrain refinement, but the hardening decreases slowly towards a steady-state, as seen in figure 1.1. In the same way, the recrystallization model implemented in the finite element code extrapolates the experimental results to a higher temperature and higher deformation grades. The predicted grain radius is lower than observed experimentally, which confirms the tendencies observed in chapter 4, i.e. that the recrystallized grain size decreases with increasing annealing temperature and stored energy of deformation.

Further work is required on the saturation of the effective stress at low deformation temperatures. As mentioned in chapter 6, the change in mechanical behaviour is most probably associated with a change in microscopic deformation mechanism. This should be reflected in the evolution rates of the dislocation densities.

Bibliography

- [1] I. J. Polmear. *Light Alloys*. Butterworth-Heinemann, fourth edition, 2005.
- [2] aluMATTER. <http://dev.aluminium.matter.org.uk>, 2001-2010.
- [3] RUSAL. <http://www.aluminiumleader.com>, 2016.
- [4] J. P. Hirth and J. Loth. *Theory of Dislocations*. Krieger Publishing Company, second edition, 1982.
- [5] D. Hull and D. J. Bacon. *Introduction to Dislocations*. Butterworth-Heinemann, fourth edition, 2001.
- [6] F. J. Humphreys and M. Hatherly. *Recrystallization and Related Annealing Phenomena*. Elsevier Ltd., second edition, 2004.
- [7] E. Nes. Modelling of work hardening and stress saturation in FCC metals. *Progress in Materials Science*, 41(3):129–193, 1998.
- [8] G. I. Taylor. Plastic strain in metals. Lecture notes, May 1938.
- [9] F. Roters, D. Raabe, and G. Gottstein. Work hardening in heterogeneous alloys — A microstructural approach based on three internal state variables. *Acta Materialia*, 48(17):4181–4189, 2000.
- [10] X. Duan and T. Sheppard. Simulation of substructural strengthening in hot flat rolling. *Journal of Materials Processing Technology*, 125–126:179–187, 2002.
- [11] O. Rowan. Problems of plastic gliding. *Proceedings of the Physical Society*, 52(1):8–22, 1940.
- [12] A. D. Rollett. *Strain Hardening at Large Strains in Aluminium Alloys*. PhD thesis, Los Alamos National Laboratory, March 1988.
- [13] A. D. Rollett and Kocks U. F. A review of the stages of work hardening. *Solid State Phenomena*, 35–36:1–18, 1994.

- [14] N. M. Ghoniem, J. R. Matthews, and R. J. Amodeo. A Dislocation Model for Creep in Engineering Materials. *Res Mechanica*, 29(3):197–219, 1990.
- [15] F. R. N. Nabarro, Z. S. Basinski, and D. B. Holt. The Plasticity of Pure Single Crystals. *Advances in Physics*, 13(50):193–323, 1964.
- [16] J. Gil Sevillano, P. van Houtte, and E. Aernoudt. Large strain work hardening and textures. *Progress in Materials Science*, 25(2–4):69–134, 1980.
- [17] M. Zehetbauer and V. Seumer. Cold work hardening in stages IV and V of F.C.C. metals — I. Experiments and interpretation. *Acta Metallurgica*, 41(2):577–588, 1993.
- [18] G. I. Taylor. The Mechanism of Plastic Deformation of Crystals. Part I.—Theoretical. *Proceedings of the Royal Society of London A: Mathematical, Physical and Engineering Sciences*, 145(855):362–387, 1934.
- [19] G. I. Taylor. The Mechanism of Plastic Deformation of Crystals. Part II.—Comparison with Observations. *Proceedings of the Royal Society of London A: Mathematical, Physical and Engineering Sciences*, 145(855):388–404, 1934.
- [20] J. Gil Sevillano. Flow Stress and Work Hardening. In H. Mughrabi, R. W. Cahn, P. Haasen, and E. J. Kramer, editors, *Plastic Deformation and Fracture Materials*, volume 6 of *Materials Science and Technology A comprehensive Treatment*, chapter 2, pages 19–88. VCH Verlagsgesellschaft mbH, Weinheim and VCH Publishers Inc., New York, 1993.
- [21] U. F. Kocks. Laws for Work-Hardening and Low-Temperature Creep. *Journal of Engineering Materials and Technology*, 98(1):76–85, 1976.
- [22] Y. Estrin and H. Mecking. A unified phenomenological description of work hardening and creep based on one-parameter models. *Acta Metallurgica*, 32(1):57–70, 1984.
- [23] Y. Estrin. Dislocation-Density-Related Constitutive Modeling. In A. S. Krausz and K. Krausz, editors, *Unified Constitutive Laws of Plastic Deformation*, chapter 2, pages 69–106. Academic Press, 1996.
- [24] E. Nes, K. Marthinsen, and B. Rønning. Modelling the evolution in microstructure and properties during processing of aluminium alloys. *Journal of Materials Processing Technology*, 117(3):333–340, 2001.
- [25] Kablman E. and P. Sherstnev. Integrated Modeling of Strength Evolution in Al-Mg-Si Alloys during Hot Deformation. *Materials Science Forum*, 765:429–433, 2013.

- [26] M. F. Ashby. Results and consequences of a recalculation of the Frank-Read and the Orowan stress. *Acta Metallurgica*, 14(5):679–681, 1966.
- [27] A. H. Cottrell and B. A. Bilby. Dislocation Theory of Yielding and Strain Ageing of Iron. *Proceedings of the Physical Society. Section A*, 62(1):49–62, 1949.
- [28] D. Caillard and J. L. Martin, editors. *Thermally Activated Mechanisms in Crystal Plasticity*. Pergamon Materials Science. Elsevier Ltd., 2003.
- [29] H. Mecking and U. F. Kocks. Kinetics of flow and strain-hardening. *Acta Metallurgica*, 29(11):1865–1875, 1981.
- [30] H. Aretz, R. Luce, M. Wolske, M. Goerdeler, V. Marx, G. Pomana, and G. Gottstein. Integration of physically based models into FEM and application in simulation of metal forming processes. *Modelling and Simulation in Materials Science and Engineering*, 8:881–891, 2000.
- [31] M. Goerdeler and Gottstein G. A microstructural work hardening model based on three internal state variables. *Materials Science and Engineering: A*, 309–310:377–381, 2001.
- [32] A. V. Granato, K. Lücke, J. Schlipf, and L. J. Teutonico. Entropy Factors for Thermally Activated Unpinning of Dislocations. *Journal of Applied Physics*, 35:2732–2745, 1964.
- [33] C. M. Sellars and Q. Zhu. Microstructural modelling of aluminium alloys during thermomechanical processing. *Materials Science and Engineering: A*, 280(1):1–7, 2000.
- [34] X. Duan and T. Sheppard. Influence of forming parameters on the final subgrain size during hot rolling of aluminium alloys. *Journal of Materials Processing Technology*, 130–131:245–249, 2002.
- [35] J. Talamantes-Silva, M. F. Abbod, E. S. Puchi Cabrera, J. H. Howard, J. H. Beynon, C. M. Sellars, and D. A. Linkens. Microstructure modelling of hot deformation of Al–1%Mg alloy. *Materials Science and Engineering: A*, 525(1–2):147–158, 2009.
- [36] M. Crumbach, M. Goerdeler, and G. Gottstein. Modelling of recrystallisation textures in aluminium alloys: I. Model set-up and integration. *Acta Materialia*, 54(12):3275–3289, 2006.
- [37] M. Crumbach, M. Goerdeler, and G. Gottstein. Modelling of recrystallisation textures in aluminium alloys: II. Model performance and experimental validation. *Acta Materialia*, 54(12):3291–3306, 2006.

- [38] M. Crumbach, L. Neumann, M. Goerdeler, H. Aretz, G. Gottstein, and R. Kopp. Through-process modelling of texture and anisotropy in AA5182. *Modelling and Simulation in Materials Science and Engineering*, 14(5):835–856, 2006.
- [39] H. Mughrabi. Dislocation wall and cell structures and long-range internal stresses in deformed metal crystals. *Acta Metallurgica*, 31(9):1367–13779, 1983.
- [40] A. S. Argon and P. Haasen. A new mechanism of work hardening in the late stages of large strain plastic flow in F.C.C. and diamond cubic crystals. *Acta Metallurgica et Materialia*, 8(11):3289–3306, 1993.
- [41] X. Duan and T. Sheppard. Simulation and control of microstructure evolution during hot extrusion of hard aluminium alloys. *Materials Science and Engineering: A*, 351(1–2):282–292, 2003.
- [42] R. Sandström and R. Lagneborg. A model for hot working occurring by recrystallization. *Acta Metallurgica*, 23(3):187–398, 1975.
- [43] Y. Estrin. Dislocation theory based constitutive modelling: foundations and applications. *Journal of Materials Processing Technology*, 80–81:33–39, 1998.
- [44] F. Roters. A new concept for the calculation of the mobile dislocation density in constitutive models of strain hardening. *physica status solidi (b)*, 240(1):68–74, 2003.
- [45] M. F. Ashby. The Deformation of Plastically Non-homogeneous Materials. *Philosophical Magazine*, 21(170), 1970.
- [46] A. Ma, F. Roters, and D. Raabe. A dislocation density based constitutive model for crystal plasticity FEM including geometrically necessary dislocations. *Acta Materialia*, 54(8):2169–2179, 2006.
- [47] W. Pantleon. Stage IV work-hardening related to disorientations in dislocation structures. *Materials Science and Engineering: A*, 387–389(15):257–261, 2004.
- [48] E. Nes and K. Marthinsen. Modeling the evolution in microstructure and properties during plastic deformation of f.c.c.-metals and alloys – an approach towards a unified model. *Materials Science and Engineering: A*, 322(1–2):176–193, 2002.
- [49] G. V. S. S. Prasad, M. Goerdeler, and G. Gottstein. Work hardening model based on multiple dislocation densities. *Materials Science and Engineering: A*, 400–401:231–233, 2005.

- [50] J. E. Bailey. Electron Microscope Observations on the Annealing Processes Occuring in Cold-worked Silver. *Philosophical Magazine*, 5(56):833–842, 1960.
- [51] J. E. Bailey and P. B. Hirsch. The recrystallization process in some polycrystalline metals. *Proceedings of the Royal Society of London A: Mathematical, Physical and Engineering Sciences*, 267(1328):11–30, 1962.
- [52] J. E. Burke and D. Turnbull. Recrystallization and grain growth. *Progress in Metal Physics*, 3:220–244, 1952.
- [53] M. Avrami. Kinetics of Phase Change. I General Theory. *The Journal of Chemical Physics*, 7:1103–1112, 1939.
- [54] M. Avrami. The Kinetics of Phase Change. II Transformation-Time Relations for Random Distribution of Nuclei. *The Journal of Chemical Physics*, 8:212–224, 1940.
- [55] J. Farjas and P. Roura. Modification of the Kolmogorov – Johnson – Mehl – Avrami rate equation for non-isothermal experiments and its analytical solution. *Acta Materialia*, 54(20):5573–5579, 2006.
- [56] H. E. Vatne, T. Furu, R. Ørsund, and E. Nes. Modelling recrystallization after hot deformation of aluminium. *Acta Materialia*, 44(11):4463–4473, 1996.
- [57] P. Sherstnev. *Physikalisch basierte Modellierung der Gefügeentwicklung während des Warmwalzens von Aluminiumlegierungen*. PhD thesis, Montanuniversität Leoben, October 2009.
- [58] P. Loidolt. Statische Rekristallisation von AA6082. Projektlabor Metalle und Keramiken, February 2012.
- [59] K. Drozd, J. Horsinka, J. Kliber, M. Černý, D. Ostroushko, and I. Mamuzic. Study of the development of strain in plane strain compression test. In *Metal 2011*, 2011.
- [60] C. A. Schneider, W. S. Rasband, and K. W. Eliceiri. NIH Image to ImageJ: 25 years of image analysis. *Nature Methods*, 9(7):671–675, 2012.
- [61] W. S. Rasband. <http://imagej.nih.gov/ij/>, 1997-2016.
- [62] Scientific Forming Technologies Corporation. <http://www.deform.com/>, 2016.
- [63] P. Loidolt. Cold Deformation and Recrystallization of the Aluminium Alloy 6082. Master’s thesis, Graz University of Technology, March 2014.
- [64] EDAX Inc. <http://www.edax.com/>, 2016.

- [65] F. Kroupa. Dislocation dipoles and dislocation loops. *Journal de Physique Colloques*, 27(C3):154–167, 1966.
- [66] S. D. Yadav, S. Kalácska, M. Domáková, D. Canelo Yubero, R. Resel, I. Groma, C. Beal, B. Sonderegger, and C. Poletti. Evolution of the substructure of a novel 12% Cr steel under creep conditions. *Materials Characterization*, 115:23–31, 2016.
- [67] D. Kuhlmann-Wilsdorf. The theory of dislocation-based crystal plasticity. *Philosophical Magazine A*, 79(4):955–1008, 1999.
- [68] F. R. Castro-Fernandez, C. M. Sellars, and J. A. Whiteman. Changes of the flow stress and microstructure during hot deformation of Al-1Mg-1Mn. *Materials Science and Technology*, 6(5):453–460, 1990.
- [69] M. Spuller. Study of the recrystallization of a plane strain cold deformed commercial AA6082 at 300 °C and 400 °C. Internship report, 2015.
- [70] Y. Huang and F. J. Humphreys. Measurements of grain boundary mobility during recrystallization of a single-phase aluminium alloy. *Acta Materialia*, 47(7):2259–2268, 1999.
- [71] Y. Huang and F. J. Humphreys. Subgrain growth and low angle boundary mobility in aluminium crystals of orientation $\{110\}\langle 001\rangle$. *Acta Materialia*, 48(8):2017–2030, 2000.
- [72] Y. Huang and F. J. Humphreys. Measurements of subgrain growth in a single-phase aluminum alloy by high-resolution EBSD. *Materials Characterization*, 47(3–4):235–240, 2001.
- [73] Y. Huang and F. J. Humphreys. The effect of solutes on grain boundary mobility during recrystallization and grain growth in some single-phase aluminium alloys. *Materials Chemistry and Physics*, 132(1):166–174, 2012.
- [74] C. Schäfer, V. Mohles, and G. Gottstein. Modeling of non-isothermal annealing: Interaction of recrystallization, recovery, and precipitation. *Acta Materialia*, 59(17):6574–6587, 2011.
- [75] A. Lens, Maurice C., and J. H. Driver. Grain boundary mobilities during recrystallization of Al-Mn alloys as measured by in situ annealing experiments. *Materials Science and Engineering: A*, 403(1–2):144–153, 2005.
- [76] H. S. Zurob, Y. Bréchet, and J. Dunlop. Quantitative criterion for recrystallization nucleation in single-phase alloys: Prediction of critical strains and incubation times. *Acta Materialia*, 54(15):3983–3990, 2006.

- [77] EngineeringToolBox. <http://www.engineeringtoolbox.com>.
- [78] M. Kumar, C. Poletti, and H. P. Degischer. Precipitation kinetics in warm forming of AW-7020 alloy. *Materials Science and Engineering: A*, 561:362–370, 2013.